Angewandte Chemie
Eine Zeitschrift der Gesellschaft Deutscher Chemiker

Supporting Information

A Novel Electrode for Value-Generating Anode Reactions in Water Electrolyzers at Industrial Current Densities

C. Wang, Y. Wu, A. Bodach, M. L. Krebs, W. Schuhmann, F. Schüth**

Content

Materials and Methods

1. General data

All solvents and chemicals were used as purchased without further purifications. Chemicals: 5-hydroxymethylfurfural (Sigma-Aldrich, 99 %), Sodium hydroxide (NaOH, reagent, pellet; VWR Chemicals), Iron(III) chloride hexahydrate (reagent grade, ≥98%, Sigma-Aldrich), Iron(III) nitrate nonahydrate (ACS reagent, ≥98%, Sigma-Aldrich), Iron(III) sulfate hydrate (97%, Sigma-Aldrich), Iron(II) chloride tetrahydrate (ReagentPlus®, 98%, Sigma-Aldrich), Copper(II) chloride dihydrate (ACS reagent, ≥99.0%, Sigma-Aldrich), Manganese(II) chloride tetrahydrate (ACS reagent, ≥98%, Sigma-Aldrich), 37 wt % HCl (J. T. Baker), 65 wt % HNO_3 (J. T. Baker), 35 wt % H_2O_2 (J. T. Baker), Cobalt(II) nitrate hexahydrate ($Co(NO_3)_2 \cdot 6H_2O$; ACS reagent, ≥98%; Sigma-Aldrich), Potassium hydroxide (KOH, reagent, pellet; VWR Chemicals ≥85%), 1,6-Diaminohexane (≥99% (GC), Sigma-Aldrich), 1-Butanol (99%; Alfa Aesar), Ethanol (absolute, ≥99.8%; Sigma-Aldrich), 1-Phenylethanol (98%; Sigma-Aldrich), 3-Phenyl-1-propylamine (98%; Sigma-Aldrich), Cyclohexanemethylamine (98%; Sigma-Aldrich), Benzyl alcohol (anhydrous, 99.8%; Sigma-Aldrich), Benzylamine (ReagentPlus®, 99%; Sigma-Aldrich), Cyclohexanol (ReagentPlus®, 99%; Sigma-Aldrich), Ethylene glycol (anhydrous, 99.8%; Sigma-Aldrich), Furfural (ACS reagent, 99%; Sigma-Aldrich), Furfuryl alcohol(98%; Sigma-Aldrich), 1-Propanol (anhydrous, 99.7%; Sigma-Aldrich), Formic acid (reagent grade, ≥95%; Sigma-Aldrich), D-(+)-Glucose (≥99.5% (GC); Sigma-Aldrich), Glycerol (ACS reagent, ≥99.5%; Sigma-Aldrich), Isopropanol (anhydrous, 99.5%; Sigma-Aldrich), Methanol (anhydrous, 99.8%; Sigma-Aldrich), Hydrazine hydrate (N_2H_4 64-65 %, reagent grade, 98%), Sodium borohydride (powder, ≥98.0%; Sigma-Aldrich), D-Sorbitol (powder, ≥98.0%; Sigma-Aldrich), Urea (ACS reagent, 99.0-100.5%; Sigma-Aldrich), and Oil Red O (Alfa Aesar). Ni foam, Fe foam, Cu foam (Recemat BV, Netherlands), Nickel plate (99.5%, Alfa Aesar), Perfluorinated membrane made from Nafion™ 117 (Sigma-Aldrich) and anion-exchange membrane (Fumasep FAB-PK-130, fuel cell store).

Prior to the synthesis, all the flasks were washed with a solution of aqua regia (HCl/HNO_3 = 3:1 v/v) to remove any traces of metal residue, followed by washing with water and acetone, and finally dried at 80 °C overnight. Milli-Q water (18.2 MΩ) was used for all the syntheses and catalysis experiments.

2. Characterizations.

--Elemental analysis was carried out at a commercial analysis laboratory (*Mikroanalytisches Laboratorium Kolbe Fraunhofer Institut UMSICHT, Gebäude G-Osterfelder Str. 3 D-46047 Oberhausen*) with an AAnalyst 200 **Atomic Absorption Spectrometer (AAS).**

--Scanning electron microscopy (SEM) images were taken with a Hitachi S-5500 microscope. The EDX analyses were performed with an SDD-detector and software from Thermo Fisher.

--Scanning transmission electron microscope (STEM) images were taken with a HD 2700 ultrahigh-resolution cold field emission scanning microscope at an acceleration voltage of 200 kV. An EDAX Octane T Ultra W 200mm^2 SDD with TEAM-Software was attached to the instrument.

--**Transmission electron microscopy (TEM)** images of the catalysts were recorded with a Hitachi HF-2000 microscope at an acceleration voltage of 200 kV.

--**X-ray powder diffraction**: Powder X-ray diffraction (XRD) patterns were obtained at Rigaku SmartLab SE diffractometer with 9 kW rotating Cu-Kα radiation.

PUL: The X-ray powder pattern for qualitative phase analysis was collected on a Stoe STADI P transmission diffractometer using Mo radiation (0.7093 Å). The instrument is equipped with a primary Ge (111) monochromator (MoKα_1) and a position sensitive Mythen1K detector. Data was collected in the range between 3 and 70° 2θ with a step width of 0.015° 2θ. Measuring time per step was 40s. For the measurement, the sample was prepared between two foils in a transmission sample holder. The measured pattern was evaluated qualitatively by comparison with entries from the ICCD PDF-2 powder pattern database.

STO: The X-ray powder patterns for qualitative phase analysis were collected on a Stoe STADI P transmission diffractometer using Mo radiation (0.7093 Å). The instrument is equipped with a primary Ge (111) monochromator (MoKα_1) and a position sensitive

Mythen1K detector. Data were collected in the range between 5 and 70° 2θ with a step width of 0.015° 2θ. Measuring time per step was 20s. For the measurements, the samples were prepared in a transmission sample holder. The measured patterns were evaluated qualitatively by comparison with entries from the ICCD PDF-2 powder pattern database.

PUL and STO Data are from different goniometers with equal/same parts sharing the same x-ray tube.

--**X-ray photoelectron spectra (XPS)**: XPS measurements were performed with a spectrometer from SPECS GmbH equipped with a PHOIBOS 150 1D-DLD hemispherical energy analyser. The monochromatized Al Kα X-ray source (E=1486.6 eV) was operated at 14 kV and 100W. For the narrow scans, an analyzer pass energy of 20 eV was applied. The medium area mode was used as lens mode. The base pressure during the experiment in the analysis chamber was $5x10^{-10}$ mbar. To account charging effects, all spectra are referred to C 1s at 284.5 eV.

--**Atomic force microscopy** (AFM) measurements were carried out on a Bruker multimode 8 scanning probe microscope.

--XAFS measurements: The X-ray absorption fine structure spectra Fe K-edge were collected at 44A beamline of National Synchrotron Radiation Research Center (NSRRC) Taiwan. The data were collected in fluorescence mode using a Lytle detector while the corresponding reference samples were collected in transmission mode. The electrode sheet was assembled on the Kapton adhesive tape.

XAFS Analysis and Results: The acquired EXAFS data were processed according to the standard procedures using the ATHENA module of Demeter software packages.

The EXAFS spectra were obtained by subtracting the post-edge background from the overall absorption and then normalizing with respect to the edge-jump step. Subsequently, the χ(k) data were Fourier transformed to real (R) space using a hanging windows (dk=1.0 $Å^{-1}$) to separate the EXAFS contributions from different coordination shells. To obtain the quantitative structural parameters around central atoms, least-

squares fitting was performed using the ARTEMIS module of Demeter software packages.

The following EXAFS equation was used:

$$\chi(k) = \sum_j \frac{N_j S_0^2 F_j(k)}{kR_j^2} \cdot \exp[-2k^2\sigma^2{}_j] \cdot \exp[\frac{-2R_j}{\lambda(k)}] \cdot \sin[2kR_j + \phi_j(k)]$$

the theoretical scattering amplitudes, phase shifts and the photoelectron mean free path for all paths were calculated. S_0^2 is the amplitude reduction factor, $F_j(k)$ is the effective curved-wave backscattering amplitude, N_j is the number of neighbors in the j^{th} atomic shell, R_j is the distance between the Xray absorbing central atom and the atoms in the j^{th} atomic shell (back scatterer), λ is the mean free path in Å, $\phi_j(k)$ is the phase shift (including the phase shift for each shell and the total central atom phase shift), σ_j is the Debye-Waller parameter of the j^{th} atomic shell (variation of distances around the average R_j). The functions $F_j(k)$, λ and $\phi_j(k)$ were calculated with the ab initio code FEFF9. The additional details for EXAFS simulations are given below.

All fits were performed in the *R* space with a *k*-weight of 2 while phase correction was also applied in the first coordination shell to make R value close to the physical interatomic distance between the absorber and shell scatterer. The coordination numbers of model samples were fixed as the nominal values, while the S_0^2, the internal atomic distances R, Debye-Waller factor σ^2, and the edge-energy shift Δ were allowed to run freely.

3. Experimental section

3.1 Electrodes preparation.

NiFe-t electrodes: The nickel foam (NF) was cut into slices (1 cm × 3 cm) and successively ultrasonicated in hydrochloric acid (3 M), acetone, ethanol and water for 15 min, respectively. Then, the NF was put into a 50 mL beaker containing a mixture of $FeCl_3 \cdot 6H_2O$ (2.5 mmol) and 5% H_2O_2 (25 mL) that had been reacted for 5 mins. After soaking the nickel foam for a given time (t=1, 5 or 10 min), the solution was decanted and the NF rinsed three times with ultrapure water. The **NiFe-t** electrode was then removed from the beaker, put into a plastic petri dish, and dried at 60 ^oC in an oven for 24 h.

NiFe-1 (without H_2O_2) electrode: NF was cut into slices (1 cm × 3 cm) and ultrasonicated in hydrochloric acid (3 M), acetone, ethanol and water for 15 min, respectively. Then, the NF was put into a 50 mL baker containing a mixture of $FeCl_3 \cdot 6H_2O$ (2.5 mmol) and 25 mL H_2O that had been stirred for 5 mins. After soaking the nickel foam for 1 min, the solution was decanted, and the NF rinsed three times with ultrapure water. The **NiFe-1 (without H_2O_2)** electrode was then removed from the beaker, put into a plastic petri dish, and dried at 60 ^oC in an oven for 24 h.

NF-H_2O_2 electrode was synthesized in the same manner as described for the preparation of NiFe-1 without the addition of $FeCl_3 \cdot 6H_2O$.

3.2 Electrochemical measurements

Taking the electrooxidation of HMF as an example.

The oxygen evolution reaction (OER), hydrogen evolution reaction (HER), and electrocatalytic oxidation of HMF were conducted using a Gamry Interface 1010 B electrochemical workstation at room temperature with a three-electrode system in a H-type cell, which was separated by a Nafion 117 membrane (or the PK-130 membrane).

The Fe (H_2O_2)-modified NF electrode was directly used as the working electrode (WE), with typically an approximately 10 mm x 10 mm piece exposed to the electrolyte. This was used as the 1 cm^2 standard for normalization of the current to electrode surface area, being aware that for porous electrodes the true surface area is higher. It was determined from the double layer capacitance, see below. A coiled Pt wire was used as the counter electrode (CE), and a Hg/HgO electrode was used as the reference electrode (RE). An external thermometer in the cathode chamber was used to track the temperature changes during the reaction. The Hg/HgO electrode (RE-61AP) is available from ALS Co., Ltd, and 1 M sodium hydroxide is used as an electrolyte solution; E_0=118 mV vs. RHE (25 °C). All those reactions were performed in 5 mL of 1.0 M KOH electrolyte solution with and without 50 mM HMF (or 100 mM substrates). The solution in the cathode chamber was stirred at around 250 rpm, in the anode chamber at 625 rpm. Before the experiments, CV runs were performed at a rate of 100 mV/s from 0-0.7 V vs. Hg/HgO for 20 cycles to obtain a stable electrode. For catalyst recyclability test, the electrode was rinsed three times with ultrapure water and directly used for the next run. The potential range was cyclically scanned at a scan rate of 5 mV s^{-1}. The potentials were converted to the reversible hydrogen electrode potential (RHE) through the Nernst equation: ($E_{(RHE)} = E_{(Hg/HgO)} + 0.059\times pH + 0.118$ V). The post-run iR corrections were applied at 85%. The scan rate for LSV was kept at 5 mV s^{-1}. The electrochemical surface area (ECSA) was evaluated in terms of the double-layer capacitance (C_{dl}). The equation for ESCA measurements is: $ECSA = C_{dl}/C_s$, where C_s is the specific capacitance, which is assumed to be 0.040 mF/cm^2 in 1 M KOH solution, based on values previously reported for metal oxide catalysts. C_{dl} was calculated as half of the slope of the plot of capacitive current in a non-faradaic double-layer region against scan rate. Cyclic voltammetry (CV) was performed in 1.0 M KOH with 50 mM HMF at different scan rates of 20-100 mV s^{-1} in a potential window of 1.087 to 1.187 V vs. RHE. Electrochemical impedance spectroscopy (EIS) measurements were performed in 1.0 M KOH at 1.437 V vs. RHE from 20000 to 0.01 Hz with an amplitude of 5 mV. The potentials for the $Ni^{2+/3+}$ oxidation wave were found to be reproducible

within ±20 mV, when the reaction was carried out without HMF by altogether six different operators in three different laboratories with different equipment and chemicals, which is probably thus the precision of absolute potentials given throughout the manuscript. Comparative data for differently modified electrodes, however, were always recorded by the same operator with identical equipment and chemicals.

3.3 Quantitative Product Analysis

Taking the electrooxidation of HMF as an example, other analyses of the products and intermediates are shown in the corresponding HPLC or GC traces.

To analyze the products of HMF oxidation quantitatively and calculate the corresponding Faradaic efficiencies, electrolyte solutions during chronoamperometry testing were taken from the cell and analyzed by HPLC on a Shimadzu LC-2030 chromatograph equipped with a 100 mm organic acid resin column with 8.0 mm i.d. and a precolumn (40 mm organic acid resin with 8.0 mm i.d.). As the mobile phase, a 2 mM aqueous solution of trifluoroacetic acid was used with a flow rate of 1 mL min^{-1} at a temperature of 40 °C. For detection, a UV detector was used and external one-point calibration was applied to quantify HMF, HMFCA, DFF, FFCA, furoic acid and FDCA. The HMF conversion (%) and the yields (%) of FDCA were calculated using equations (1) and (2):

$$\text{HMF conversion (\%)} = [\text{mol (HMF consumed)} / \text{mol (HMF initial)}] \times 100 \quad (1)$$

$$\text{FDCA yield (\%)} = [\text{mol (FDCA formed)} / \text{mol (HMF initial)}] \times 100 \quad (2)$$

The faradaic efficiency (FE) of FDCA was calculated by equations (3):

$$\text{Faradaic efficiency (\%)} = [\text{mol (FDCA formed)} / (\text{Charge} / (6 \times F))] \times 100 \quad (3)$$

where F is the Faraday constant (96485 C mol^{-1}).

4. Optimizations of the electrode and the reaction condition

Table S1. Selected examples on the HMF electrochemical oxidation to FDCA in alkaline condition.

Catalysts	Condition	*E* [V *vs.* RHE]	FE	Ref.
NiFe-LDH/CP	1 M KOH/10 mM HMF 1 M KOH/50 mM HMF 1 M KOH/100 mM HMF	1.32 V/20 mA cm^{-2} 1.5 V/~180 mA cm^{-2} 1.5 V /~280 mA cm^{-2}	99.4% at 1.23 V 77.2% at 1.43 V	[1]
NiCoFe-LDHs	1 M NaOH/5 mM HMF	1.51V/20 mA cm^{-2}	~90% at 1.54V	[2]
Cu_xS@NiCo LDHs	1 M KOH/10 mM HMF	1.34 V/20 mA cm^{-2}	~90% at 1.32V	[3]
Co−P/CF	1 M KOH/50 mM HMF	1.38 V/20 mA cm^{-2}	---	[4]
Ni_3S_2/NF	1 M KOH/10 mM HMF	~1.35 V/10 mA cm^{-2}	99% at 1.423 V	[5]
Ni_2P NPA/NF	1 M KOH/10 mM HMF	~1.35 V/10 mA cm^{-2}	99% at 1.423 V	[6]
CoO-$CoSe_2$	0.1 M KOH/10 mM HMF	~1.35 V/20 mA cm^{-2}	97.9% at 1.43 V	[7]
NiSe@NiO_x	1 M KOH/10 mM HMF	~1.35 V/20 mA cm^{-2}	99% at 1.423 V	[8]
$NiCo_2O_4$	1 M KOH/5 mM HMF	1.53 V/14.8 mA cm^{-2}	87.5% at 1.5 V	[9]
CoNW/NF	1 M KOH/10 mM HMF	1.311 V/10 mA cm^{-2}	98.6% at 1.49 V	[10]
$CuCo_2O_4$	1 M KOH/50 mM HMF	~1.23 V/10 mA cm^{-2} ~1.37 V/150 mA cm^{-2}	94% at 1.45 V	[11]
Ni_xB	1 M KOH/10 mM HMF	~1.40 V/10 mA cm^{-2}	99% at 1.45 V	[12]
hp-Ni	1 M KOH/10 mM HMF	~1.35 V/10 mA cm^{-2}	98% at 1.423 V	[13]
E-CoAl-LDH-NSA	1 M KOH/10 mM HMF	~1.30 V/10 mA cm^{-2}	99.4% at 1.52 V 97.47% at 1.57 V 69.63% at 1.62 V	[14]
MoO_2-FeP@C	1 M KOH/10 mM HMF	~1.405 V/100 mA cm^{-2}	97.8% at 1.424V	[15]

Co_3O_4 nanowire	1 M KOH/100 mM HMF	~1.65 V/100 mA cm^{-2}	98.4% at 1.469 V	[16]
Ni_3N@C.	1 M KOH/10 mM HMF	~1.45 V/180 mA cm^{-2}	98% at 1.45 V	[17]
CoO-$CoSe_2$	1 M KOH/10 mM HMF	~1.43 V/40 mA cm^{-2}	91% at 1.43 V	[18]
VN	1 M KOH/10 mM HMF	~1.45 V/120 mA cm^{-2}	90% at 1.45 V	[19]
$(FeCrCoNiCu)_3O_4$ nanosheets	1 M KOH/50 mM HMF	~1.5 V/55 mA cm^{-2}	96.6% at 1.5 V	[20]
Pt/$Ni(OH)_2$	1 M KOH/50 mM HMF	~1.5 V/30 mA cm^{-2}	~96% at 1.5 V	[21]
CoFe@NiFe	1 M KOH/10 mM HMF	~1.5 V/65 mA cm^{-2}	~99.8% at 1.5 V	[22]
CoFe Prussian Blue Analogue Films	1 M KOH/500 mM HMF	~1.5 V/45 mA cm^{-2}	~84% at 1.42 V	[23]
intermetallic iron silicide (FeSi)	1 M KOH/100 mM HMF	~1.5 V/300 mA cm^{-2}	~94% at 1.5 V	[24]

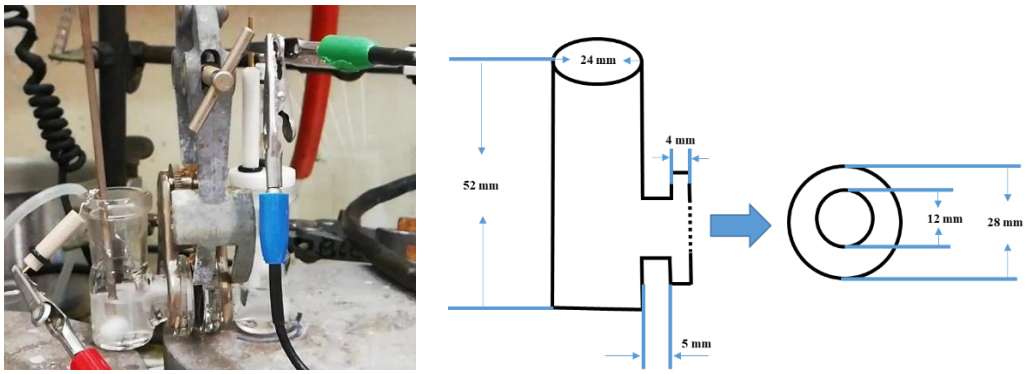

Figure S1. (Left) Digital picture of the cell when it is used for reaction. Temperature changes v.s. time at the cathode chamber measured by an external thermometer. (right) The parameters of the designed half H cell.

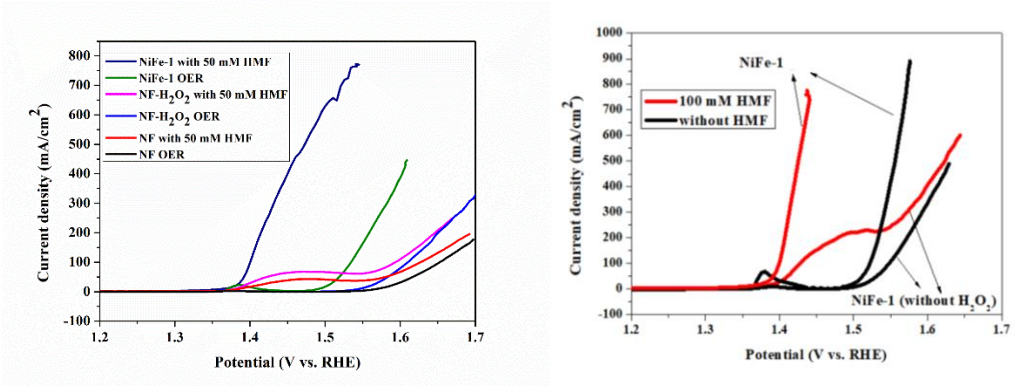

Figure S2. (Left) LSV curves for NiFe-1 electrode in comparisons with the H_2O_2 treated NF and the purified NF in 1 M KOH with and without 50 mM HMF. (Right) LSV curves for NiFe-1 electrodes in 1 M KOH with and without 100 mM HMF (For the investigations of the influence of H_2O_2 in the NiFe-1 electrode preparations to the current responses of HMF).

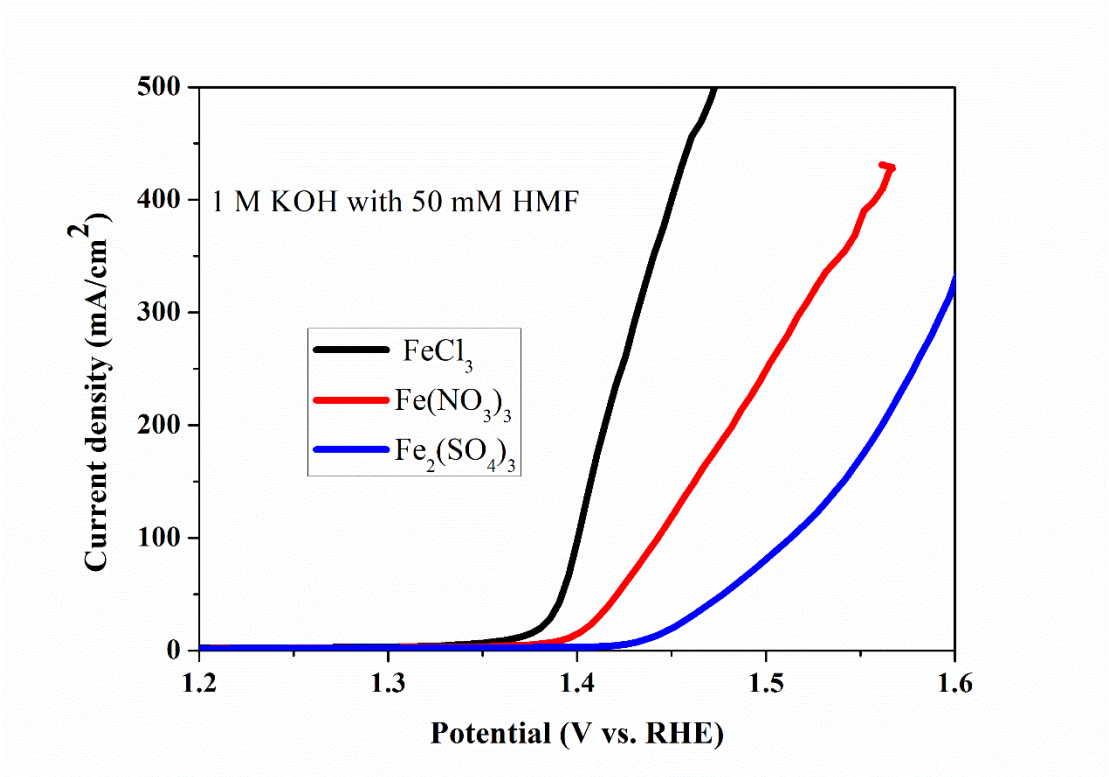

Figure S3. LSV curves for NiFe electrodes using different Fe^{3+} precursors in 1 M KOH with and without 50 mM HMF.

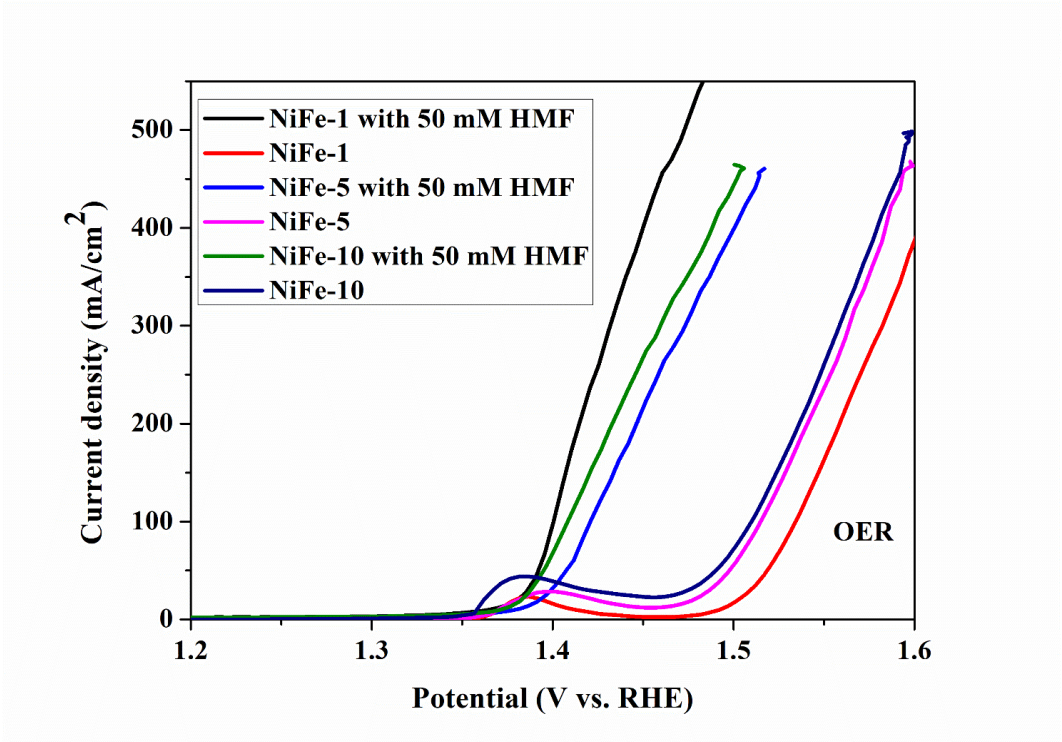

Figure S4. LSV curves for NiFe-t (t is the reaction time in the synthesis, min) in 1 M KOH with and without 50 mM HMF.

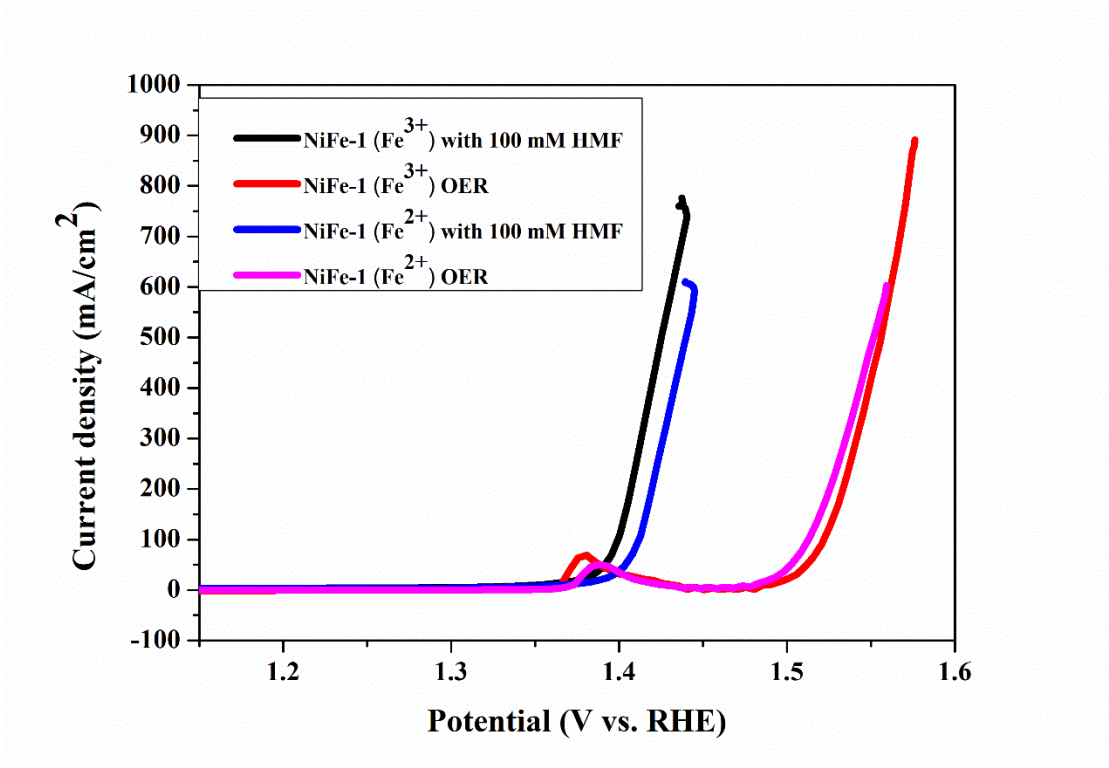

Figure S5. LSV curves for NiFe-1 electrodes in 1 M KOH with and without 100 mM HMF.

For the investigations of the influence of the oxidation states of Fe to the current responses of HMF. Fe^{3+} performed better.

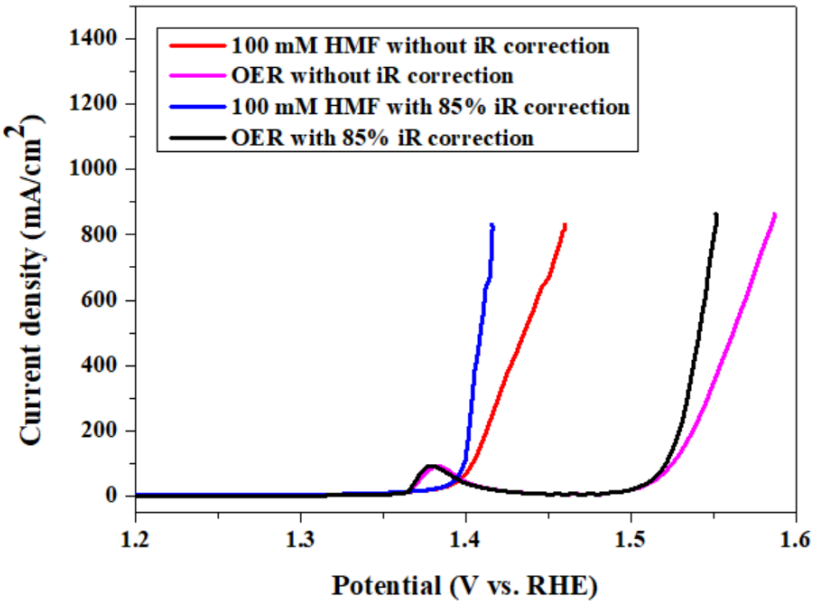

Figure S6. Comparisons to the OER and HMF oxidation in terms of LSV curves for NiFe-1 electrode with and without iR compensation. Condition: 1M KOH with and without 100 mM HMF.

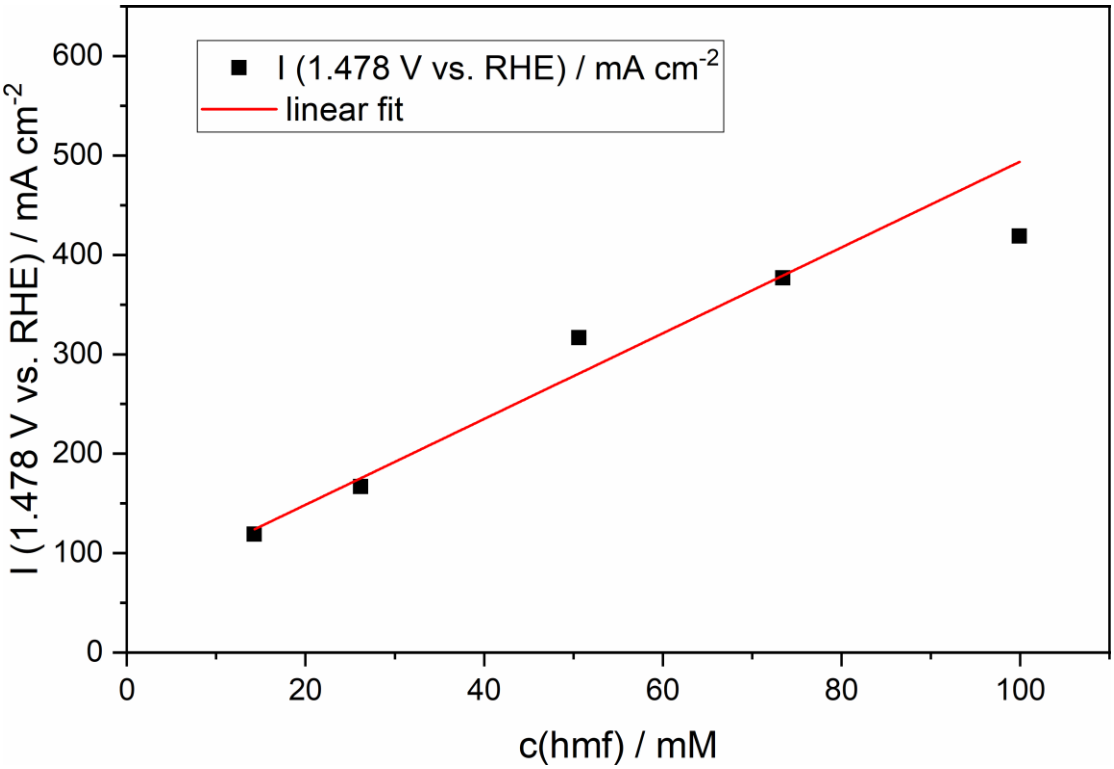

Figure S7. Current density in mA cm^{-2} at 1.478 V (vs. RHE) while varying HMF concentration. Linear fit shows a first order reaction with respect to HMF concentration. Reaction condition: 1 M KOH, 0.9 cm^2 geometrical electrode surface.

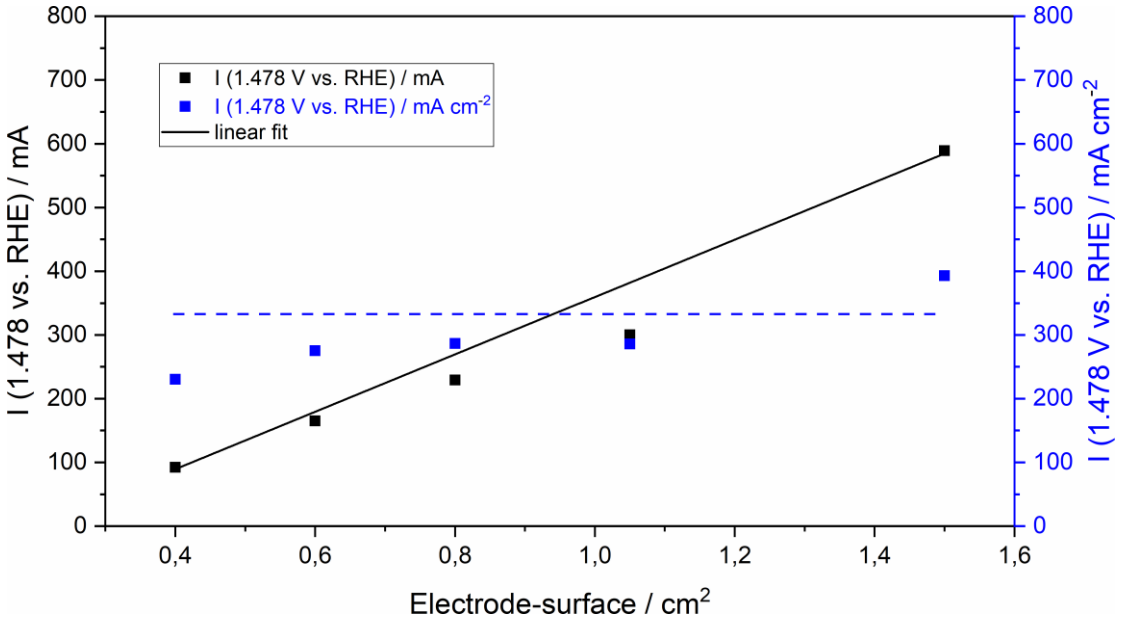

Figure S8. Current in mA (black) and surface normalized current in mA/cm^2 at 1.478 V (vs. RHE) while reducing electrode surface area. Linear fit of the current (black line) shows a first order reaction with respect to the geometrical electrode surface. The dashed blue line serves as a guide to the eye maintaining approximately constant surface-normalized currents. Reaction condition: 1 M KOH, 50 mM HMF.

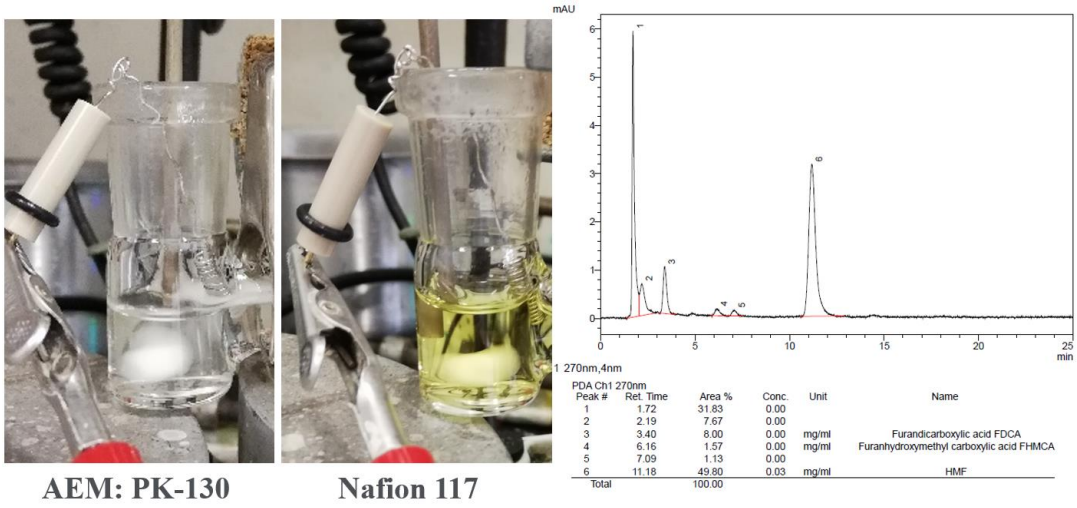

Figure S9. Digital images of the cathode chamber in NiFe-1 catalyzed HMF electro-oxidation in a H-cell using either the PK-130 membrane (left) or the Nafion™ 117 membrane (middle), and the HPLC result of the yellow solution at the cathode chamber using Nafion™ 117 membrane (right).

During the chronoamperometric experiment, the color of the solution at the cathode chamber changed progressively from colorless to light yellow. This phenomenon suggests that the use of Nafion™ 117 (although it is a fresh prepared one) led to a significant crossover of HMF/intermediates/unknown products from the anode to the cathode chamber under high current density electrolysis of HMF with high concentration.

After the HMF electrooxidation (HMF concentration 100 mM), we analyzed the light-yellow solution at the cathode chamber (originally 1 M KOH) by HPLC, but only found a trace of HMF, intermediates and other unknown products that are below the detection limit. This result is also consistent with the conclusions generated from the chronopotentiometry experiments, that membrane is the limitation of the high-concentration HMF (or other substrates) electrooxidation experiments.

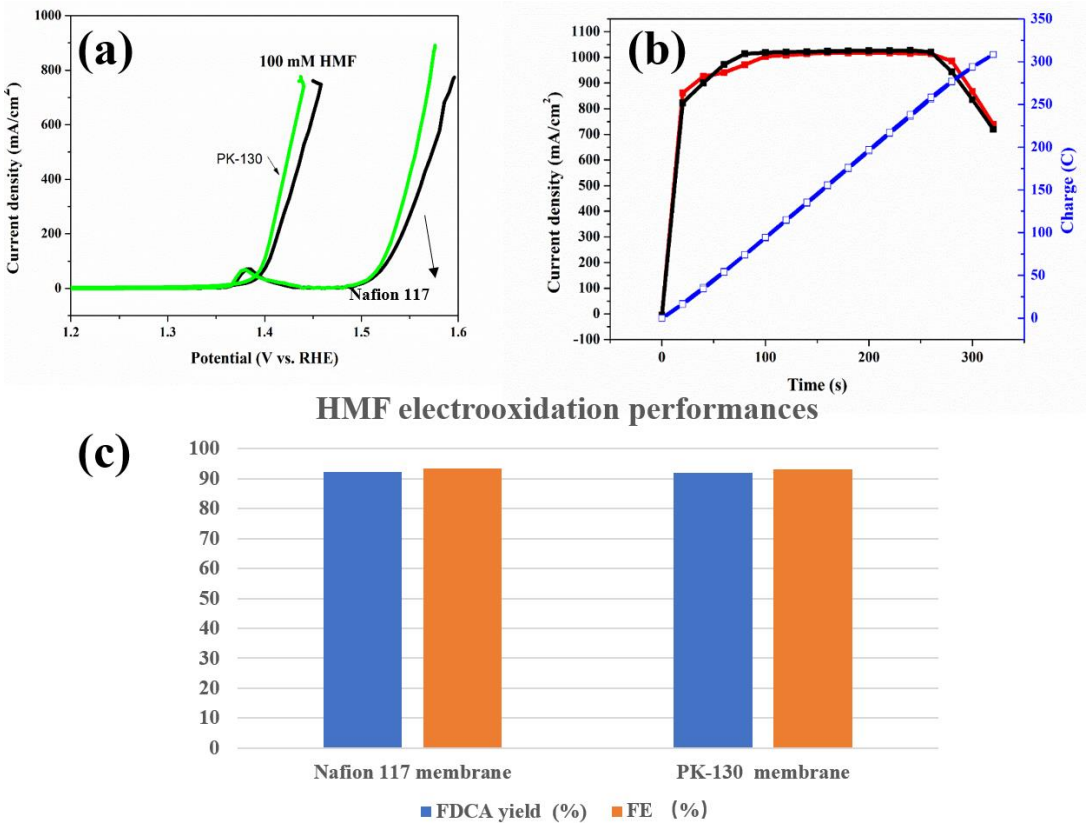

Figure S10. Comparisons of the performances in NiFe-1 catalyzed HMF electro-oxidation in a H-cell using either the Nafion™ 117 membrane or the PK-130 membrane. a) LSV curves, b) Current densities, charges *v.s.* time curves, d) electrocatalytic performances. Reaction condition: 1 M KOH and 100 mM HMF.

Experimental observations suggest that the current response and kenetics of HMF electrolysis over NiFe-1 using PK-130 membrane is only slighly better than that of using Nafion™ 117 membrane, although the final FDCA yields and FEs are almost the same.

5. Extension the synthesis to other non-noble metal modified metal foams and their performances in HMF electro-oxidation

General:

The unified synthesis strategy led to the successful synthesis of various high-performance modified metal foams, as we have exemplified in the electrochemical oxidative upgrading of HMF to FDCA (*vide infra*). Thus, the synthesis could also be extended to the use of other non-noble/noble precursors (e.g., Mg), though in specific cases (e.g., Fe foam) higher thickness foams should be used.
It is also suggested, beyond the Ni, Fe, Cu foams, that other foams (e.g., Co foam, Ti foam) could be used as the matrix for the synthesis of advanced modified metal foams. Together with the results obtained in the NiFe-1 catalyzed, highly efficient and selective oxidative upgrading of various substrates, the scope of the present work can be substantially extended.

5.1 Synthesis

Except for the changes in the precursors and metals foams, the synthesis of other modified metal foams followed the steps described for the synthesis of NiFe-1, which has been given in the experimental section. Those samples were explored for HMF electrooxidation, and the performances at various charges are shown in 5.2.
Moreover, various characterizations of those samples are conducted, and the results are shown in 5.3.

5.2 HMF electro-oxidation over modified metal foams

5.2.1 HMF electro-oxidation over modified Ni foams

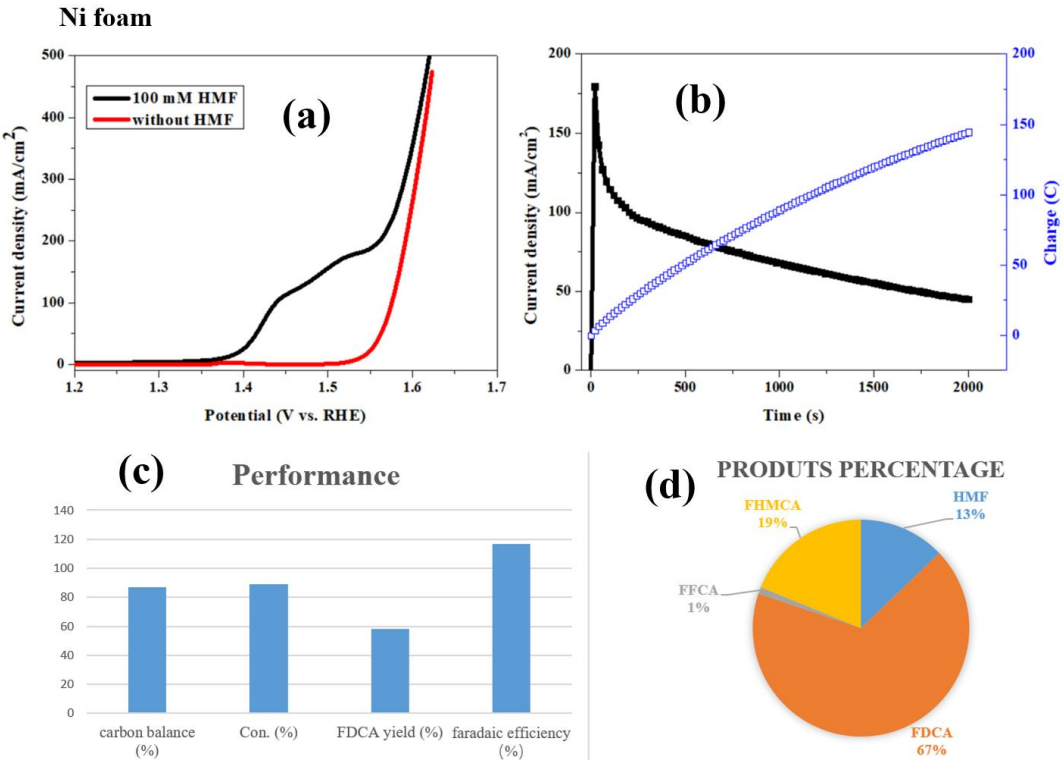

Figure S11. HMF electro-oxidation over Ni foam. a) LSV curves, b) Current densities, charges *v.s.* time curves, c) electrocatalytic performances after passing the charge of 145 C, and d) the percentages of the products and intermediates of the final sample. Reaction condition: 1 M KOH and 100 mM HMF.

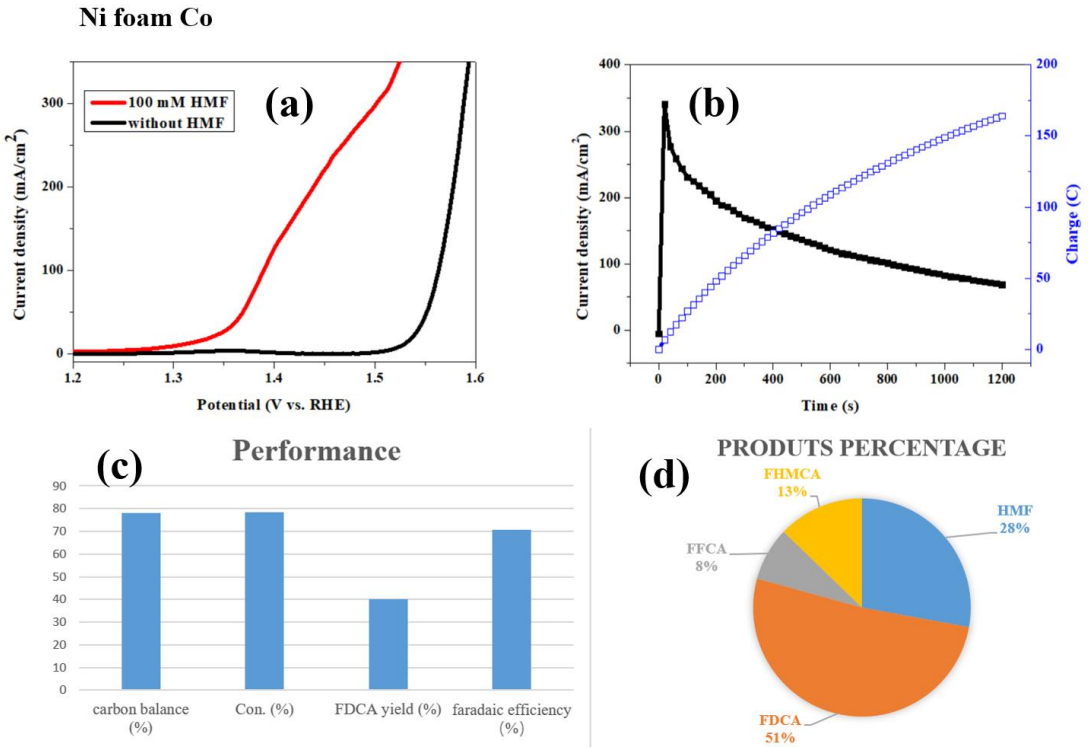

Figure S12. HMF electro-oxidation over Ni foam-Co. a) LSV curves, b) Current densities, charges *v.s.* time curves, c) electrocatalytic performances after passing the charge of 164.2 C, and d) the percentages of the products and intermediates of the final sample. Reaction condition: 1 M KOH and 100 mM HMF.

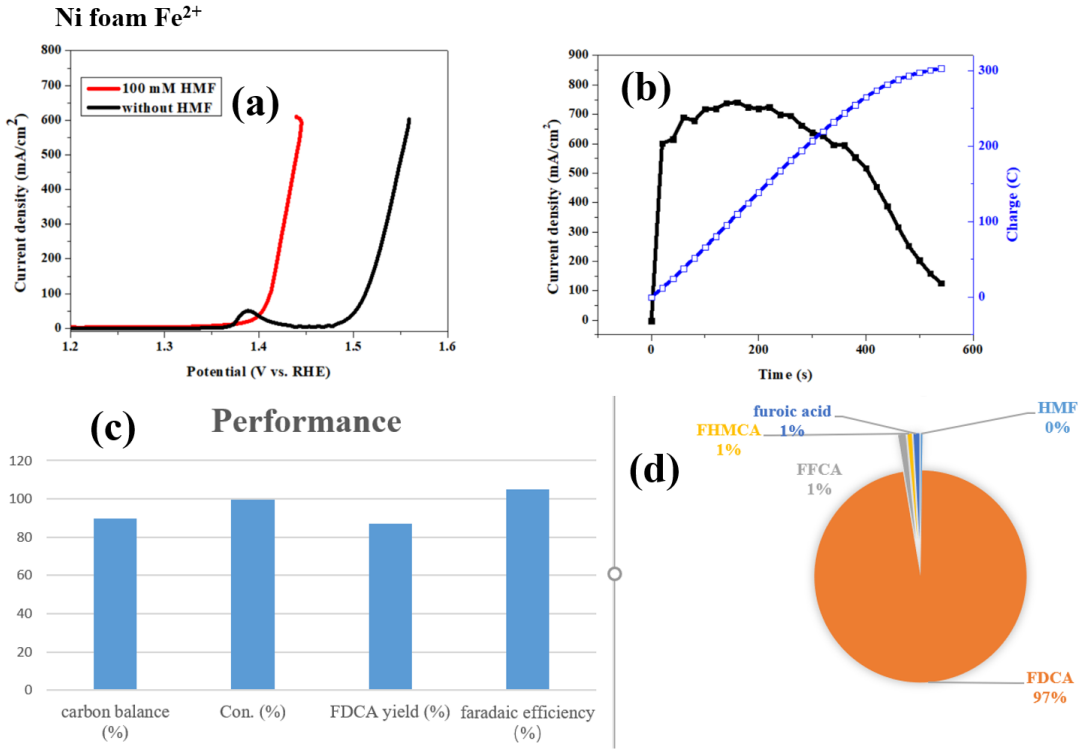

Figure S13. HMF electro-oxidation over Ni foam-Fe^{2+}. a) LSV curves, b) Current densities, charges *v.s.* time curves, c) electrocatalytic performances after passing the charge of 300 C, and d) the percentages of the products and intermediates of the final sample. Reaction condition: 1 M KOH and 100 mM HMF.

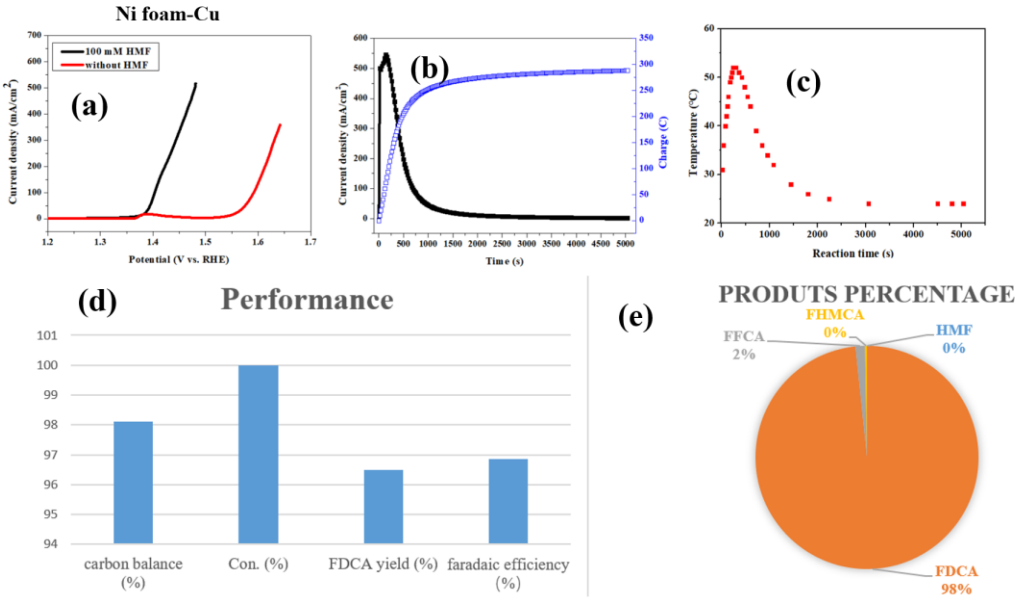

Figure S14. HMF electro-oxidation over Ni foam-Cu. a) LSV curves, b) Current densities, charges *v.s.* time curves, c) Temperature changes *v.s.* time in the cathode chamber measured by an external thermometer, d) electrocatalytic performances after passing the charge of 288.6 C, and e) the percentages of the products and intermediates of the final sample. Reaction condition: 1 M KOH and 100 mM HMF.

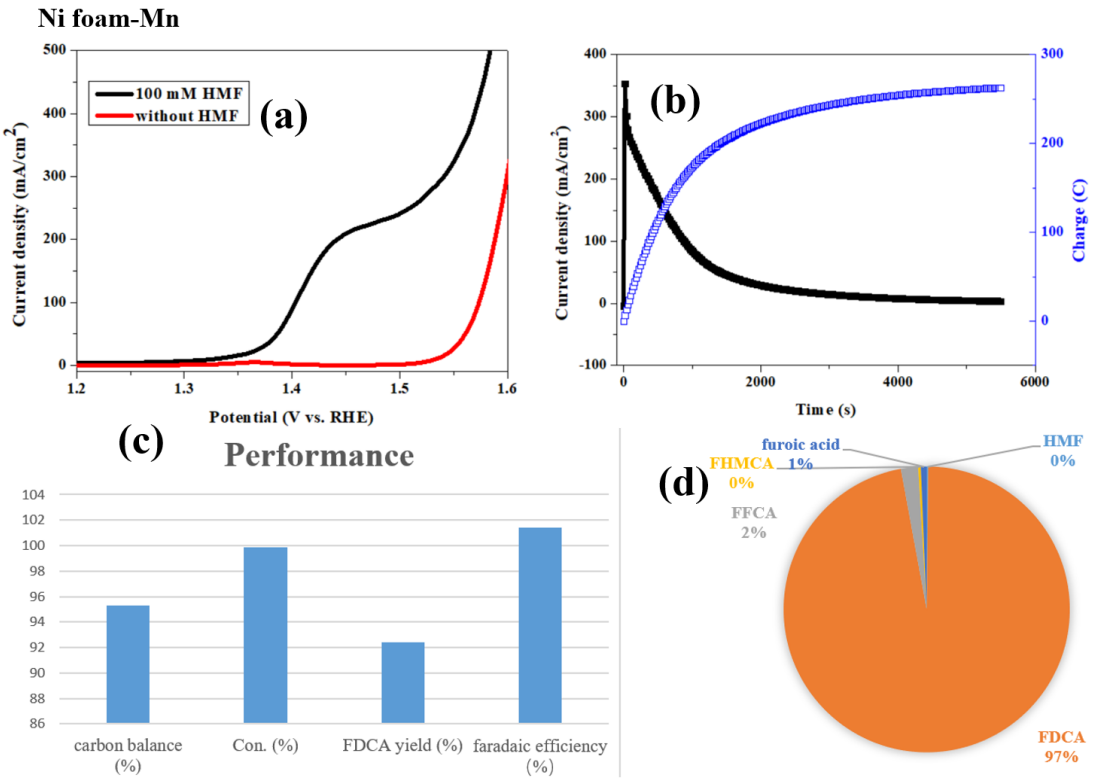

Figure S15. HMF electro-oxidation over Ni foam-Mn. a) LSV curves, b) Current densities, charges *v.s.* time curves, c) electrocatalytic performances after passing the charge of 263 C, and d) the percentages of the products and intermediates of the final sample. Reaction condition: 1 M KOH and 100 mM HMF.

5.2.2 HMF electro-oxidation over modified Fe foams

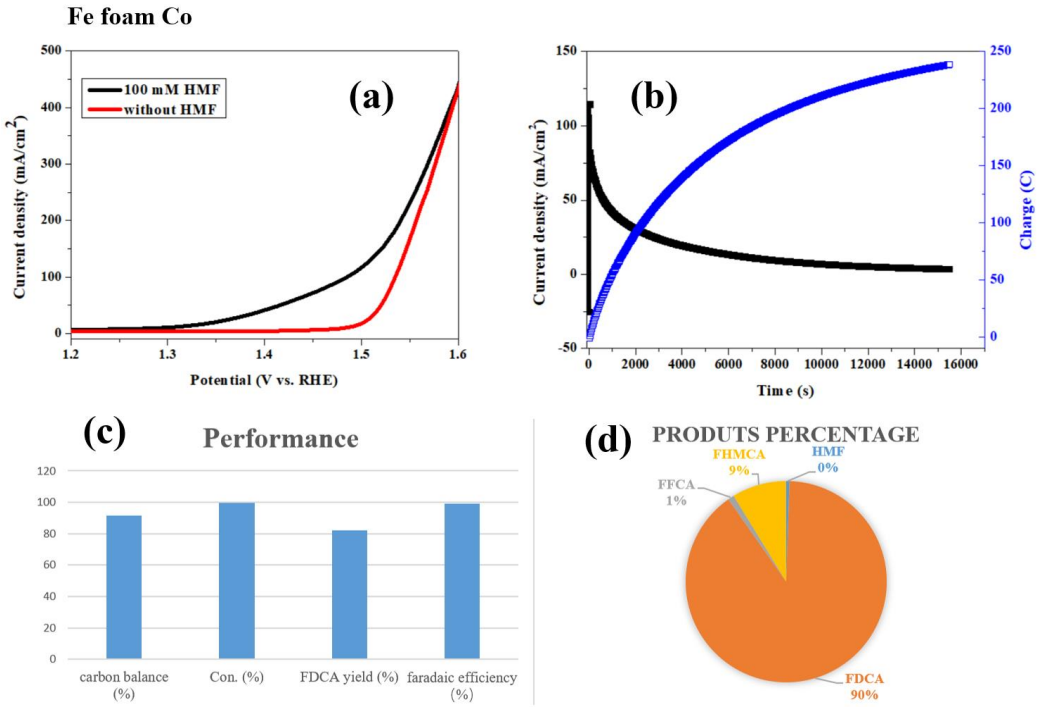

Figure S16. HMF electro-oxidation over Fe foam-Co. a) LSV curves, b) Current densities, charges *v.s.* time curves, c) electrocatalytic performances after passing the charge of 239 C, and d) the percentages of the products and intermediates of the final sample. Reaction condition: 1 M KOH and 100 mM HMF.

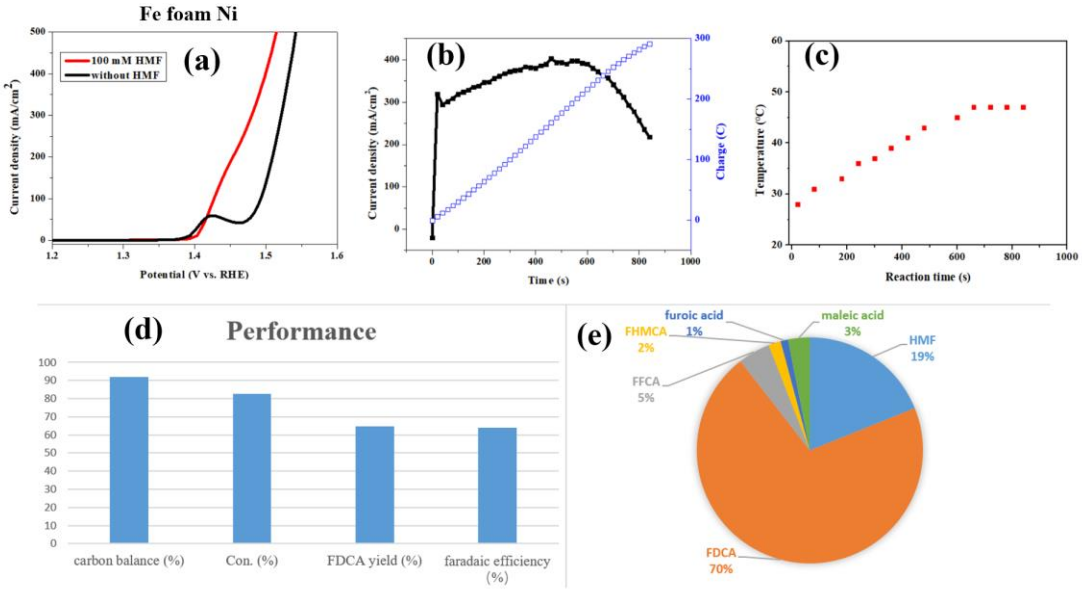

Figure S17. HMF electro-oxidation over Fe foam-Ni. a) LSV curves, b) Current densities, charges *v.s.* time curves, c) Temperature changes *v.s.* time in the cathode chamber measured by an external thermometer, d) electrocatalytic performances after passing the charge of 293.1 C, and e) the percentages of the products and intermediates of the final sample. Reaction condition: 1 M KOH and 100 mM HMF.

Figure S18. Digital figures of the Fe-foam-Cu.

After the synthesis and drying, we took out the sample from the oven. The sample seemed to be good, however, it is very fragile when it was cut for measurements. Thus, the experiments with this sample failed. However, experience and experiments with other modified Fe metal foams suggest that good performance of Fe-foam-Cu could be expected, if Fe-foam with higher thickness would be used.

5.2.3 HMF electro-oxidation over modified Cu foams

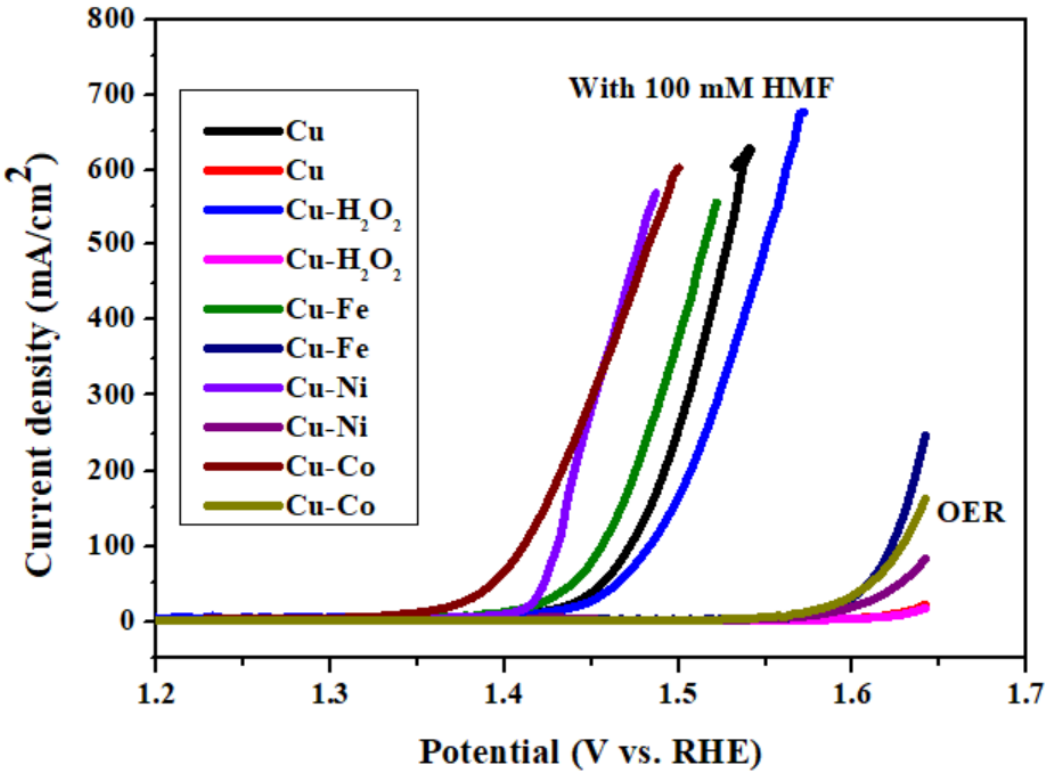

Figure S19. Overview on the HMF electro-oxidation over Cu foam based electrocatalysts: LSV curves. Reaction condition: 1 M KOH and 100 mM HMF.

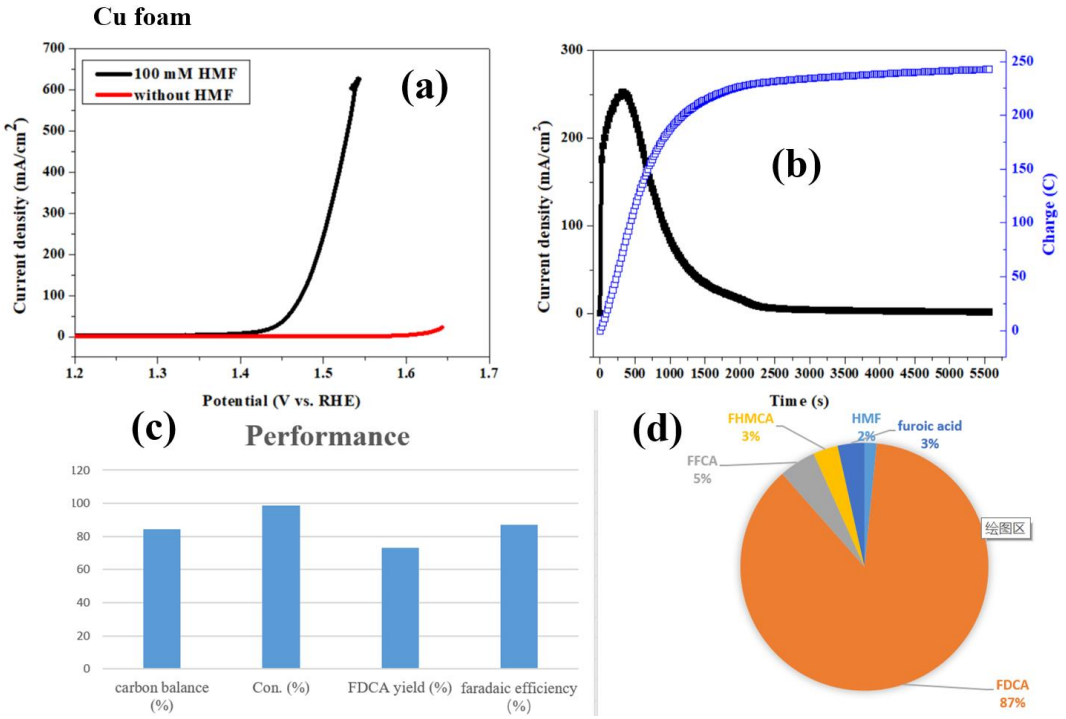

Figure S20. HMF electro-oxidation over Cu foam. a) LSV curves, b) Current densities, charges *v.s.* time curves, c) electrocatalytic performances after passing the charge of 243 C, and e) the percentages of the products and intermediates of the final sample. Reaction condition: 1 M KOH and 100 mM HMF.

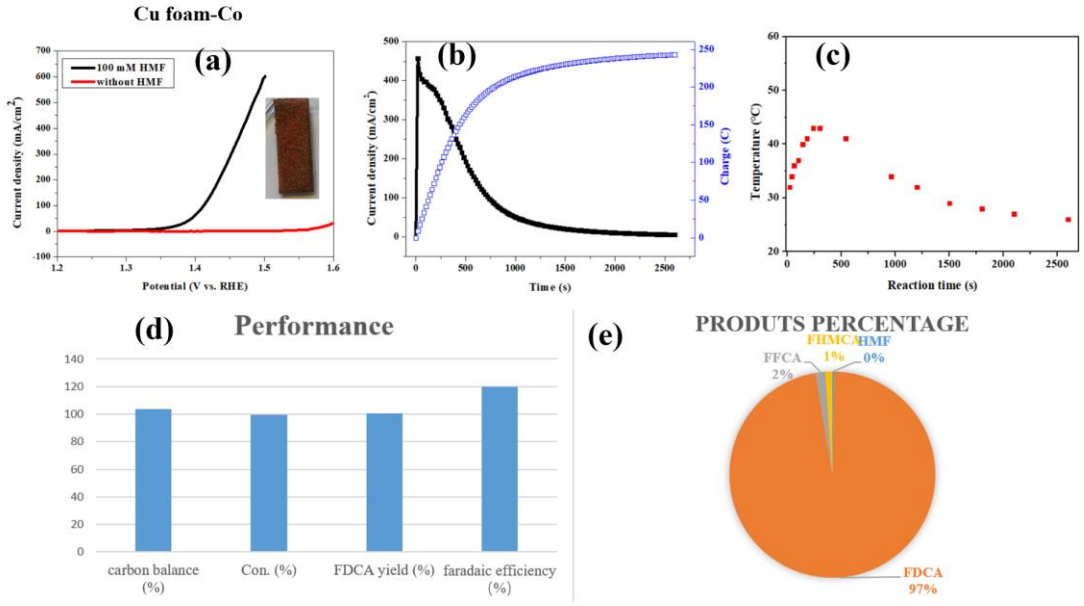

Figure S21. HMF electro-oxidation over Cu foam-Co. a) LSV curves, b) Current densities, charges *v.s.* time curves, c) Temperature changes *v.s.* time in the cathode chamber measured by an external thermometer, d) electrocatalytic performances after passing the charge of 243.2 C, and e) the percentages of the products and intermediates of the final sample. Reaction condition: 1 M KOH and 100 mM HMF.

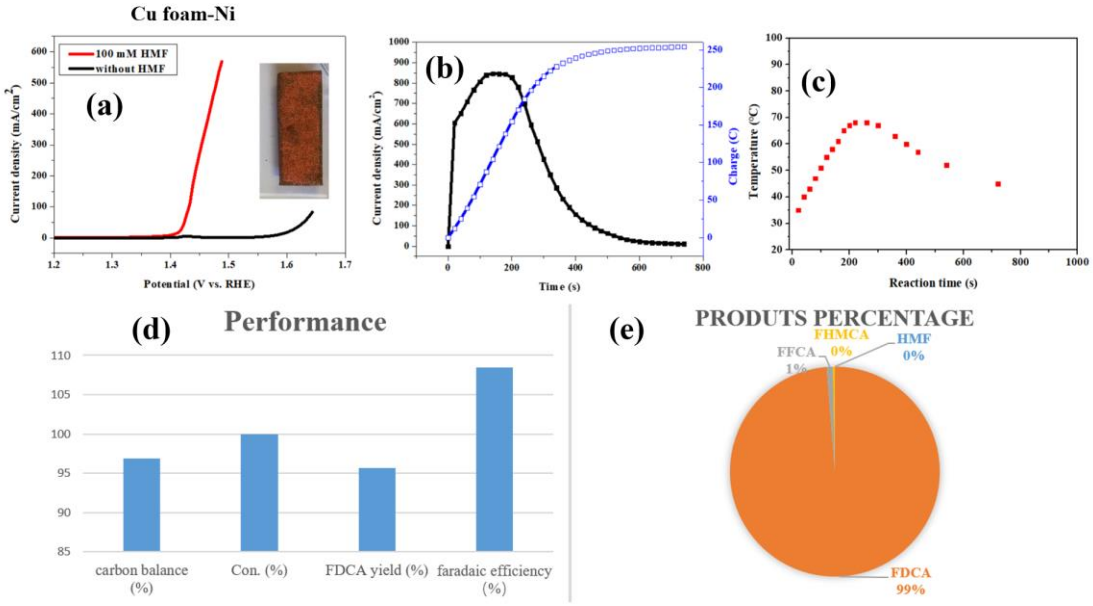

Figure S22. HMF electro-oxidation over Cu foam-Ni. a) LSV curves, b) Current densities, charges *v.s.* time curves, c) Temperature changes *v.s.* time in the cathode chamber measured by an external thermometer, d) electrocatalytic performances after passing the charge of 243.2 C, and e) the percentages of the products and intermediates of the final sample. Reaction condition: 1 M KOH and 100 mM HMF.

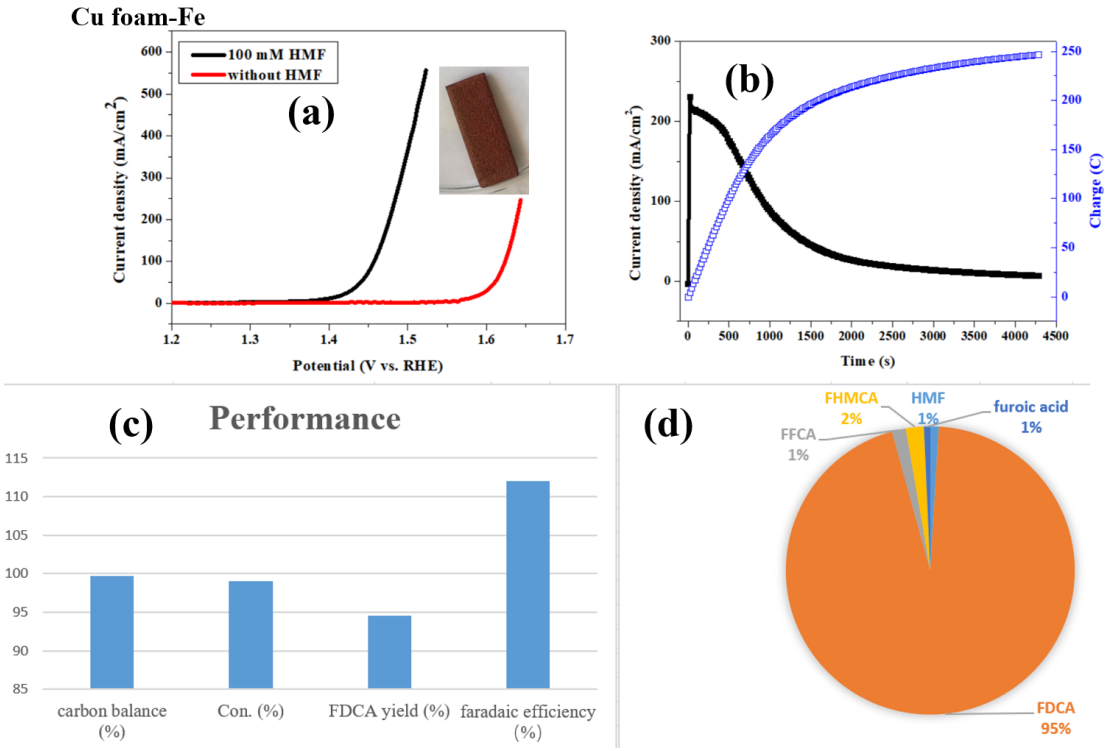

Figure S23. HMF electro-oxidation over Cu foam-Fe. a) LSV curves, b) Current densities, charges *v.s.* time curves, c) electrocatalytic performances after passing the charge of 246.8 C, and e) the percentages of the products and intermediates of the final sample. Reaction condition: 1 M KOH and 100 mM HMF.

5.3 Structural characterizations of the modified metal foams

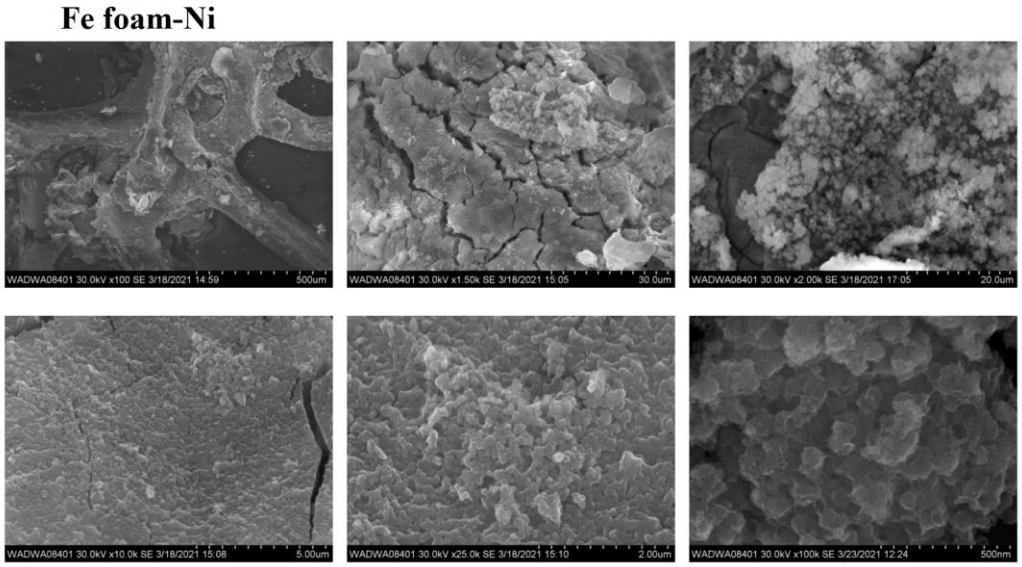

Figure S24. SEM images of **Fe foam-Ni** electrode at different magnifications.

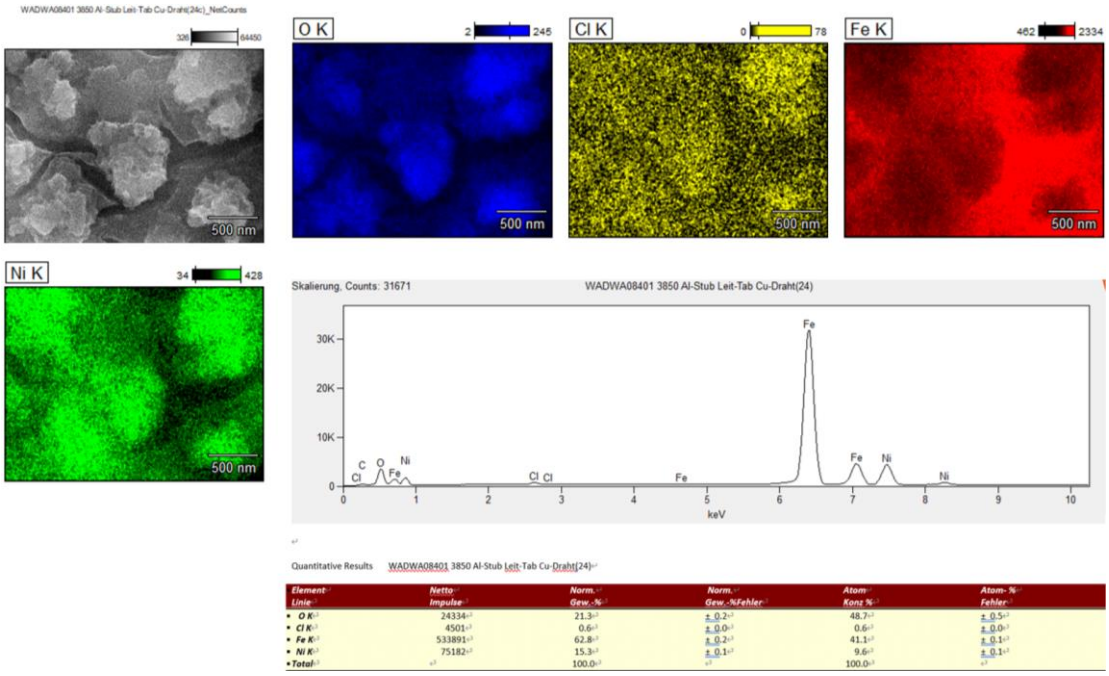

Figure S25. Structural characterizations of **Fe foam-Ni** electrode at the 24 place, including low-magnification SEM images, the corresponding elemental mappings, and point and shoot analyses.

Fe foam-Co

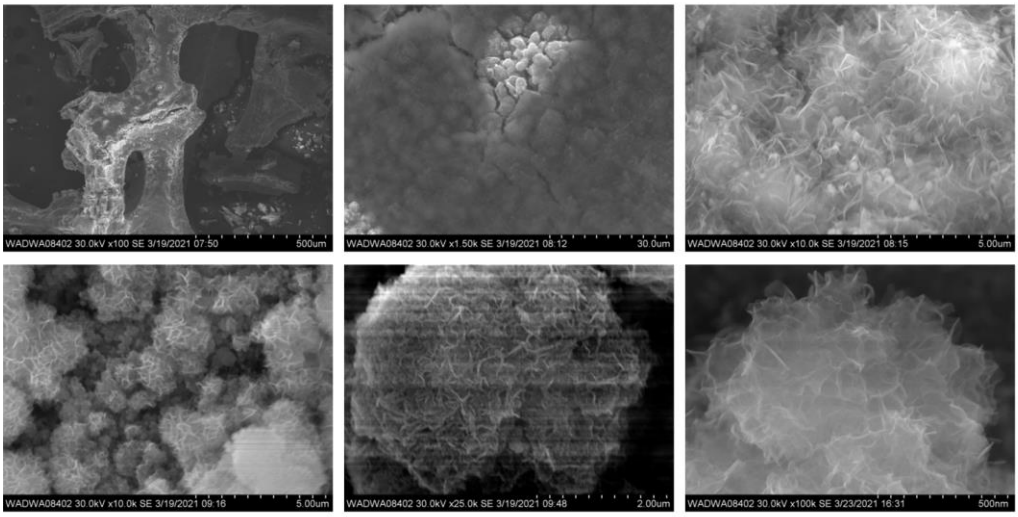

Figure S26. SEM images of **Fe foam-Co** electrode at different magnifications.

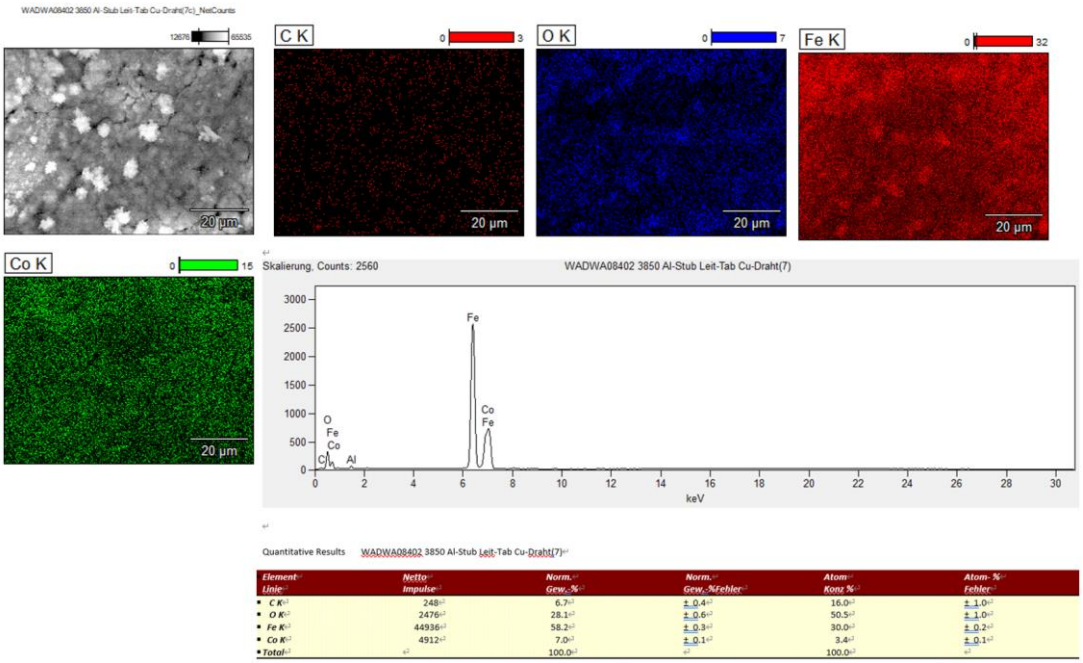

Quantitative Results WADWA08402 3850 Al-Stub Leit-Tab Cu-Draht(7)

Element Linie	Netto Impulse	Norm. Gew.-%	Norm. Gew.-%Fehler	Atom Konz %	Atom-% Fehler
C K	248	6.7	± 0.4	16.0	± 1.0
O K	2476	28.1	± 0.6	50.5	± 1.0
Fe K	44936	58.2	± 0.3	30.0	± 0.2
Co K	4912	7.0	± 0.1	3.4	± 0.1
Total		100.0		100.0	

Figure S27. Structural characterizations of **Fe foam-Co** electrode at the 07 place, including low-magnification SEM images, the corresponding elemental mappings, and point and shoot analyses.

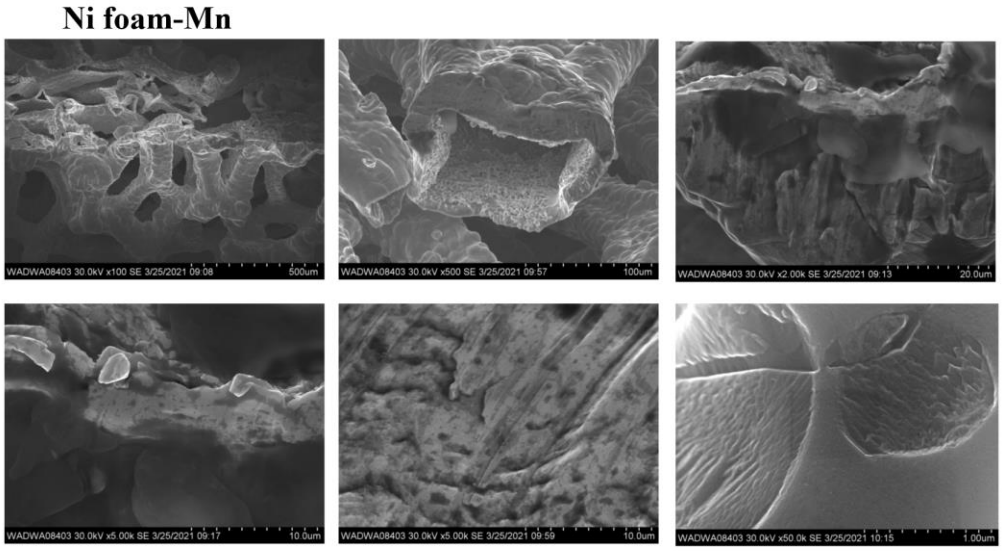

Figure S28. SEM images of **Ni foam-Mn** electrode at different magnifications.

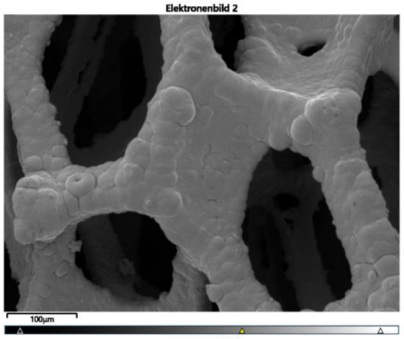

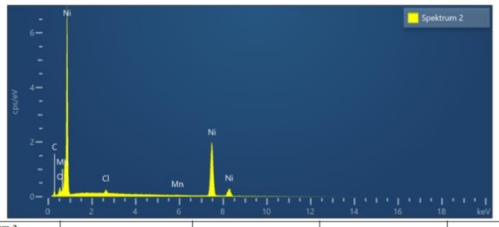

Spektrum 2				
Element	Linientyp	Massen %	Massen % Sigma	Atom %
C	K-Serie	11.82	0.80	38.25
O	K-Serie	1.74	0.19	4.23
Ni	K-Serie	85.57	0.81	56.64
Mn	K-Serie	0.19	0.13	0.13
Cl	K-Serie	0.68	0.08	0.75
Gesamt		100.00		100.00

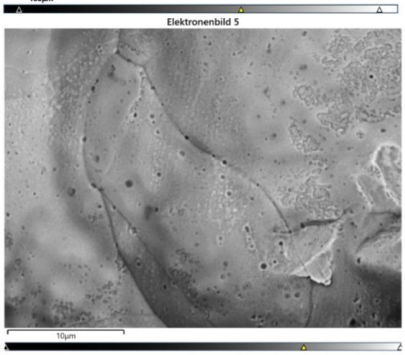

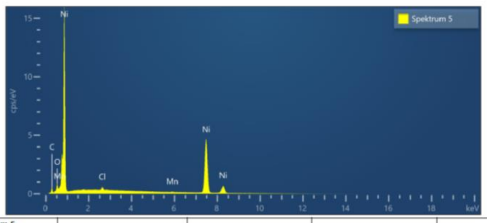

Spektrum 5				
Element	Linientyp	Massen %	Massen % Sigma	Atom %
C	K-Serie	10.59	0.33	35.26
O	K-Serie	1.96	0.08	4.89
Ni	K-Serie	86.62	0.34	59.01
Mn	K-Serie	0.25	0.06	0.18
Cl	K-Serie	0.59	0.03	0.66
Gesamt		100.00		100.00

Figure S29. Structural characterizations of **Fe foam-Co** electrode, including low-magnification SEM images, and the corresponding EDX analyses.

Ni foam-Co

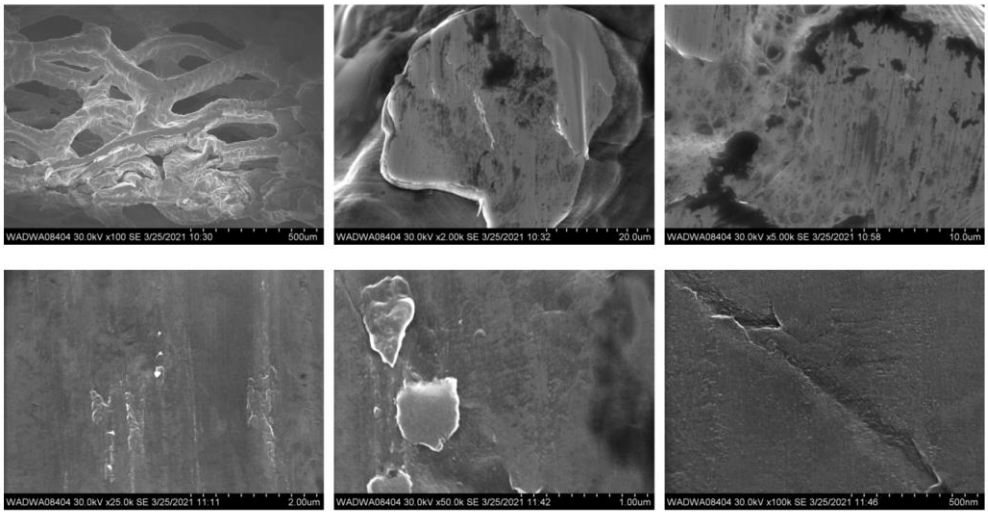

Figure S30. SEM images of **Ni foam-Co** electrode at different magnifications.

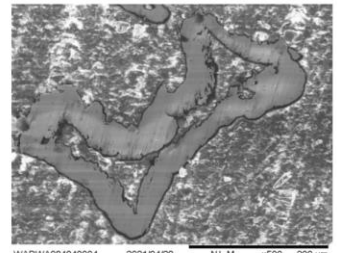

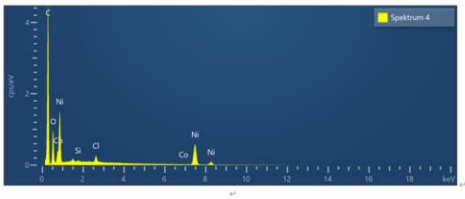

Spektrum 4				
Element	Linientyp	Massen %	Massen % Sigma	Atom %
Si	K-Serie	0.54	0.07	0.69
Ni	K-Serie	73.40	0.22	44.69
O	K-Serie	23.13	0.20	51.67
Co	K-Serie	0.00	0.14	0.00
Cl	K-Serie	2.93	0.07	2.96
Gesamt		100.00		100.00

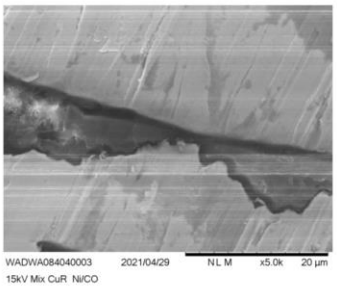

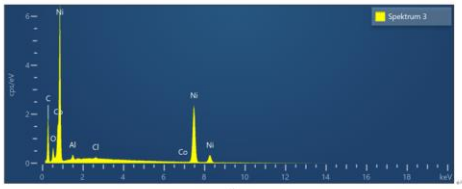

Spektrum 3				
Element	Linientyp	Massen %	Massen % Sigma	Atom %
Ni	K-Serie	94.01	0.22	83.10
Co	K-Serie	0.04	0.15	0.03
O	K-Serie	4.22	0.14	13.69
Al	K-Serie	1.41	0.09	2.72
Cl	K-Serie	0.32	0.06	0.46
Gesamt		100.00		100.00

Figure S31. Structural characterizations of **Ni foam-Co** electrode, including low-magnification SEM images, and the corresponding EDX analyses.

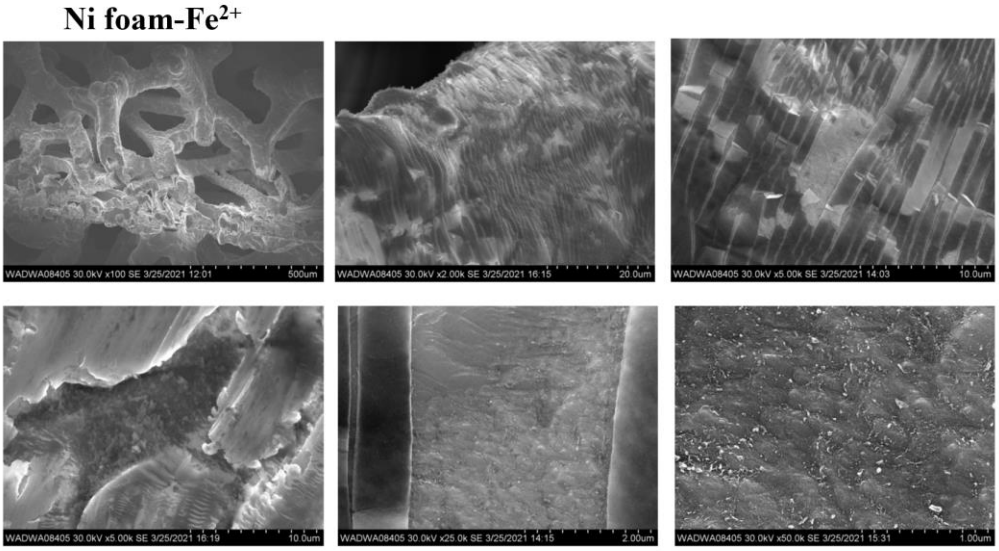

Figure S32. SEM images of **Ni foam-Fe^{2+}** electrode at different magnifications.

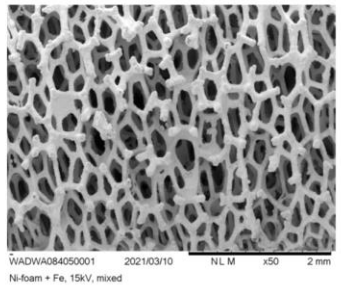

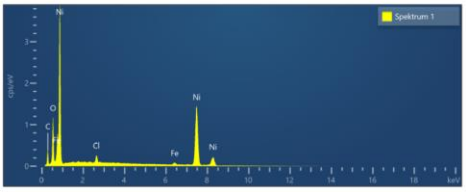

Spektrum 1				
Element	Linientyp	Massen %	Massen % Sigma	Atom %
C	K-Serie	17.56	0.66	43.24
O	K-Serie	11.05	0.25	20.42
Ni	K-Serie	69.24	0.62	34.88
Cl	K-Serie	1.03	0.06	0.86
Fe	K-Serie	1.12	0.13	0.59
Gesamt		100.00		100.00

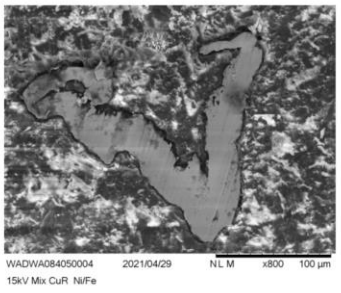

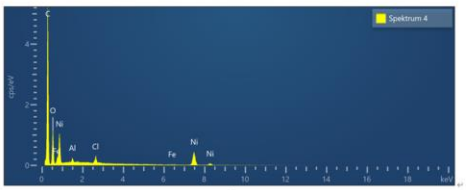

Spektrum 4				
Element	Linientyp	Massen %	Massen % Sigma	Atom %
Ni	K-Serie	61.25	0.82	32.09
Fe	K-Serie	0.11	0.34	0.06
O	K-Serie	31.78	0.73	61.09
Cl	K-Serie	3.88	0.25	3.37
Al	K-Serie	2.98	0.30	3.40
Gesamt		100.00		100.00

Figure S33. Structural characterizations of **Ni foam-Fe^{2+}** electrode, including low-magnification SEM images, and the corresponding EDX analyses.

Cu foam-Fe^{3+}

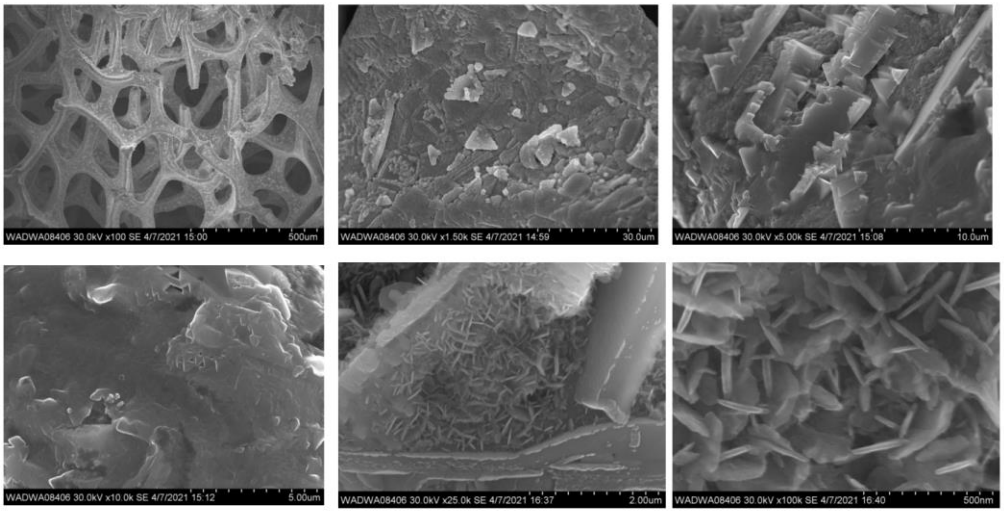

Figure S34. SEM images of **Cu foam-Fe^{3+}** electrode at different magnifications.

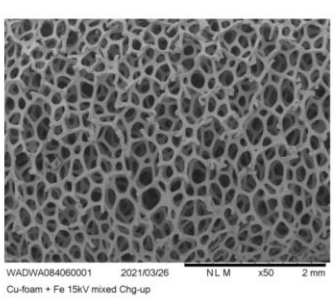

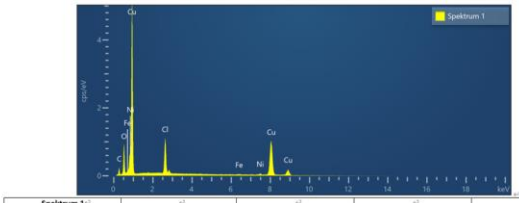

Spektrum 1				
Element	Linientyp	Massen %	Massen % Sigma	Atom %
C	K-Serie	16.01	0.75	40.00
O	K-Serie	12.47	0.27	23.38
Cl	K-Serie	7.36	0.13	6.23
Cu	L-Serie	61.97	0.64	29.26
Fe	K-Serie	0.45	0.14	0.24
Ni	K-Serie	1.74	0.23	0.89
Gesamt		100.00		100.00

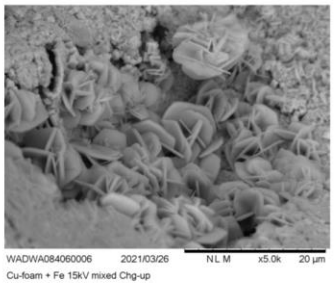

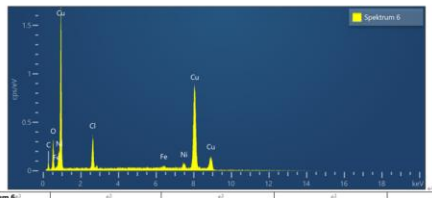

Spektrum 6				
Element	Linientyp	Massen %	Massen % Sigma	Atom %
C	K-Serie	14.86	1.67	39.40
O	K-Serie	10.16	0.55	20.23
Cl	K-Serie	5.96	0.26	5.35
Cu	L-Serie	59.50	1.44	29.82
Ni	K-Serie	8.04	0.84	4.36
Fe	K-Serie	1.47	0.48	0.84
Gesamt		100.00		100.00

Figure S35. Structural characterizations of **Cu foam-Fe^{3+}** electrode, including low-magnification SEM images, and the corresponding EDX analyses.

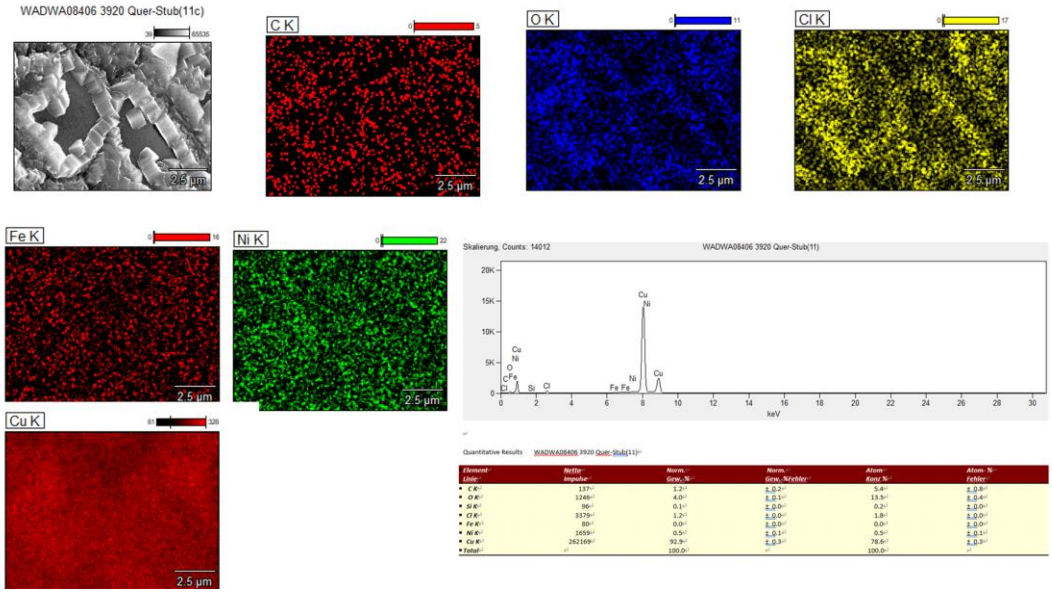

Figure S36. Structural characterizations of **Cu foam-Fe^{3+}** electrode at the 11 place, including low-magnification SEM images, the corresponding elemental mappings, and point and shoot analyses.

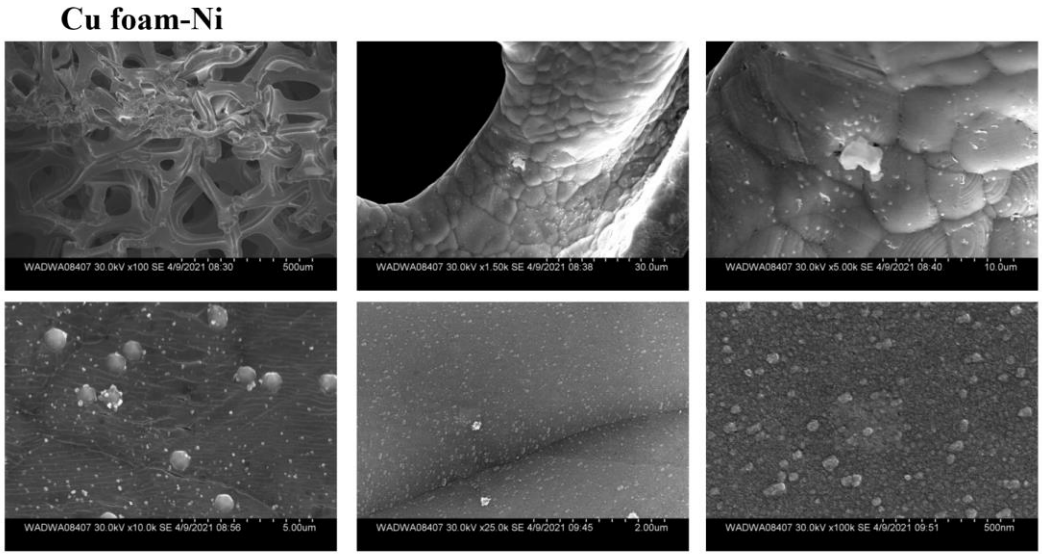

Figure S37. SEM images of **Cu foam-Ni** electrode at different magnifications.

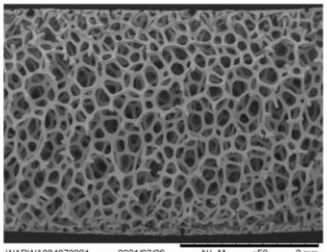

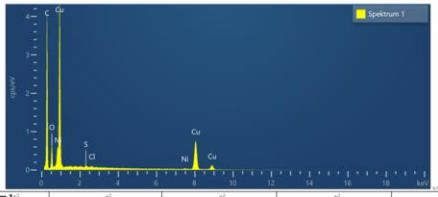

Spektrum 1				
Element	Linientyp	Massen %	Massen % Sigma	Atom %
C	K-Serie	63.97	0.35	85.33
O	K-Serie	7.36	0.20	7.37
Cl	K-Serie	0.11	0.03	0.05
Cu	L-Serie	27.84	0.30	7.02
Ni	K-Serie	0.54	0.12	0.15
S	K-Serie	0.18	0.02	0.09
Gesamt		100.00		100.00

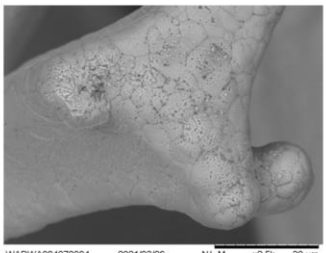

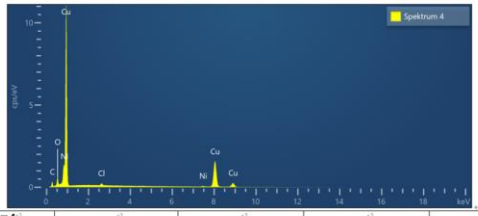

Spektrum 4				
Element	Linientyp	Massen %	Massen % Sigma	Atom %
C	K-Serie	14.21	0.55	42.92
O	K-Serie	4.59	0.15	10.40
Cl	K-Serie	0.57	0.05	0.58
Cu	L-Serie	79.43	0.55	45.35
Ni	K-Serie	1.20	0.18	0.74
Gesamt		100.00		100.00

Figure S38. Structural characterizations of **Cu foam-Ni** electrode, including low-magnification SEM images, and the corresponding EDX analyses.

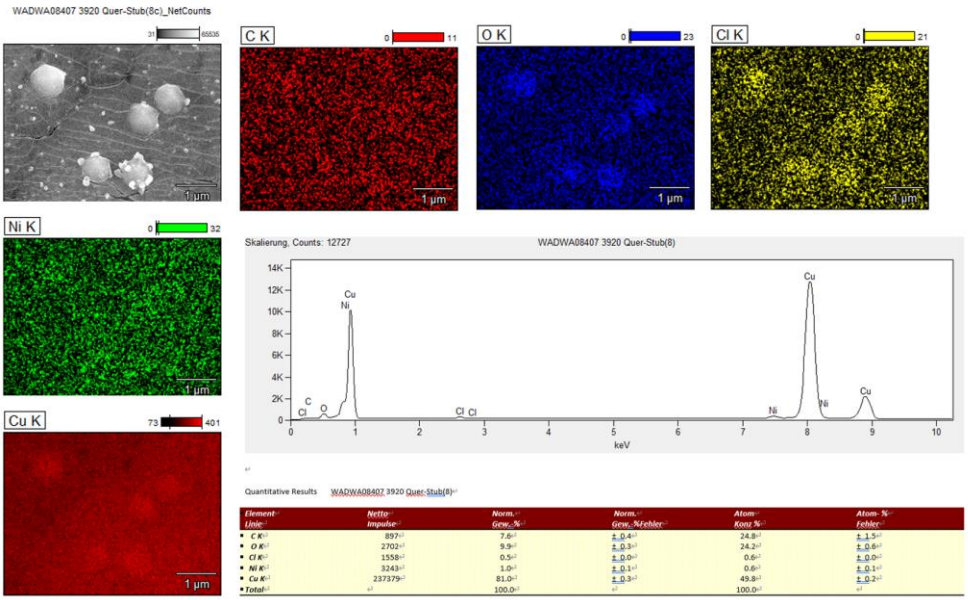

Figure S39. Structural characterizations of **Cu foam-Ni** electrode at the 11 place, including low-magnification SEM images, the corresponding elemental mappings, and point and shoot analyses.

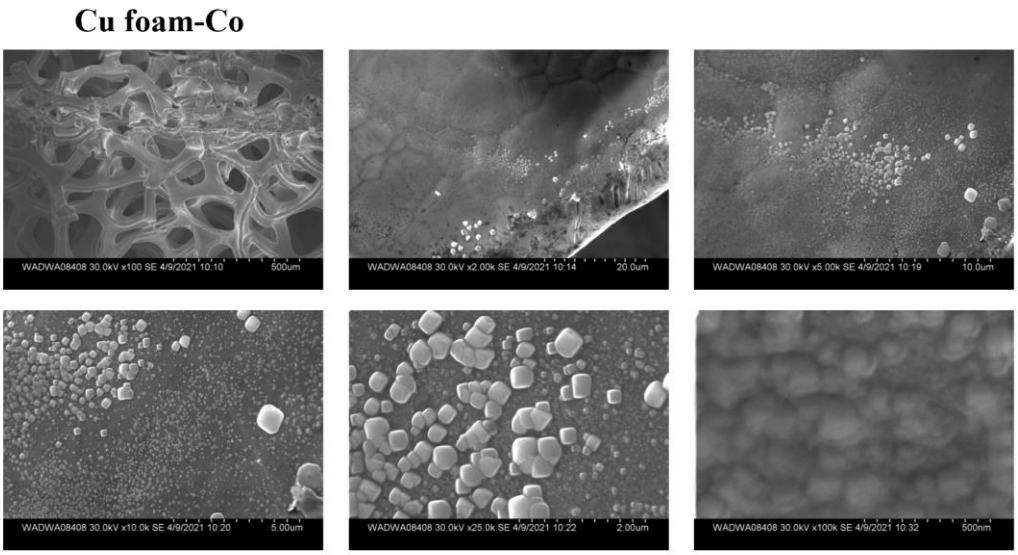

Figure S40. SEM images of **Cu foam-Co** electrode at different magnifications.

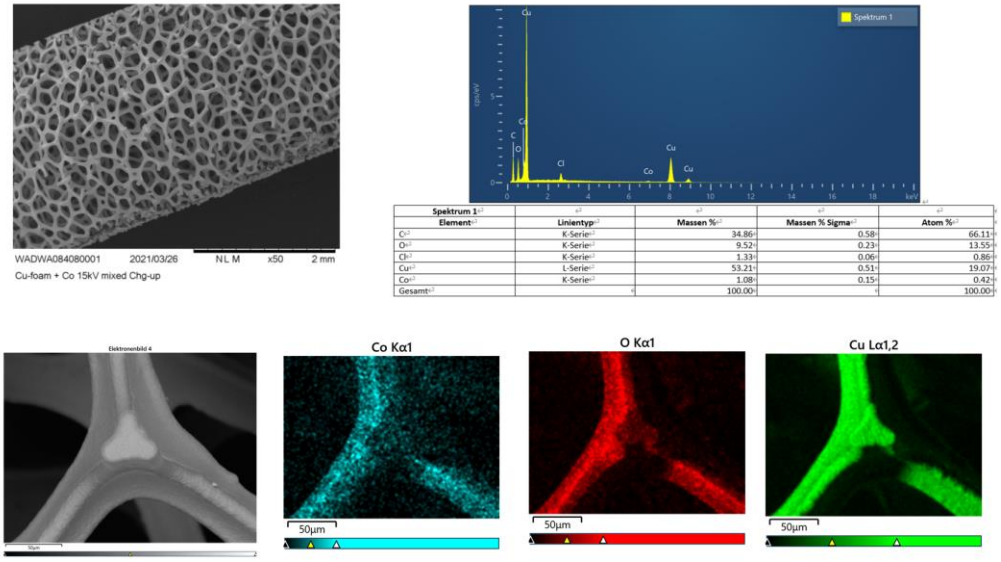

Spektrum 1				
Element	Linientyp	Massen %	Massen % Sigma	Atom %
C	K-Serie	34.86	0.58	66.11
O	K-Serie	9.52	0.23	13.55
Cl	K-Serie	1.33	0.06	0.86
Cu	L-Serie	53.21	0.51	19.07
Co	K-Serie	1.08	0.15	0.42
Gesamt		100.00		100.00

Figure S41. Structural characterizations of **Cu foam-Co** electrode, including low-magnification SEM images, EDX and the corresponding elemental mappings.

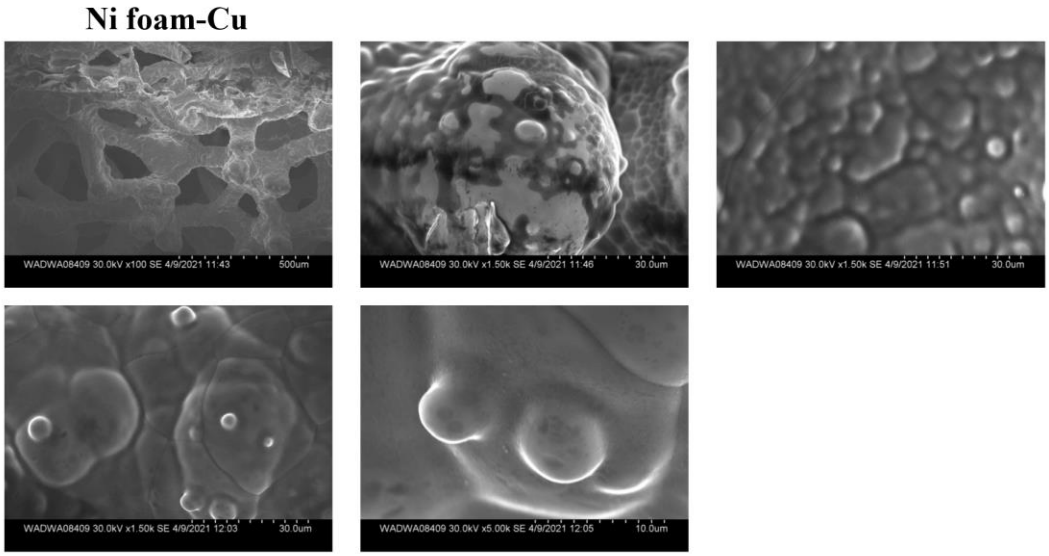

Figure S42. SEM images of **Ni foam-Cu** electrode at different magnifications.

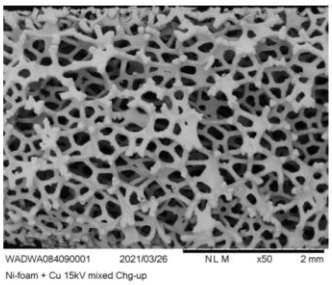

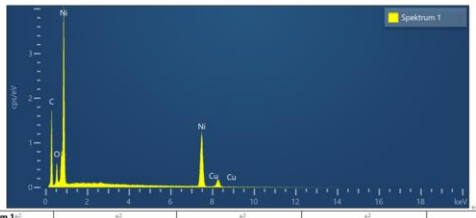

Spektrum 1				
Element	Linientyp	Massen %	Massen % Sigma	Atom %
C	K-Serie	46.33	0.59	76.72
O	K-Serie	5.64	0.23	7.02
Ni	K-Serie	47.98	0.58	16.25
Cu	L-Serie	0.04	0.51	0.01
Gesamt		100.00		100.00

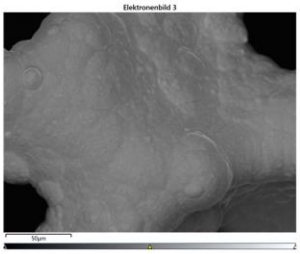

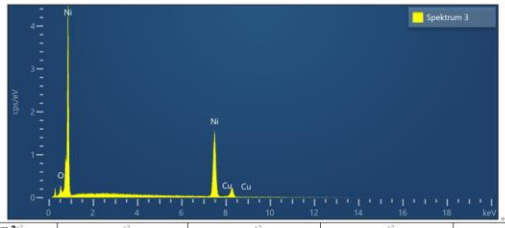

Spektrum 3				
Element	Linientyp	Massen %	Massen % Sigma	Atom %
O	K-Serie	2.08	0.24	7.22
Ni	K-Serie	96.24	1.57	91.30
Cu	L-Serie	1.68	1.59	1.47
Gesamt		100.00		100.00

Figure S43. Structural characterizations of **Ni foam-Cu** electrode, including low-magnification SEM images, and EDX.

6. Electrochemical characterizations of various electrodes

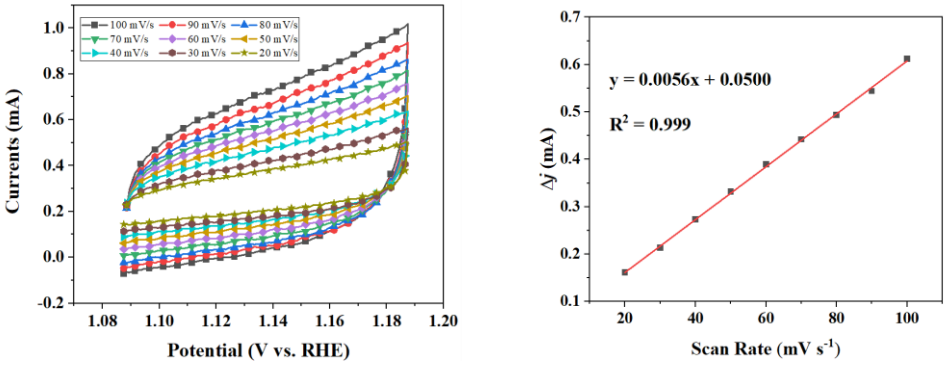

Figure S44. CV curves of NiFe-1 electrode with 100 mM HMF at different scan rates (left), and charging current differences ($\Delta j = j_{anode} - j_{cathode}$) plotted against scan rates (right).

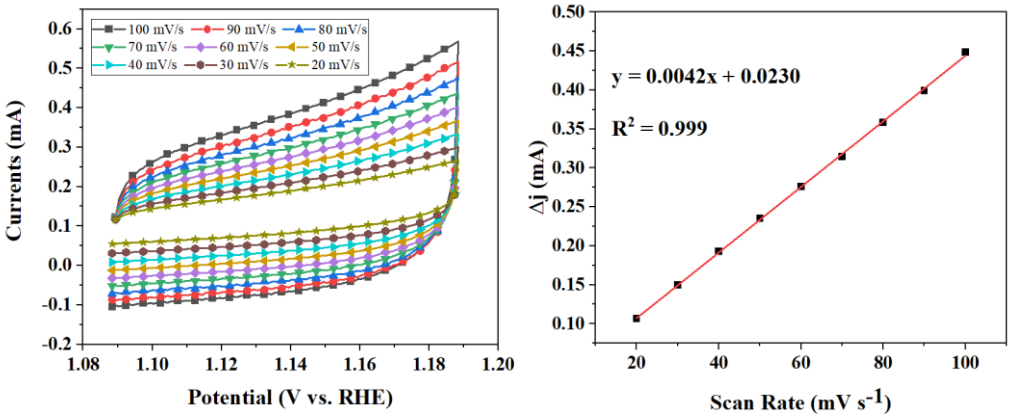

Figure S45. CV curves of Nickel foam electrode with 100 mM HMF at different scan rates (left), and charging current differences ($\Delta j = j_{anode} - j_{cathode}$) plotted against scan rates (right).

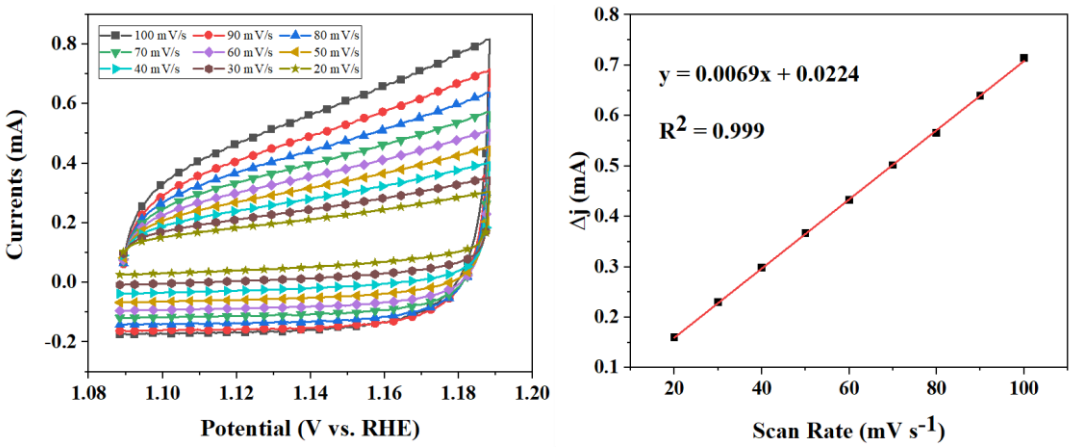

Figure S46. CV curves of Nickel foam-H_2O_2 electrode with 100 mM HMF at different scan rates (left), and charging current differences ($\Delta j = j_{anode} - j_{cathode}$) plotted against scan rates (right).

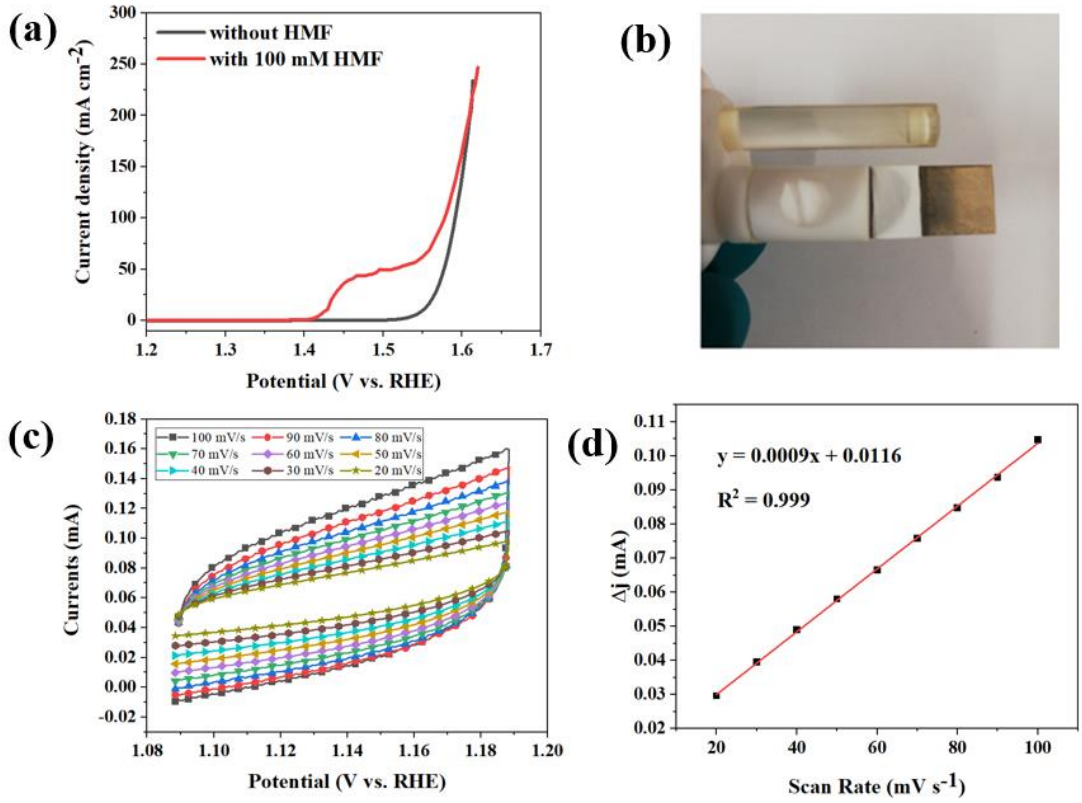

Figure S47. a) LSV curves for NiFe-1 (using nickel plate instead of nickel foam) electrode in 1 M KOH with and without 100 mM HMF. b) digital figure of the working electrode, and CV curves of NiFe-1 (using nickel plate instead of nickel foam) electrode with 100 mM HMF at different scan rates (c), and charging current differences ($\Delta j = j_{anode} - j_{cathode}$) plotted against scan rates (d).

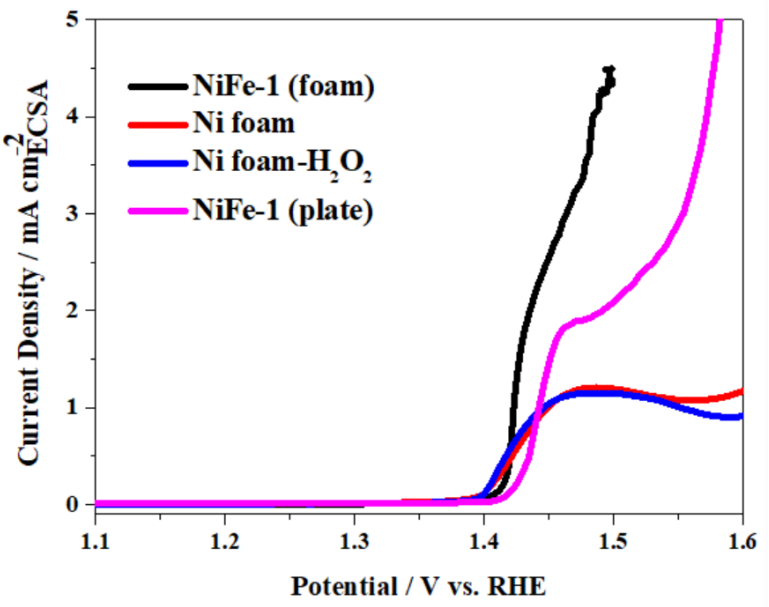

Figure S48. LSV curves in the presence of 100 mM HMF over different electrodes after normalized by ECSA.

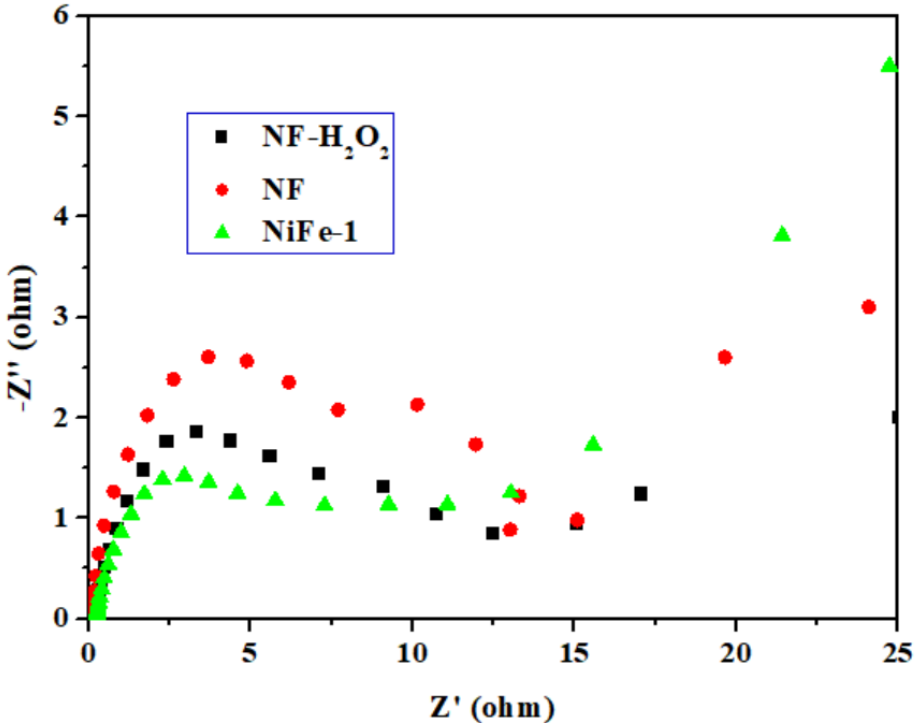

Figure S49. Nyquist plots over NiFe-1 electrode in comparisons with the H_2O_2 treated NF and the purified NF in the presence of 50 mM HMF at 1.437 V (vs. RHE).

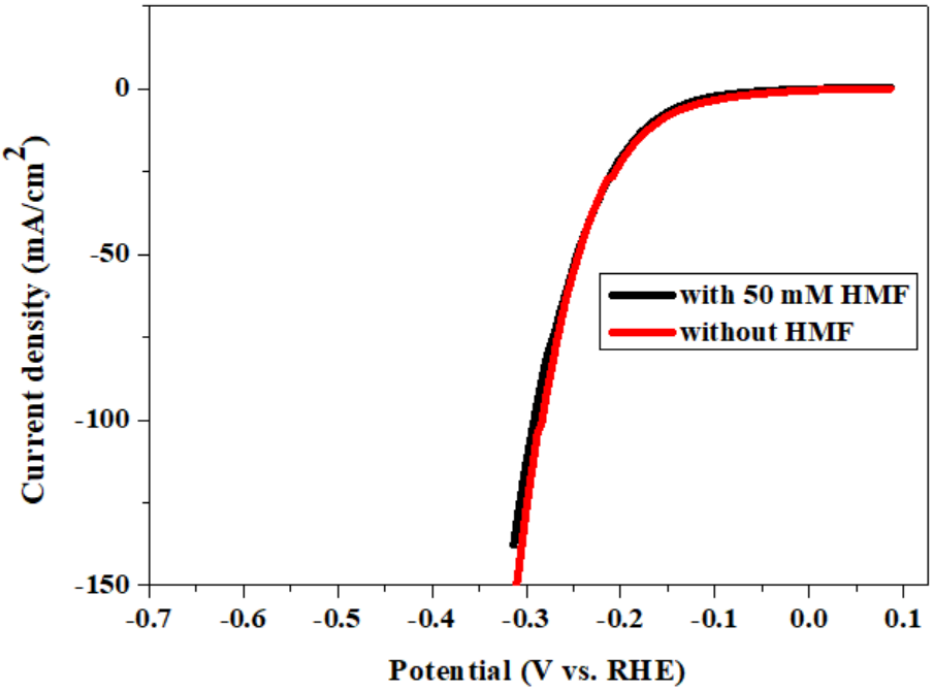

Figure S50. LSV curves of the HER over NiFe-1 electrode in 1 M KOH with and without 50 mM HMF.

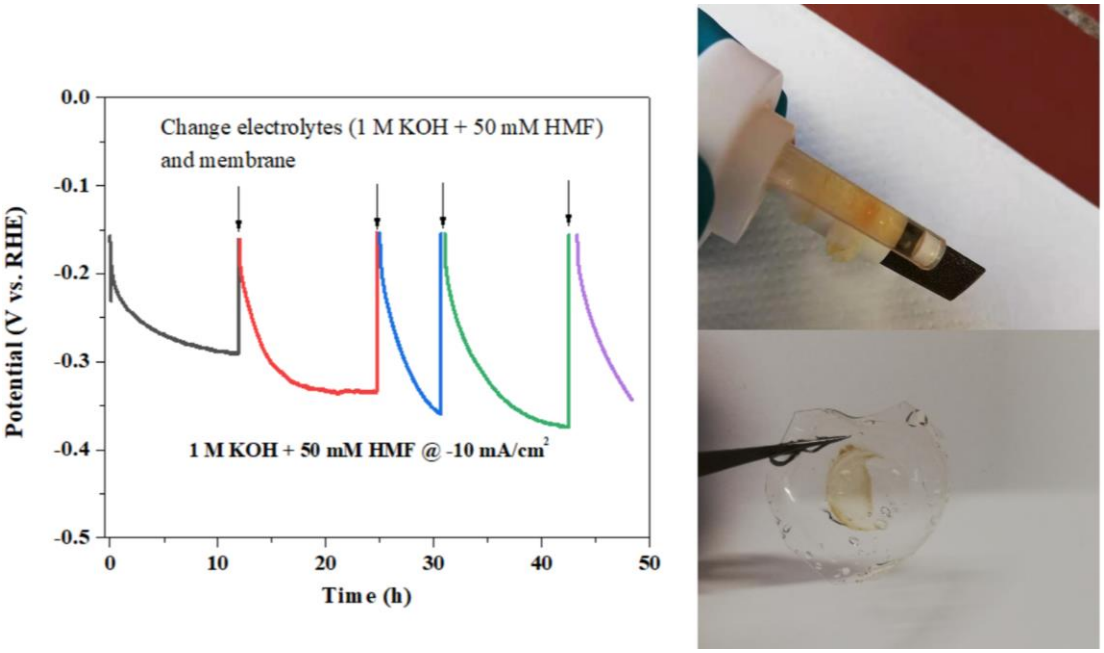

Figure S51. Chronopotentiometry curves of NiFe-1 electrode collected at -10 mA/cm^2 in 1 M KOH with 50 mM HMF (left), and the contaminated reference electrode and membrane after the first chronopotentiometry experiment (right).

*When conducting the initial chronopotentiometry experiment, we observed that the required potential at -10 mA/cm^2 continuously decreased. The bad performance was thus tentatively ascribed to the poor electrode stability. However, when the H-cell was washed, the membrane was found to be contaminated/damanaged, possibly due to the crossover between the membrane and HMF or/and the degradation products (***Figure S9***). Also the reference electrode and the working electrode were contaminated. Therefore, the electrodes were simply washed using ultra-pure water, the membrane and the electrolytes were changed, and the experiments was repeated. The required potential at -10 mA/cm^2 still continuously decreased, but the initinal potential for -10 mA/cm^2 was identical in subsequent runs, proving the high stability of the electrode.*
When comparing electrochemcial peroformances for HMF oxidation in an H-cell using either the Nafion™ 117 membrane or the PK-130 membrane, the same phenomena were observed (vide infra). Contaminated membranes may thus be the limitation for high-concentration HMF electrooxidation experiments, and this might also be true for other substrates.

7. Characterizations of the NiFe-1 electrode before and after HMF electro-oxidation reactions

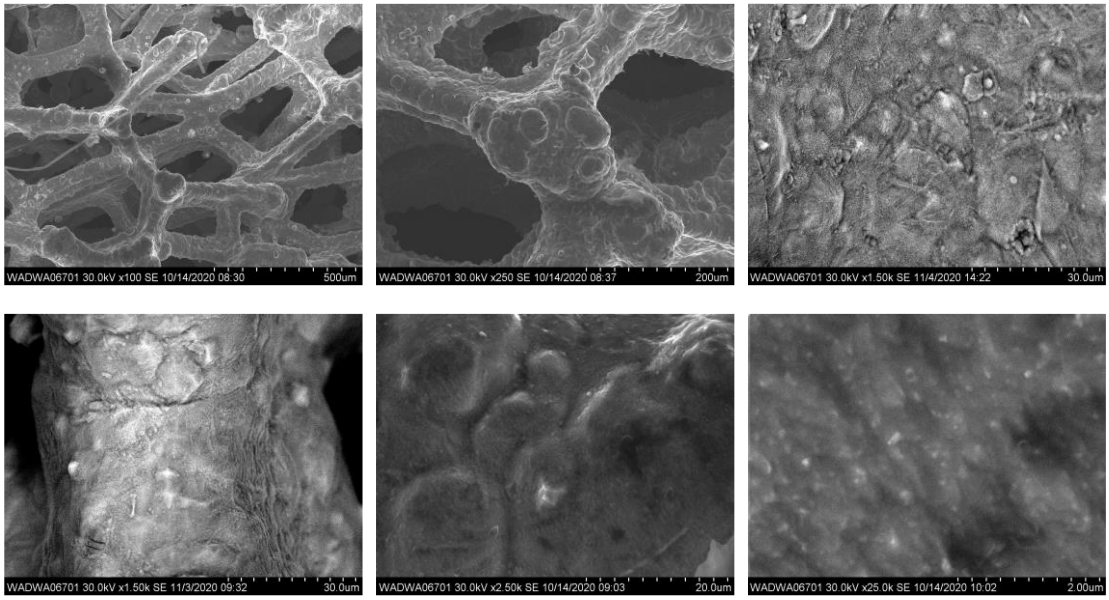

Figure S52. SEM images of fresh NiFe-1 electrode at different magnifications.

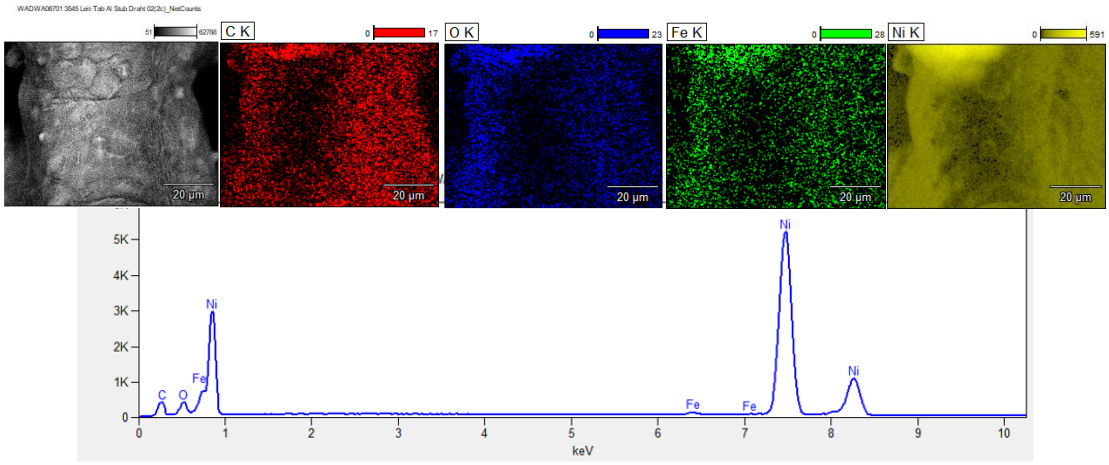

Quantitative Results WADWA06701 3545 Leit-Tab Al Stub Draht 02(2)

Element Linie	Netto Impulse	Norm. Gew.-%	Norm. Gew.-%Fehler	Atom Konz.%	Atom-% Fehler
C K	3082	20.4	± 0.4	44.5	± 1.0
O K	2563	16.8	± 0.8	27.5	± 1.3
Fe K	1149	0.5	± 0.1	0.2	± 0.0
Ni K	95347	62.3	± 0.3	27.8	± 0.2
Total		100.0		100.0	

Figure S53. Structural characterizations of fresh NiFe-1 electrode at the 02(2c) place, including low-magnification SEM images, the corresponding elemental mappings, and point and shoot analyses.

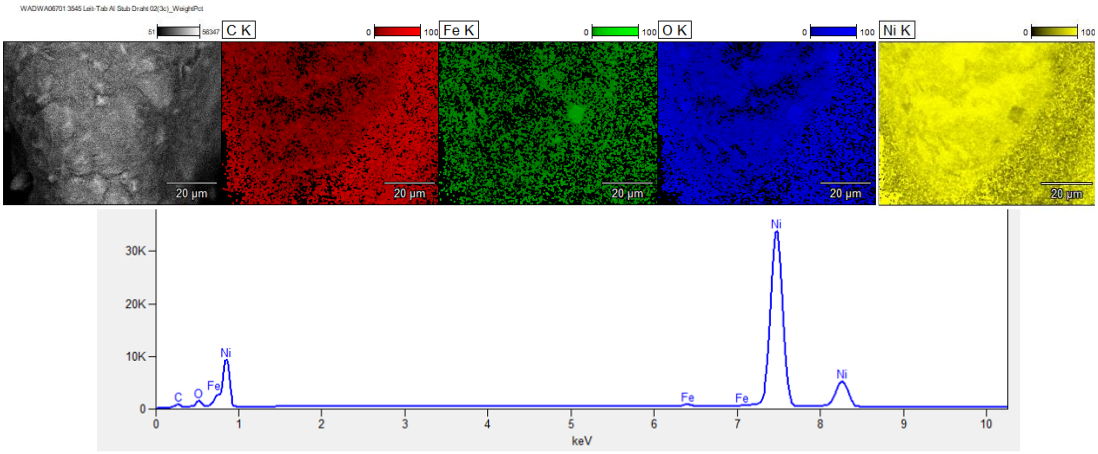

Quantitative Results WADWA06701 3545 Leit-Tab Al Stub Draht 02(3)

Element Linie	Netto Impulse	Norm. Gew.-%	Norm. Gew.-%Fehler	Atom Kanz %	Atom- % Fehler
C K	5039	7.7	± 0.1	24.3	± 0.5
O K	8473	9.4	± 0.2	22.3	± 0.6
Fe K	6740	0.6	± 0.0	0.4	± 0.0
Ni K	613160	82.2	± 0.2	53.0	± 0.1
Total		100.0		100.0	

Figure S54. Structural characterizations of fresh NiFe-1 electrode at the 02(3c) place, including low-magnification SEM images, the corresponding elemental mappings, and point and shoot analyses.

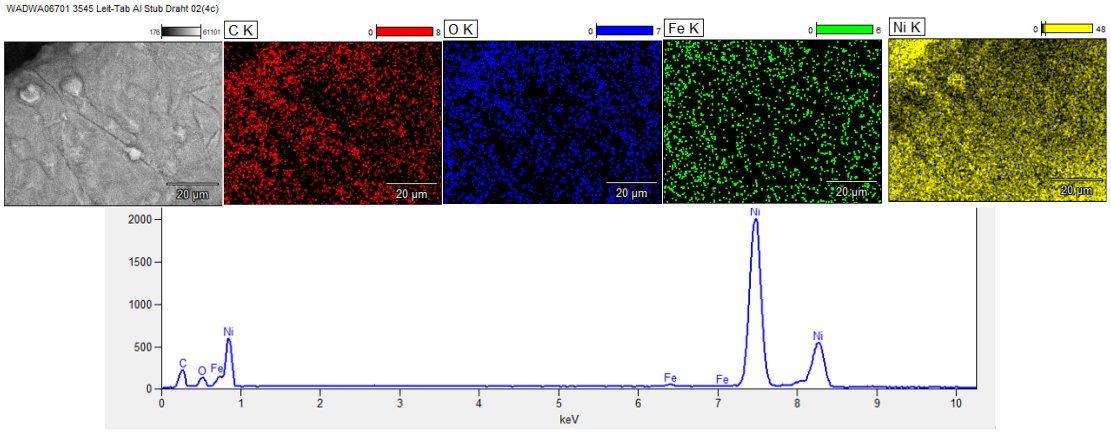

Quantitative Results WADWA06701 3545 Leit-Tab Al Stub Draht 02(4)

Element Linie	Netto Impulse	Norm. Gew.-%	Norm. Gew.-%Fehler	Atom Konz.%	Atom-% Fehler
C K	1556	25.0	± 0.7	52.4	± 1.5
O K	763	13.4	± 0.7	21.2	± 1.0
Fe K	487	0.5	± 0.1	0.2	± 0.0
Ni K	37775	61.1	± 0.5	26.2	± 0.2
Total		100.0		100.0	

Figure S55. Structural characterizations of fresh NiFe-1 electrode at the 02(4c) place, including low-magnification SEM images, the corresponding elemental mappings, and point and shoot analyses.

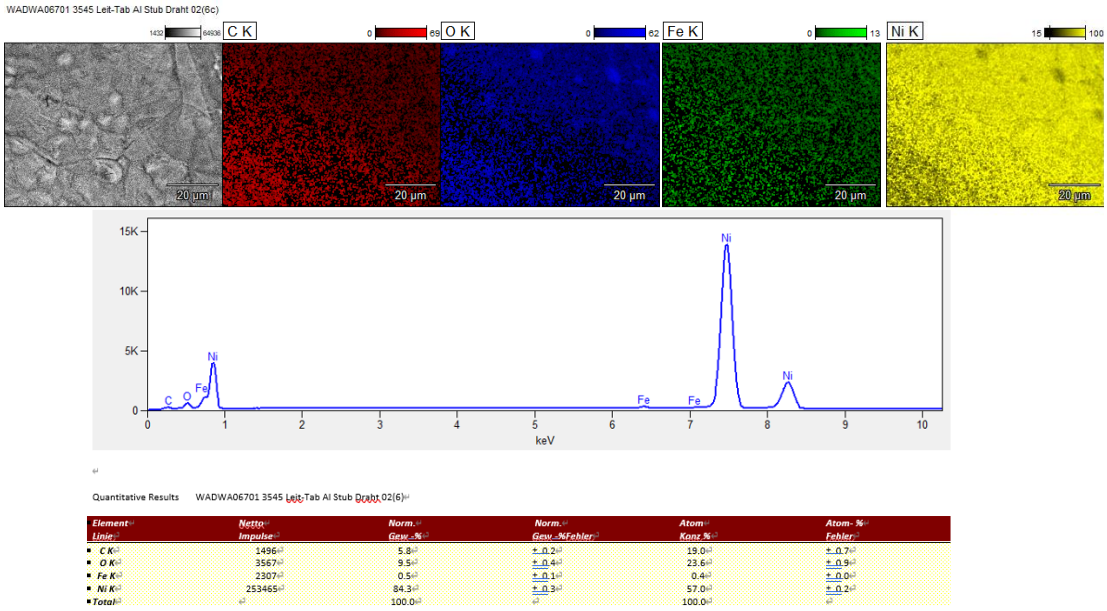

Figure S56. Structural characterizations of fresh NiFe-1 electrode at the 02(6c) place, including low-magnification SEM images, the corresponding elemental mappings, and point and shoot analyses.

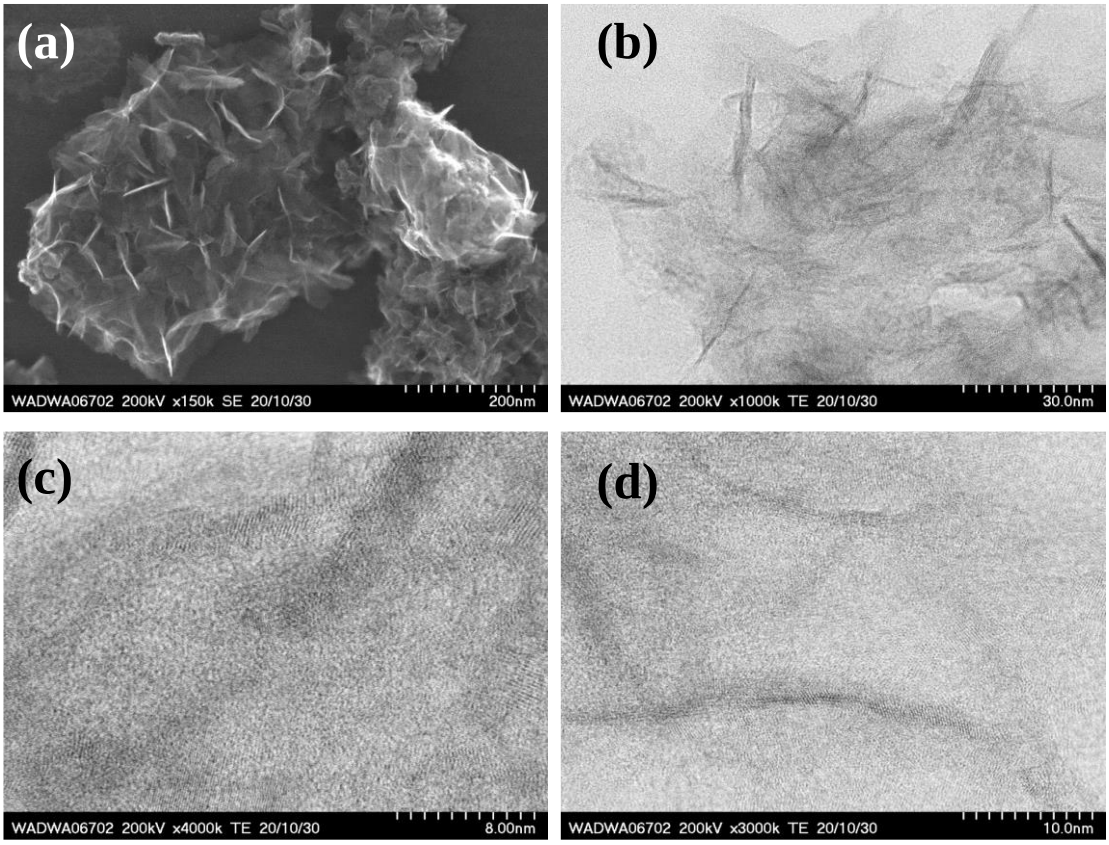

Figure S57. Electron microscope images of the **fresh** NiFe-1 after sonication the Fe modified NF in water: a) secondary electron image, b-d) transmission electron images including the HRTEM images, c) and d).

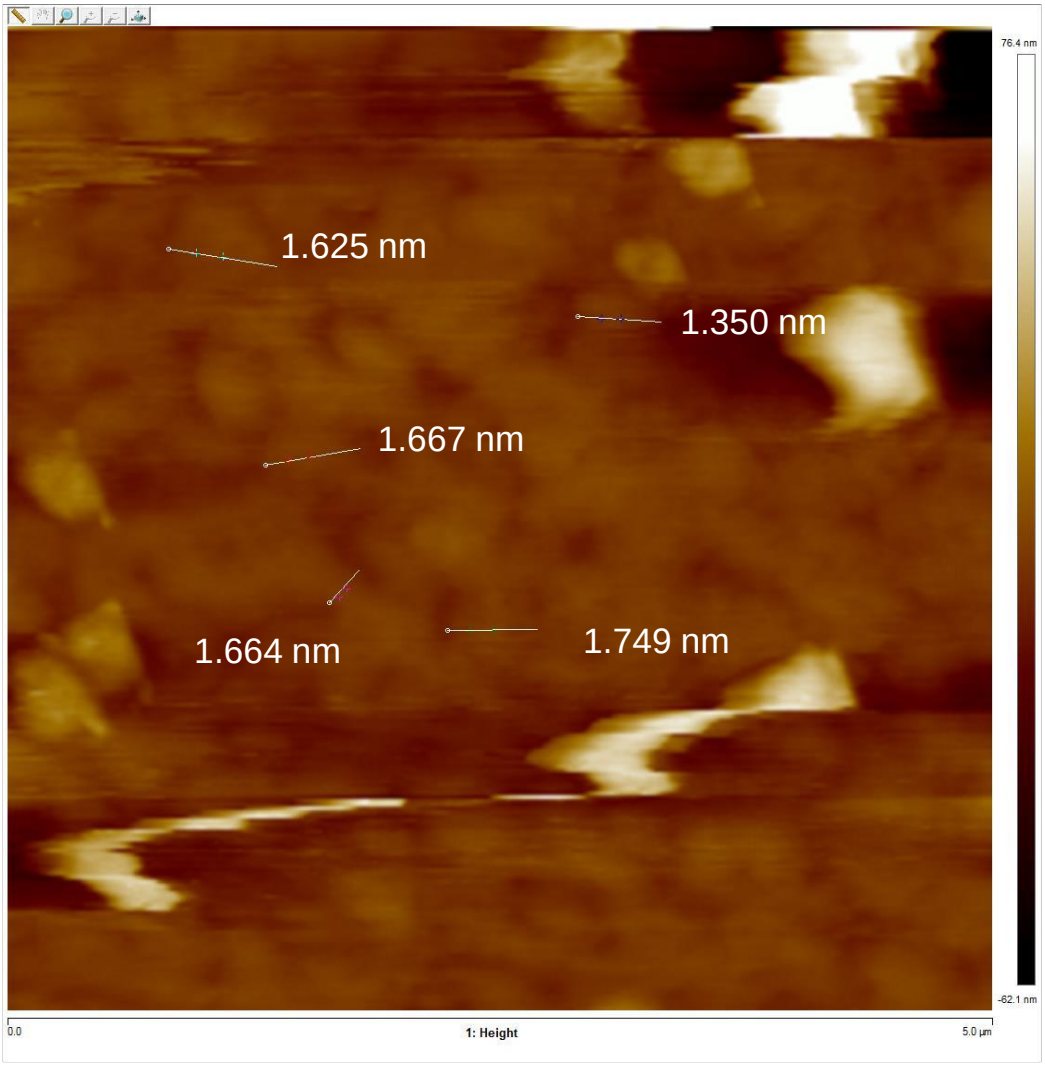

Figure S58. AFM height profile of the **fresh** NiFe-1 after sonication the Fe modified NF in water.

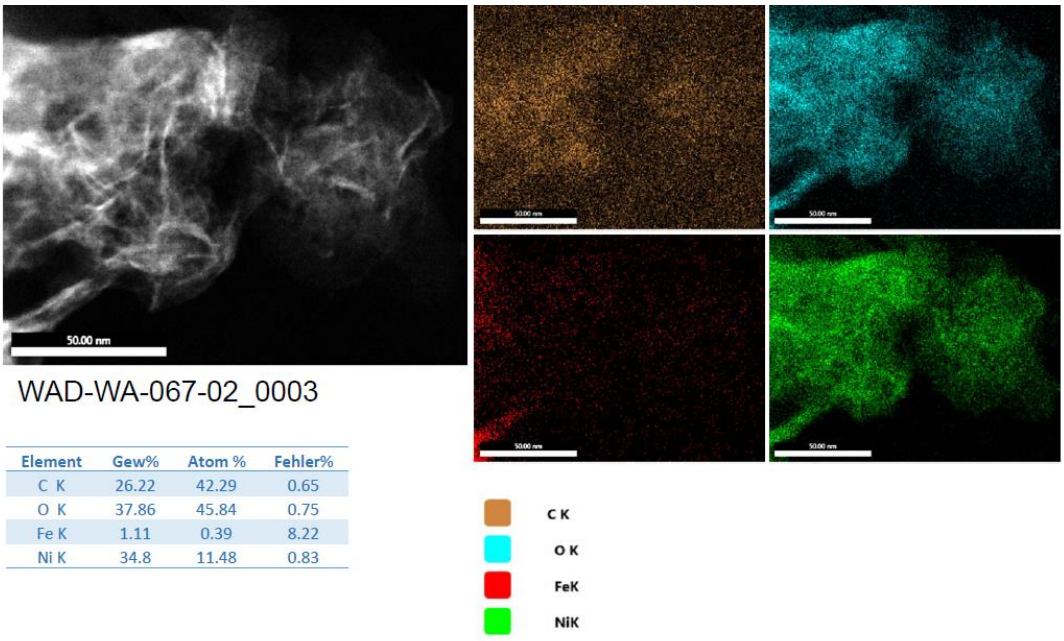

Element	Gew%	Atom %	Fehler%
C K	26.22	42.29	0.65
O K	37.86	45.84	0.75
Fe K	1.11	0.39	8.22
Ni K	34.8	11.48	0.83

Figure S59. HAADF-STEM images of the **fresh** NiFe-1 sample after sonication the Fe modified NF in water, the corresponding elemental mappings, and EDX analyses.

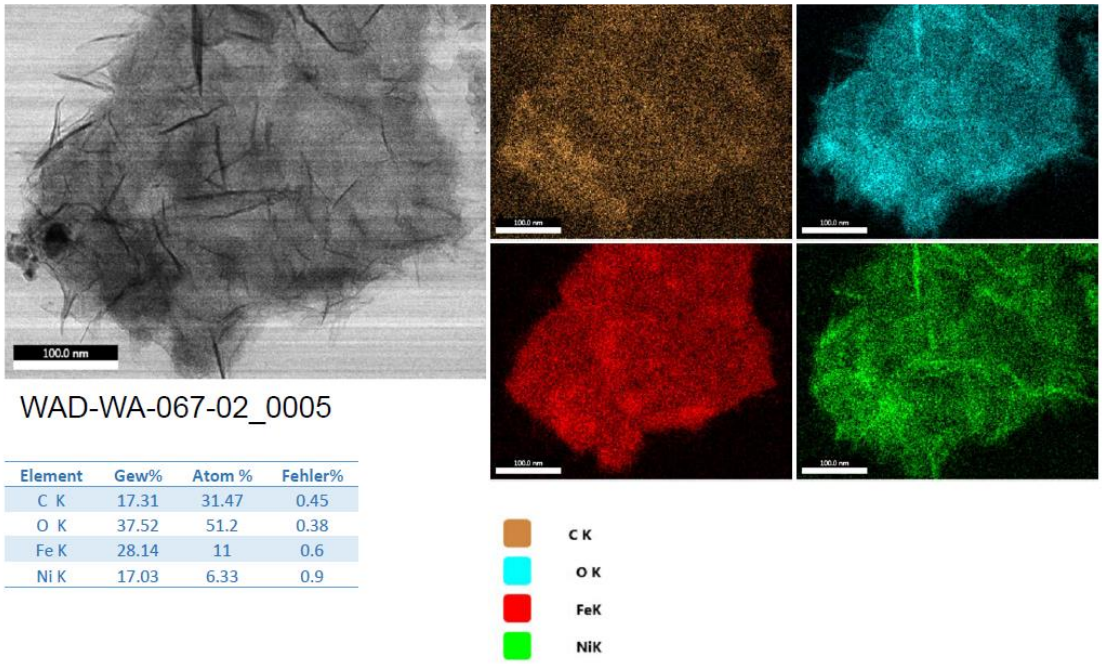

Element	Gew%	Atom %	Fehler%
C K	17.31	31.47	0.45
O K	37.52	51.2	0.38
Fe K	28.14	11	0.6
Ni K	17.03	6.33	0.9

Figure S60. HAADF-STEM images of the **fresh** NiFe-1 after sonication the Fe modified NF in water, the corresponding elemental mappings, and EDX analyses.

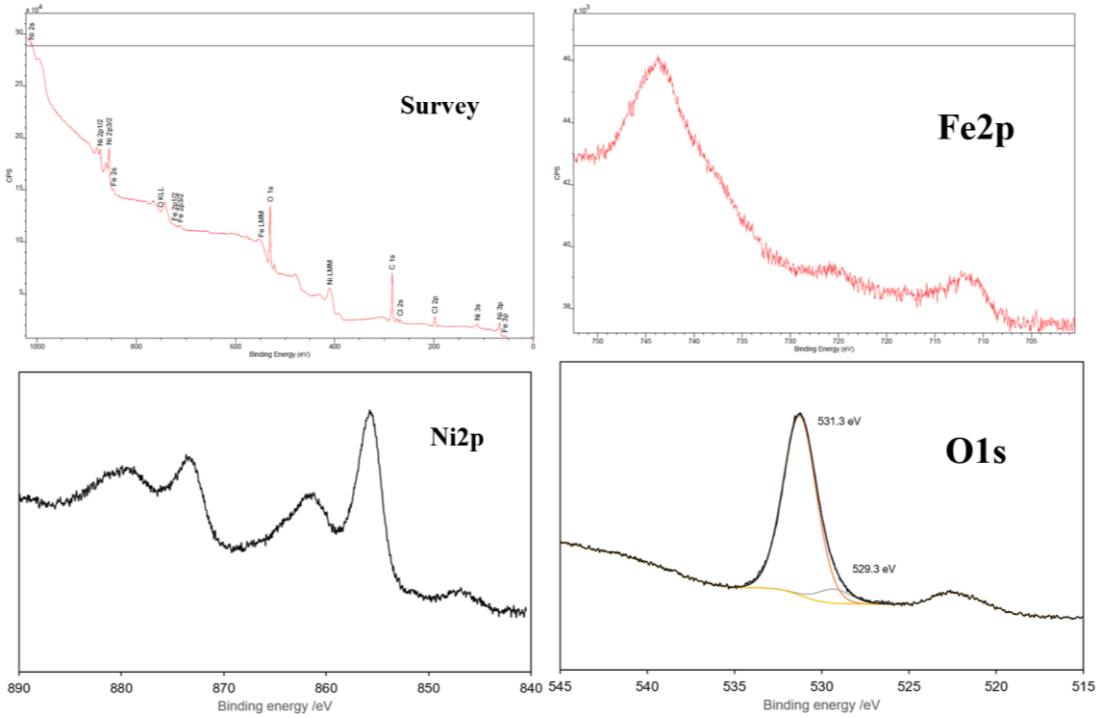

Figure S61. XPS analysis of the **fresh** NiFe-1 electrode, including the survey, Fe 2p, Ni 2p and O 1s spectra.

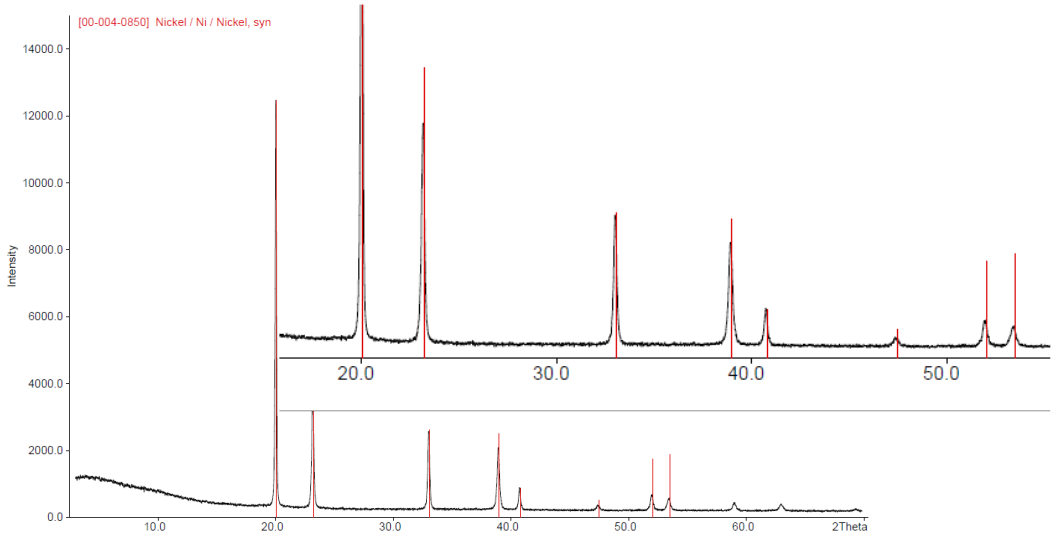

Figure S62. The XRD of fresh NiFe-1 electrode.

It showed the position shift as compared to the pure nickel plate, which led us to conduct the grazing angle experiments, as shown in the main text.

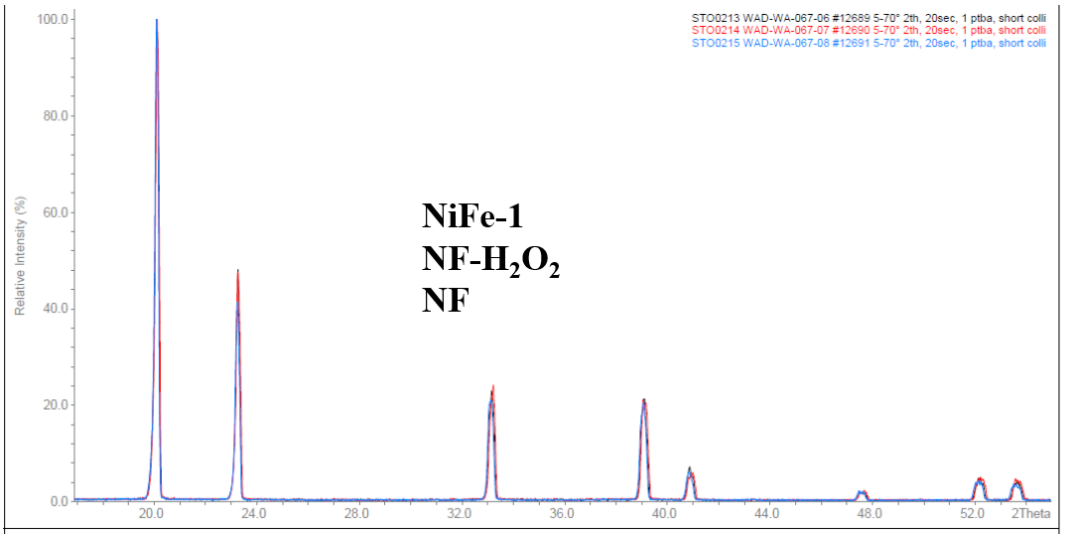

Figure S63. The XRD patterns of fresh NiFe-1 electrode in comparisons with the H_2O_2 treated NF and the purified NF.

Conventional XRD, recorded in grazing incidence to increase the surface contribution to the diffraction patterns, only revealed reflections of nickel (both on a flat sheet and on the foam), with a slight asymmetry/shift, which could indicate some iron incorporation (Figs. S62, S63). However, no indication of any other phase than that of the metal was obtained.

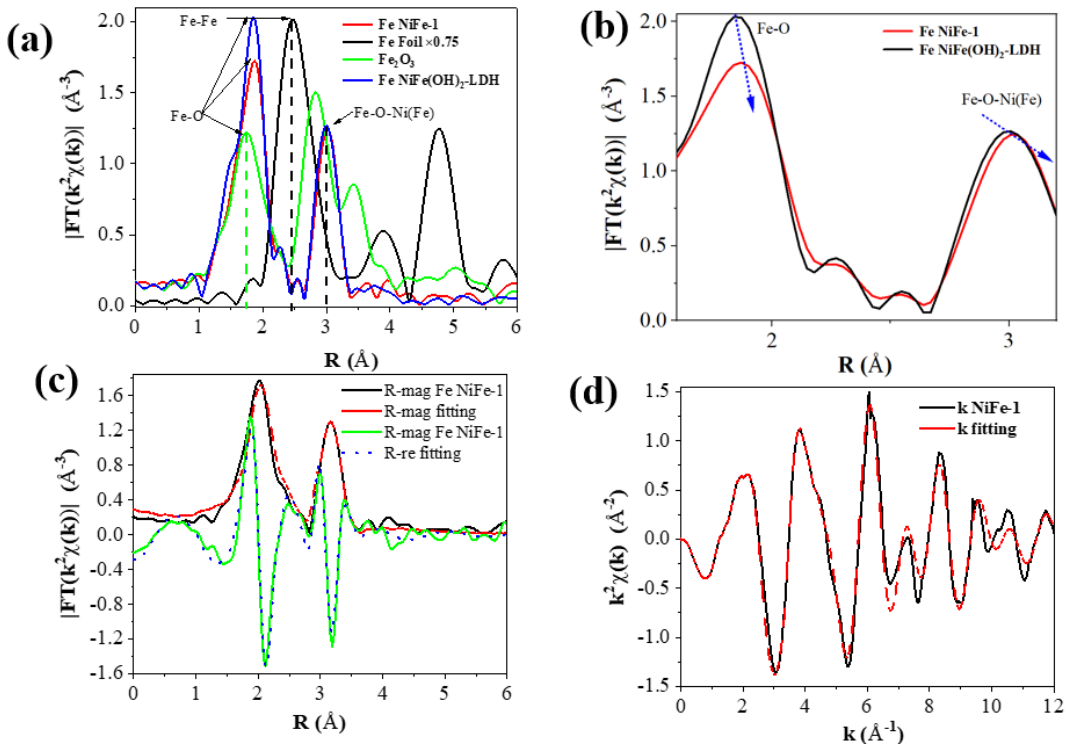

Figure S64. (a) Radial distance χ(R) space spectra (reference samples: Fe foil, Fe_2O_3, and NiFe layered double hydroxide (NiFe-LDH)). (c) χ(R) space spectra fitting curve and (d) $k^2\chi(k)$ space spectra fitting curve of NiFe-1.

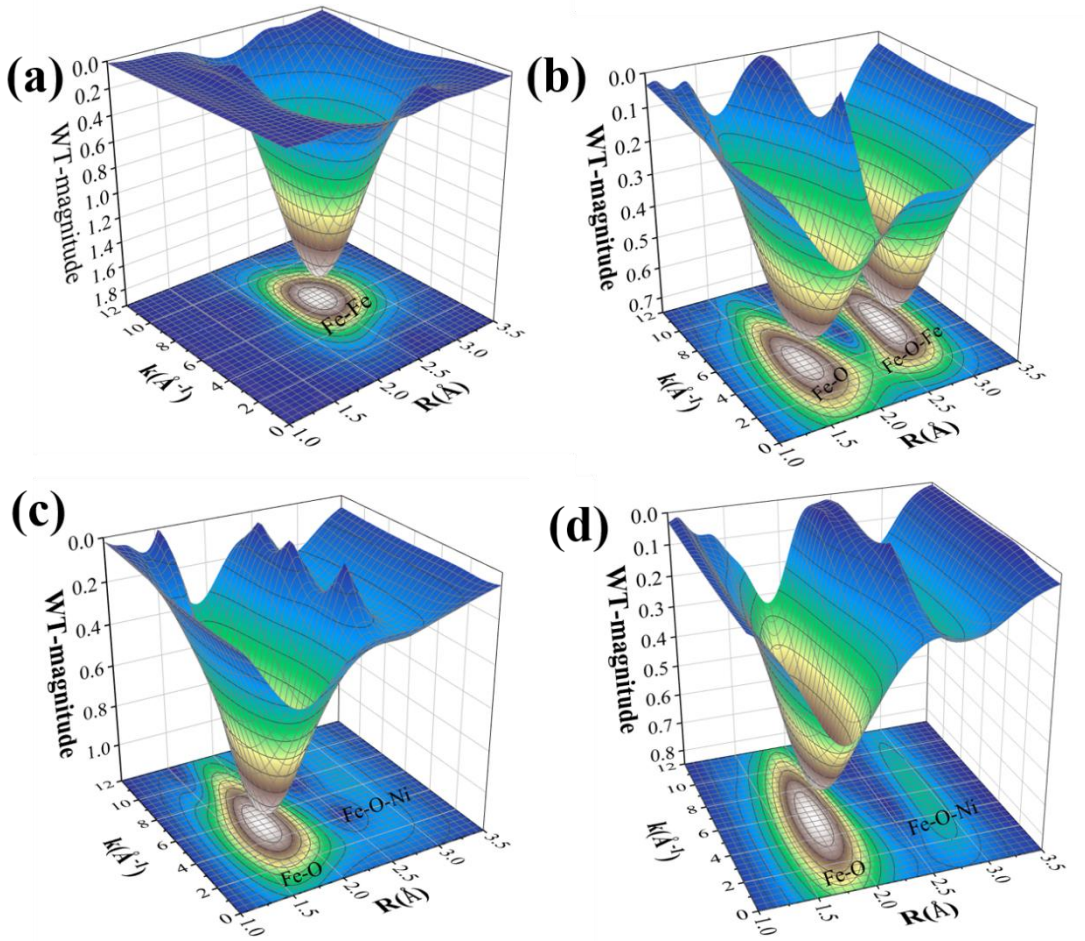

Figure S65. a)-d) 3D contour Wavelet transform extended X-ray absorption fine structure (WT-EXAFS) map with 2D projection of Fe foil, Fe_2O_3, pristine NiFe-LDH, and NiFe-1, respectively.

Table S2. EXAFS fitting results for the local structure parameters around Fe of NiFe-1.

	Reduced Chi-square (χ_v^2)	R-factor（%）	amp/ S_0^2	$N_{(Fe\text{-}O\ path)}$	$R_{(Fe\text{-}O\ path)}$ (Å)	$\sigma^2_{(Fe\text{-}O\ path)}$ (10^{-3}Å^2)	ΔE_0 (eV)
Fe NiFe-1	605.16	0.0427	1.11+/-0.12	4	2.035 ± 0.003	3.8+/-1.7	2.81+/-0.87
			amp/ S_0^2	$N_{(Fe\text{-}O\text{-}Ni\ path)}$	$R_{(Fe\text{-}O\text{-}Ni\ path)}$ (Å)	$\sigma^2_{(Fe\text{-}O\text{-}Ni\ path)}$ (10^{-3}Å^2)	ΔE_0 (eV)
			0.87+/-0.13	6	3.089± 0.005	5.6+/-2.2	1.71+/-0.57

R = distance between absorber and backscattering atoms.
N = coordination number.
σ^2 = Debye-Waller factor.

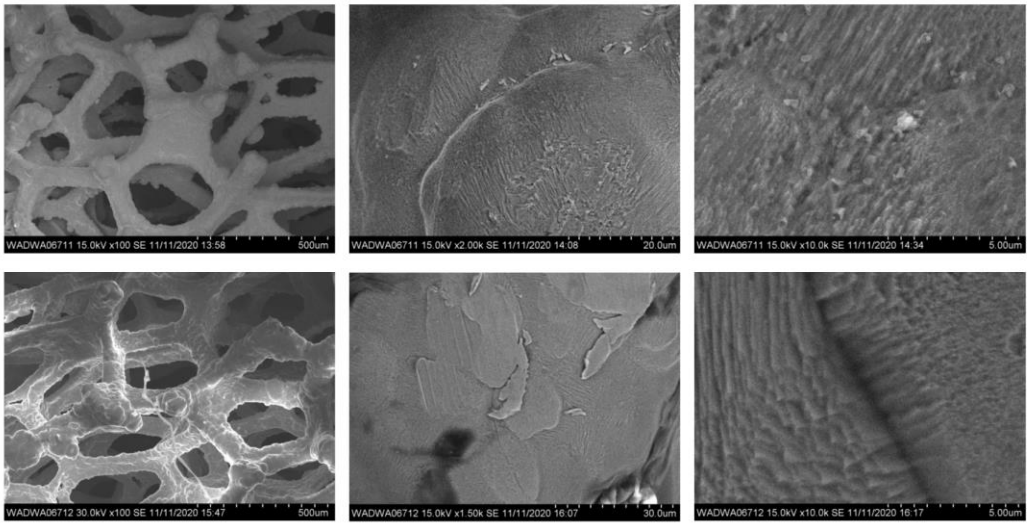

Figure S66. SEM images of the NiFe-1 electrode after the HMF electro-oxidation recycling tests at different magnifications.

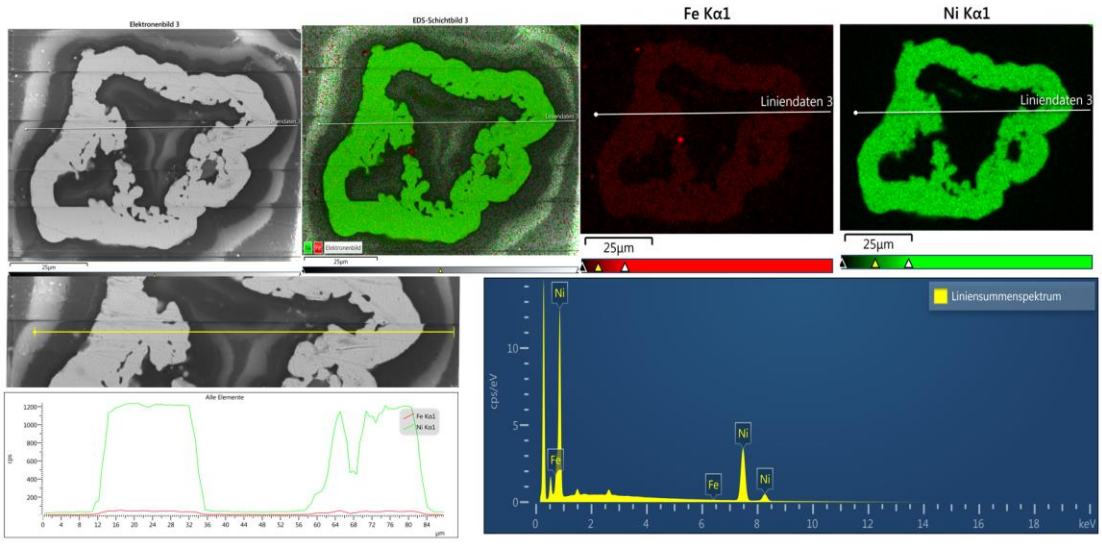

Liniensummenspektrum				
Element	Linientyp	Massen %	Massen % Sigma	Atom %
Fe	K-Serie	0.07	0.07	0.07
Ni	K-Serie	99.93	0.07	99.93
Gesamt		100.00		100.00

Figure S67. SEM analysis of the NiFe-1 electrode after the HMF electro-oxidation recycling tests, including the EDS mappings, line scan analysis and EDX.

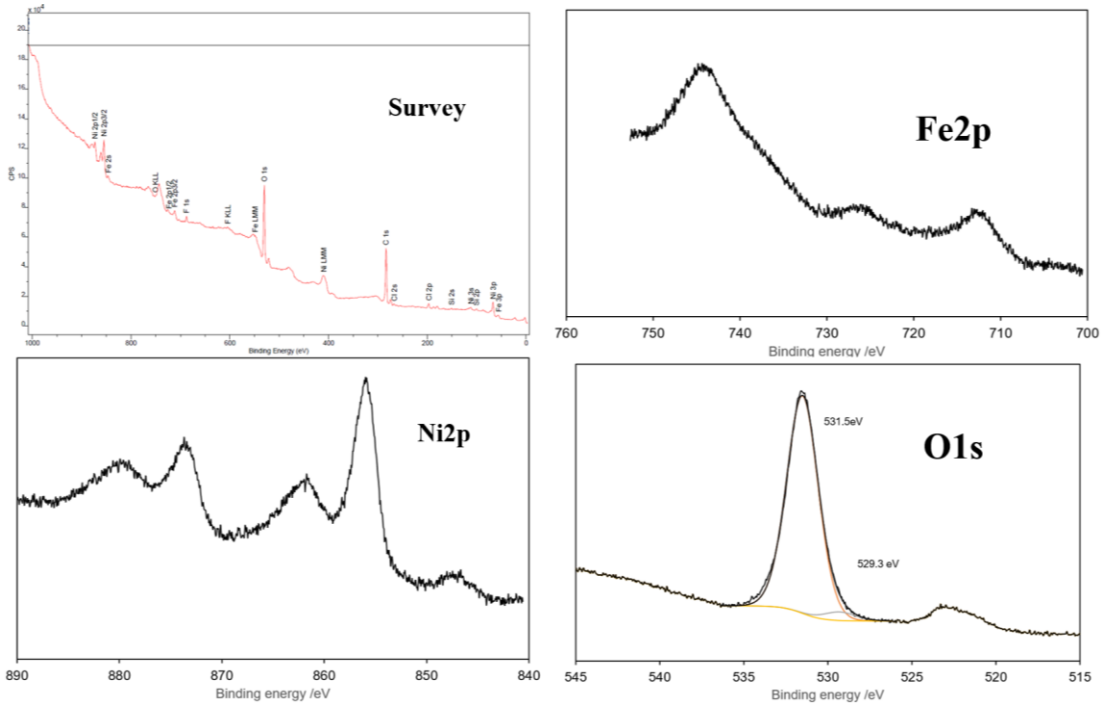

Figure S68. XPS analysis of the NiFe-1 electrode after the HMF electro-oxidation recycling tests, including the survey, Fe 2p, Ni 2p and O 1s spectra.

8. NiFe-1 catalyzed anodic oxidation of organic/inorganic substrates

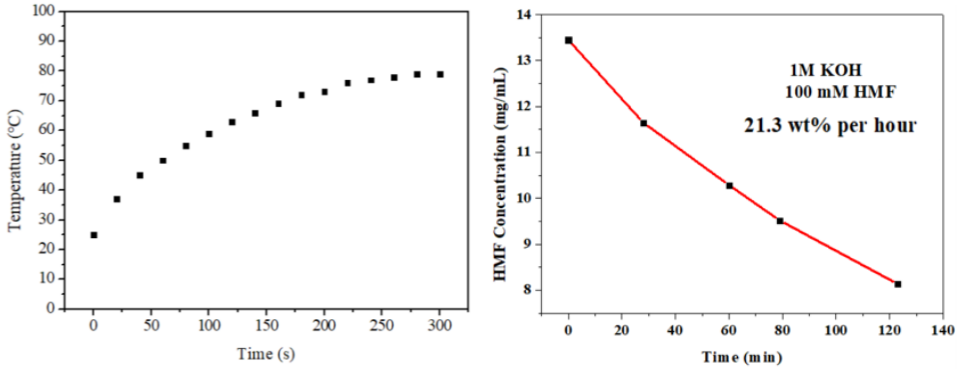

Figure S69. (left) Temperature changes in the cathode chamber measured by an external thermometer during the HMF electro-oxidation. (right) degradation of HMF. Reaction condition: 1 M KOH and 100 mM HMF.

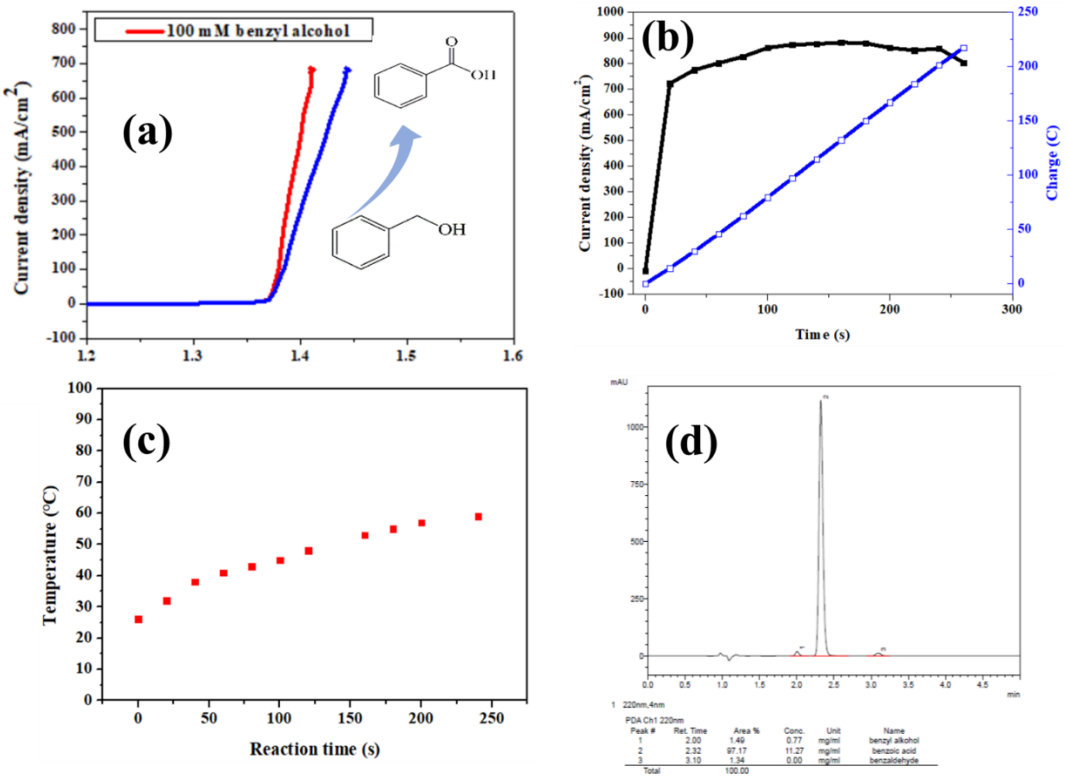

Figure S70. a) LSV curve of NiFe-1 catalyzed benzyl alcohol electro-oxidation in a H-cell (blue line is without compensation, while red line is with 85% iR compensation), b) Current densities, charges *v.s.* time curves, c) Temperature changes *v.s.* time in the cathode chamber measured by an external thermometer, and d) HPLC chromatogram of the final sample. Reaction condition: 1 M KOH and 100 mM benzyl alcohol.

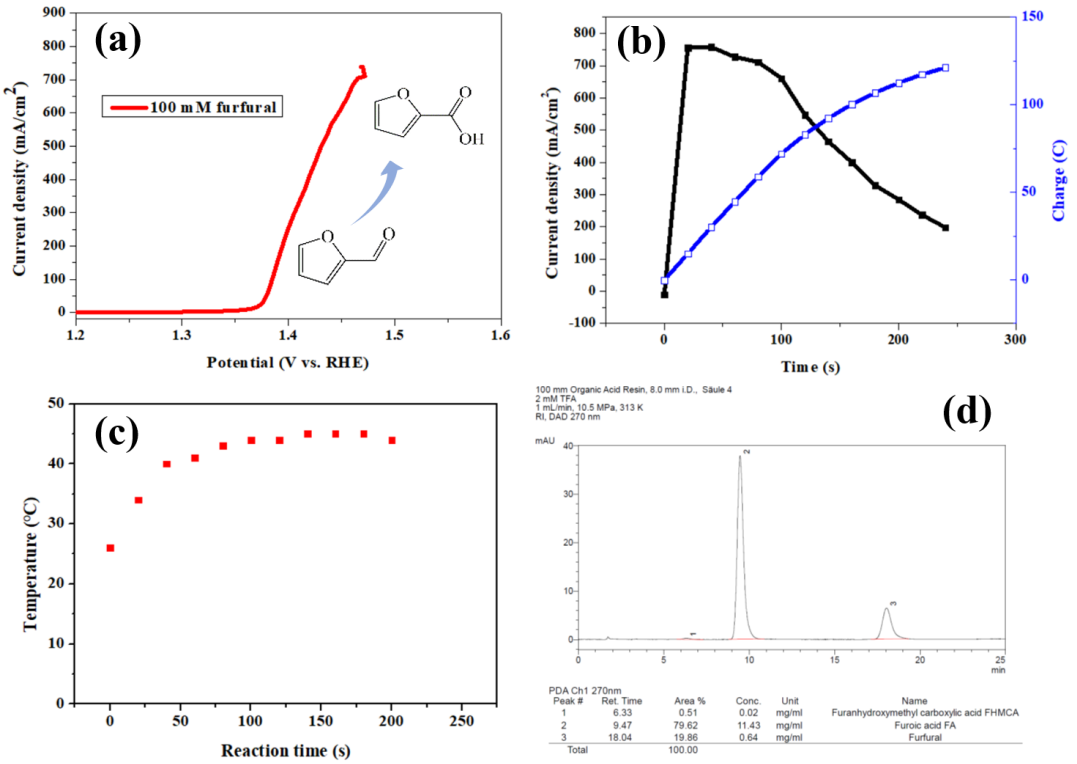

Figure S71. a) LSV curve of NiFe-1 catalyzed furfural electro-oxidation in a H-cell, b) Current densities, charges *v.s.* time curves, c) Temperature changes *v.s.* time in the cathode chamber measured by an external thermometer, and d) HPLC chromatogram of the final sample. Reaction condition: 1 M KOH and 100 mM furfural.

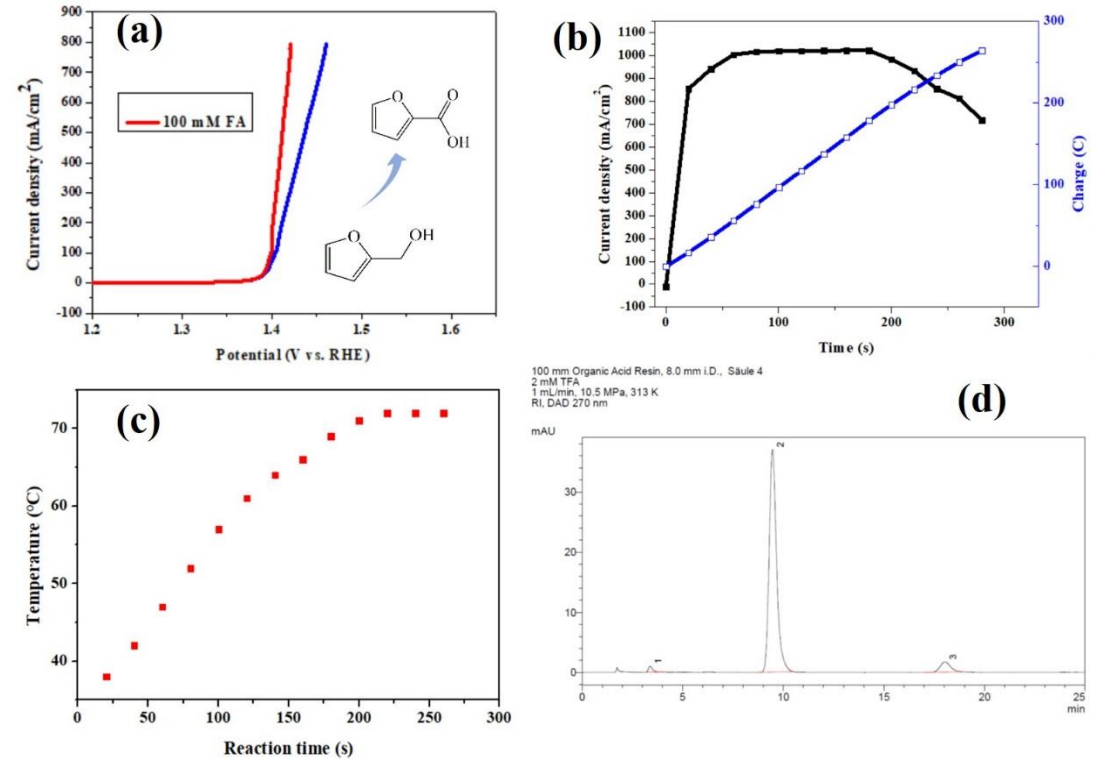

Figure S72. a) LSV curve of NiFe-1 catalyzed furfural alcohol electro-oxidation in a H-cell (blue line is without compensation, while red line is with 85% iR compensation), b) Current densities, charges *v.s.* time curves, c) Temperature changes *v.s.* time in the cathode chamber measured by an external thermometer, and d) HPLC chromatogram of the final sample. Reaction condition: 1 M KOH and 100 mM furfural alcohol.

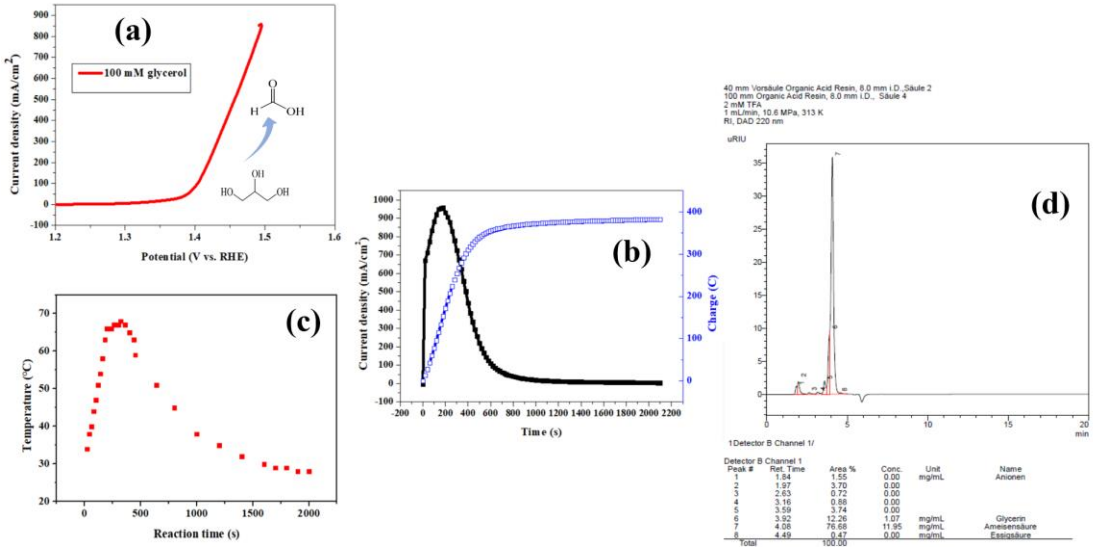

Figure S73. a) LSV curve of NiFe-1 catalyzed glycerol electro-oxidation in a H-cell, b) Current densities, charges *v.s.* time curves, c) Temperature changes *v.s.* time in the cathode chamber measured by an external thermometer, and d) HPLC chromatogram of the final sample. Reaction condition: 1 M KOH and 100 mM glycerol.

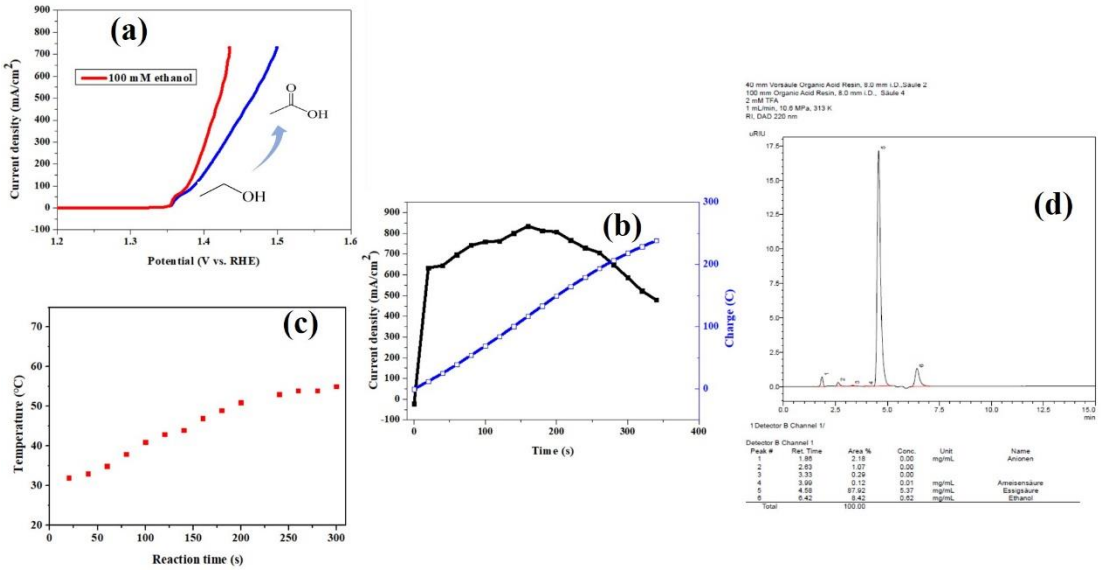

Figure S74. a) LSV curve of NiFe-1 catalyzed ethanol electro-oxidation in a H-cell (blue line is without compensation, while red line is with 85% iR compensation), b) Current densities, charges *v.s.* time curves, c) Temperature changes *v.s.* time in the cathode chamber measured by an external thermometer, and d) HPLC chromatogram of the final sample. Reaction condition: 1 M KOH and 100 mM ethanol.

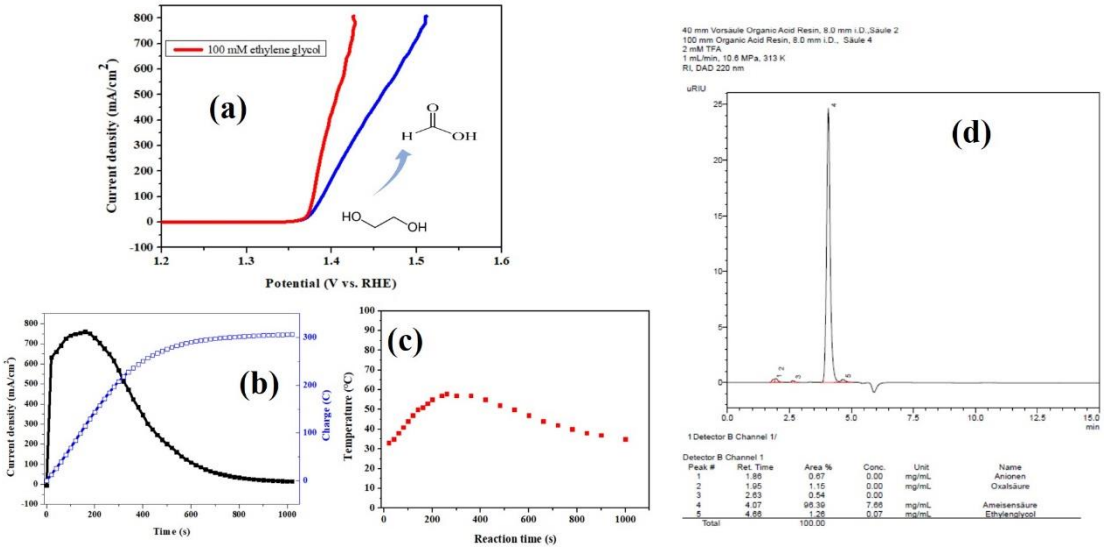

Figure S75. a) LSV curve of NiFe-1 catalyzed ethylene glycol electro-oxidation in a H-cell (blue line is without compensation, while red line is with 85% iR compensation), b) Current densities, charges *v.s.* time curves, c) Temperature changes *v.s.* time in the cathode chamber measured by an external thermometer, and d) HPLC chromatogram of the final sample. Reaction condition: 1 M KOH and 100 mM ethylene glycol.

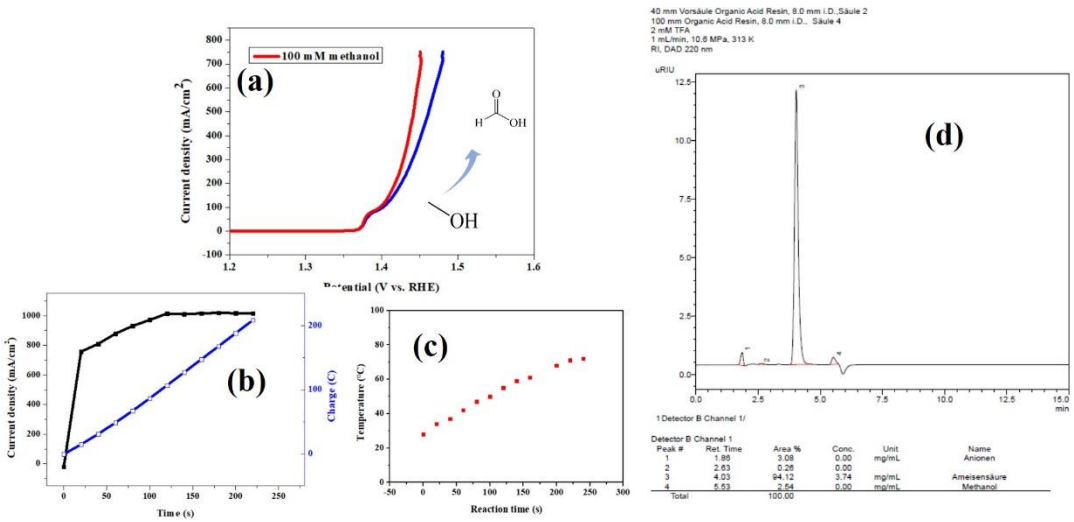

Figure S76. a) LSV curve of NiFe-1 catalyzed methanol electro-oxidation in a H-cell (blue line is without compensation, while red line is with 85% iR compensation), b) Current densities, charges *v.s.* time curves, c) Temperature changes *v.s.* time in the cathode chamber measured by an external thermometer, and d) HPLC chromatogram of the final sample. Reaction condition: 1 M KOH and 100 mM methanol.

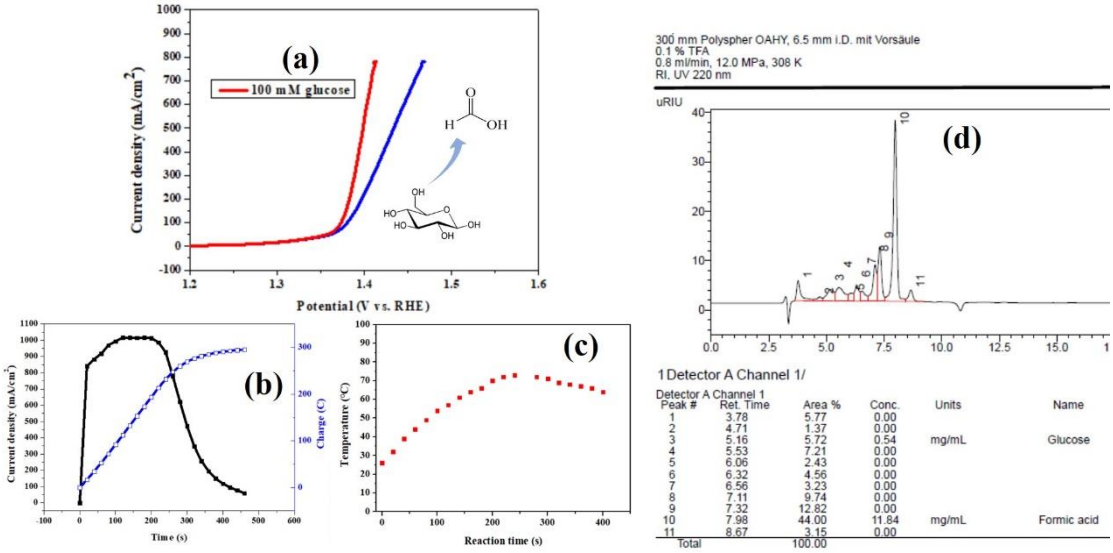

Figure S77. a) LSV curve of NiFe-1 catalyzed glucose electro-oxidation in a H-cell (blue line is without compensation, while red line is with 85% iR compensation), b) Current densities, charges *v.s.* time curves, c) Temperature changes *v.s.* time in the cathode chamber measured by an external thermometer, and d) HPLC chromatogram of the final sample. Reaction condition: 1 M KOH and 100 mM glucose.

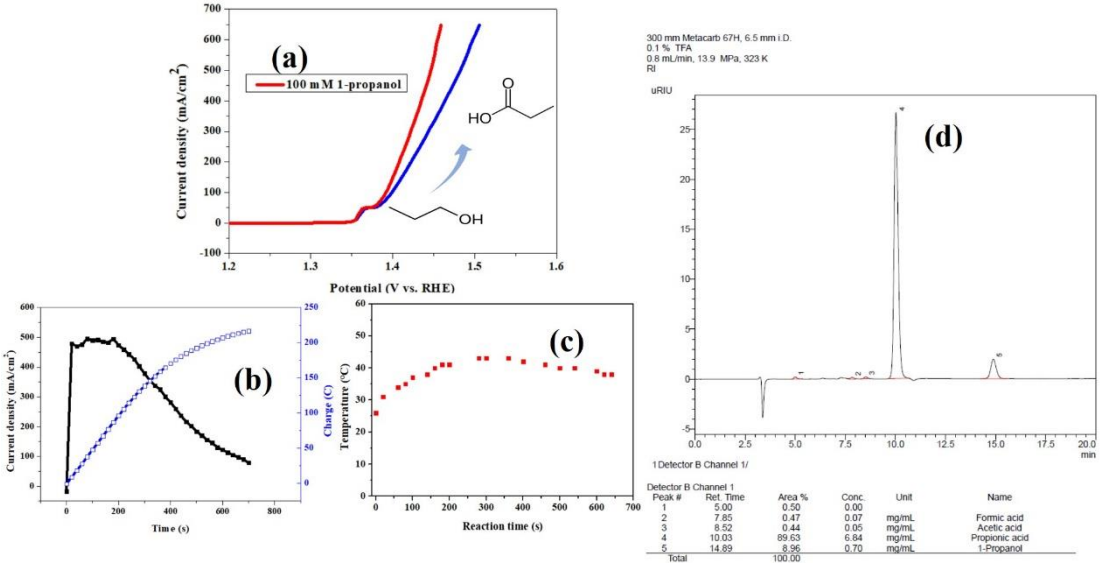

Figure S78. a) LSV curve of NiFe-1 catalyzed 1-propanol electro-oxidation in a H-cell (blue line is without compensation, while red line is with 85% iR compensation), b) Current densities, charges *v.s.* time curves, c) Temperature changes *v.s.* time in the cathode chamber measured by an external thermometer, and d) HPLC chromatogram of the final sample. Reaction condition: 1 M KOH and 100 mM 1-propanol.

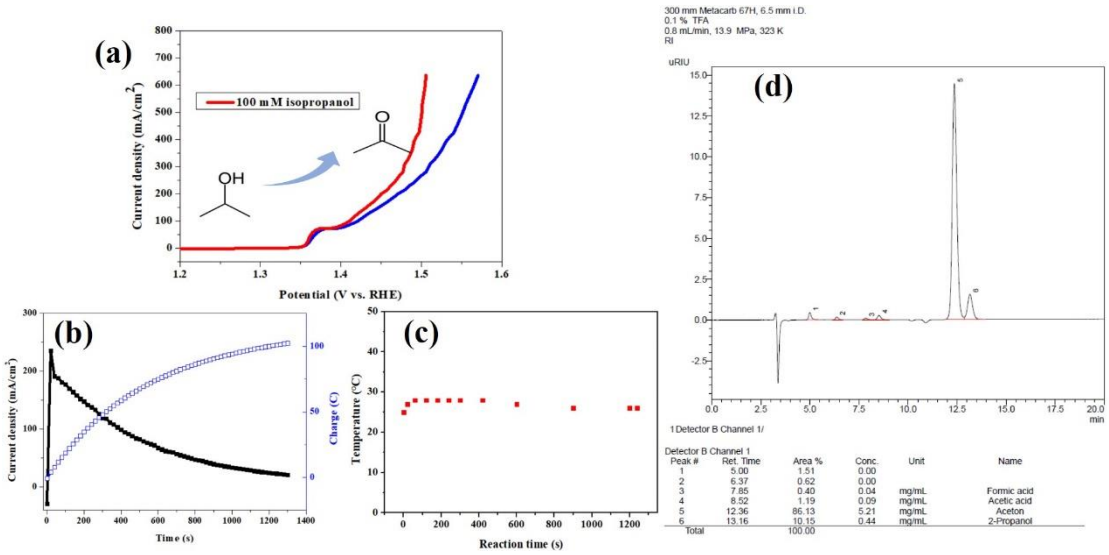

Figure S79. a) LSV curve of NiFe-1 catalyzed 2-propanol electro-oxidation in a H-cell (blue line is without compensation, while red line is with 85% iR compensation), b) Current densities, charges *v.s.* time curves, c) Temperature changes *v.s.* time in the cathode chamber measured by an external thermometer, and d) HPLC chromatogram of the final sample. Reaction condition: 1 M KOH and 100 mM 2-propanol.

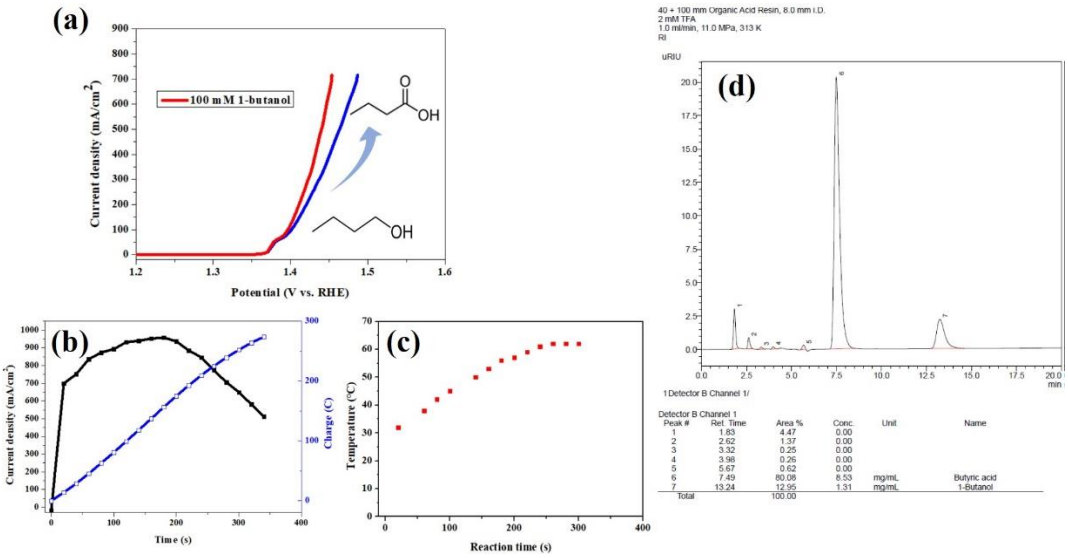

Figure S80. a) LSV curve of NiFe-1 catalyzed 1-butanol electro-oxidation in a H-cell (blue line is without compensation, while red line is with 85% iR compensation), b) Current densities, charges *v.s.* time curves, c) Temperature changes *v.s.* time in the cathode chamber measured by an external thermometer, and d) HPLC chromatogram of the final sample. Reaction condition: 1 M KOH and 100 mM 1-butanol.

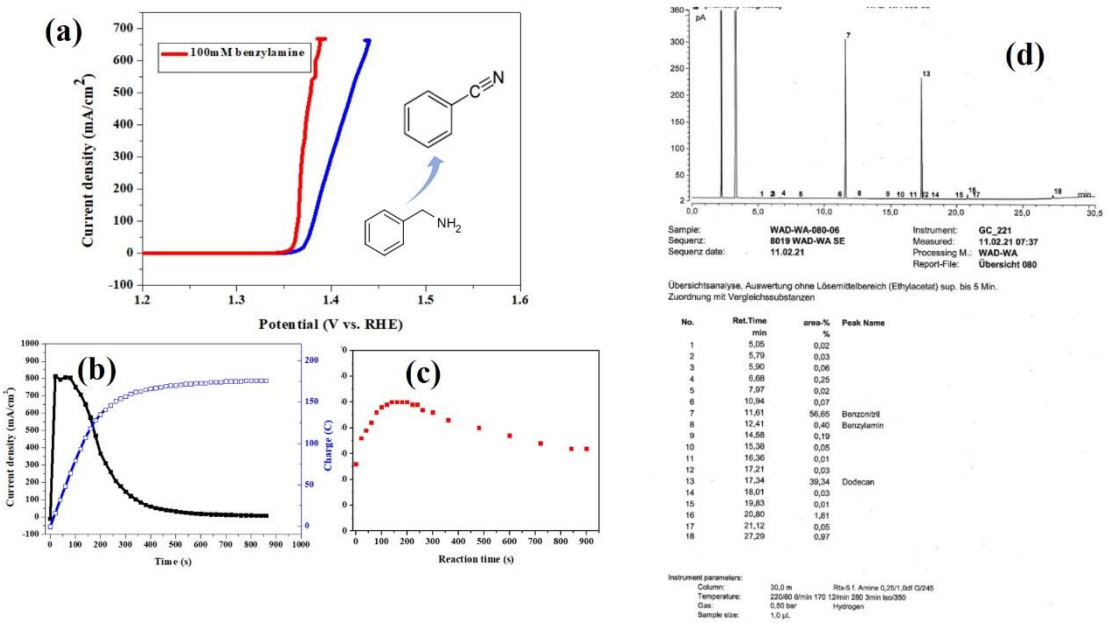

Figure S81. a) LSV curve of NiFe-1 catalyzed benzyl amine electro-oxidation in a H-cell (blue line is without compensation, while red line is with 85% iR compensation), b) Current densities, charges *v.s.* time curves, c) Temperature changes *v.s.* time in the cathode chamber measured by an external thermometer, and d) GC chromatogram of the final sample (electrolyte solution was extracted with ethyl acetate, and using dodecane as internal standard). Reaction condition: 1 M KOH and 100 mM benzyl amine.

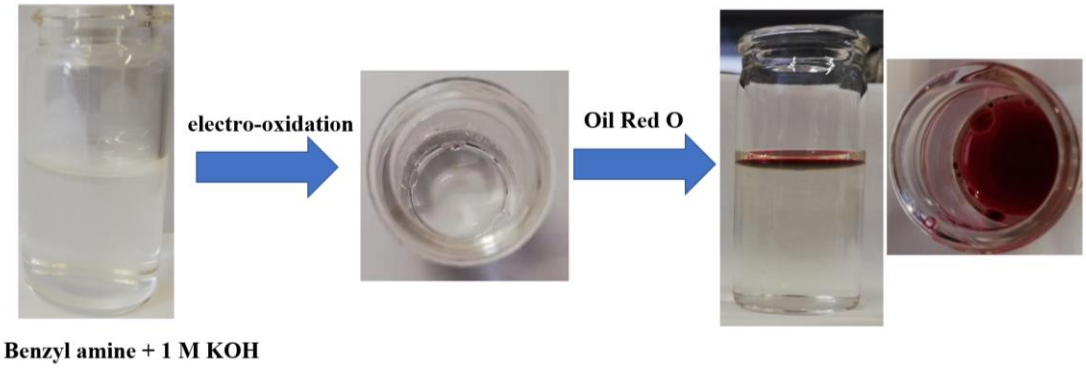

Figure S82. Digital figures of NiFe-1 catalyzed benzyl amine electro-oxidation and the color change upon the addition of Oil Red O.

Typically, most of the amines have good water solubility. However, benzyl amine in 1M KOH aqueous solution cannot be completely dissolved. Electrooxidation of this substrate was explored nevertheless, due to the low oxidation potential compared to OER. Also the benzyl amine is efficiently converted into the corresponding nitrile at high current density within a very short time. The benzonitrile is oily, floats on the surface of the electrolyte, and changes into pink-red color upon the addition of Oil Red O (an oil-soluble dye). Those observations demonstrate that electrochemical oxidative upgrading of amines to corresponding nitriles can be highly favorable, and the products can be efficiently isolated by solvent extraction (here ethyl acetate was used), or water-oil separation membrane, showing the high promise in large-scale industrial productions of nitrile products.

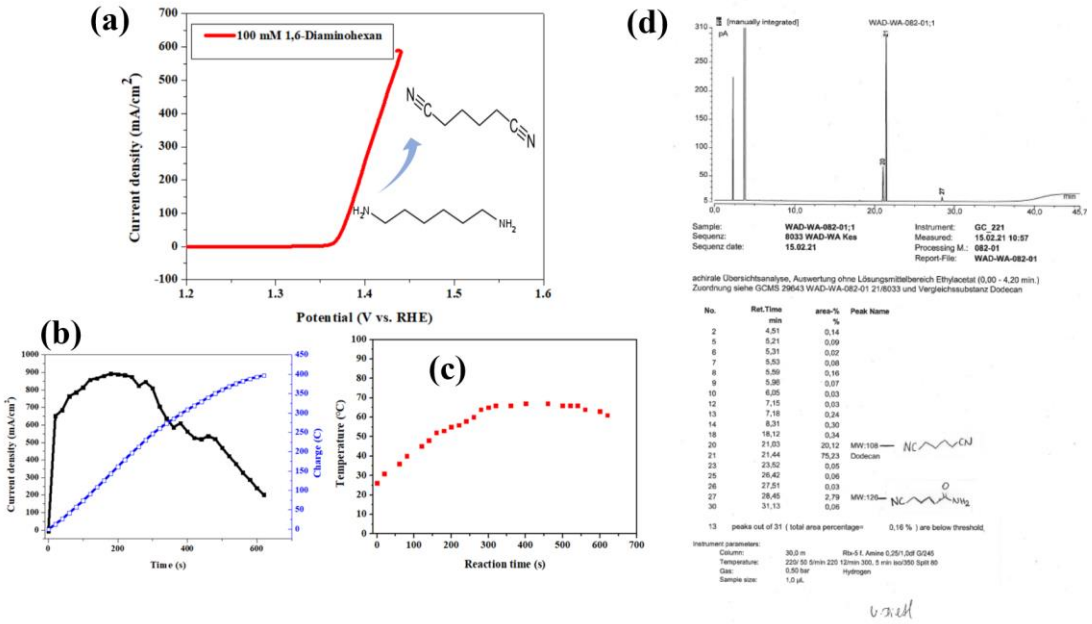

Figure S83. a) LSV curve of NiFe-1 catalyzed 1,6-Diaminohexan electro-oxidation in a H-cell, b) Current densities, charges *v.s.* time curves, c) Temperature changes *v.s.* time in the cathode chamber measured by an external thermometer, and d) GC chromatogram of the final sample (electrolyte solution was extracted with ethyl acetate, and using dodecane as internal standard). Reaction condition: 1 M KOH and 100 mM 1,6-Diaminohexan.

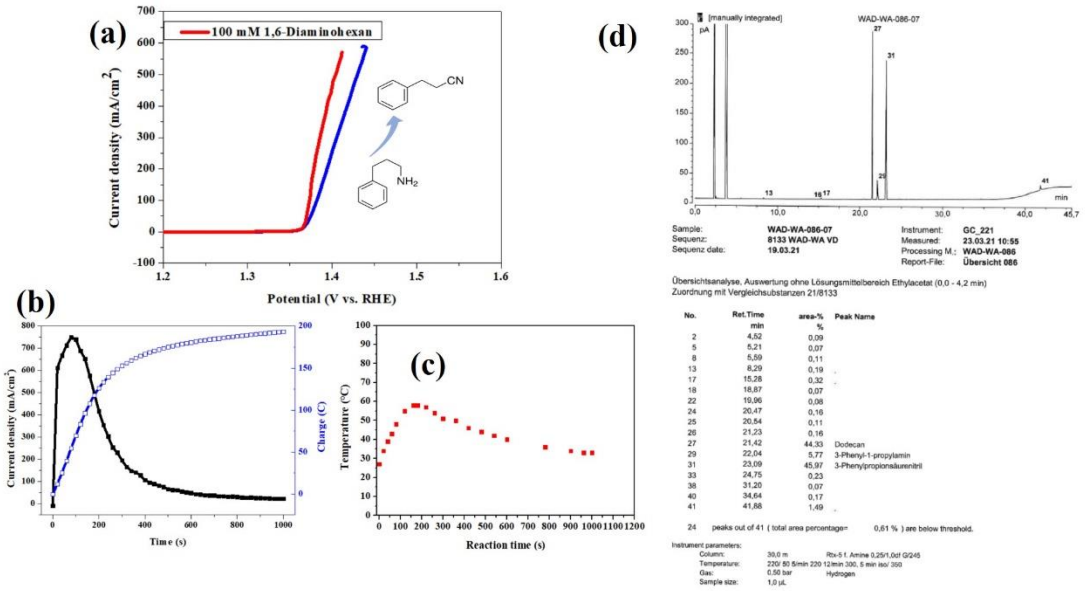

Figure S84. a) LSV curve of NiFe-1 catalyzed 3-phenylpropan-1-amine electro-oxidation in a H-cell (blue line is without compensation, while red line is with 85% iR compensation), b) Current densities, charges *v.s.* time curves, c) Temperature changes *v.s.* time in the cathode chamber measured by an external thermometer, and d) GC chromatogram of the final sample (electrolyte solution was extracted with ethyl acetate, and using dodecane as internal standard). Reaction condition: 1 M KOH and 100 mM 3-phenylpropan-1-amine.

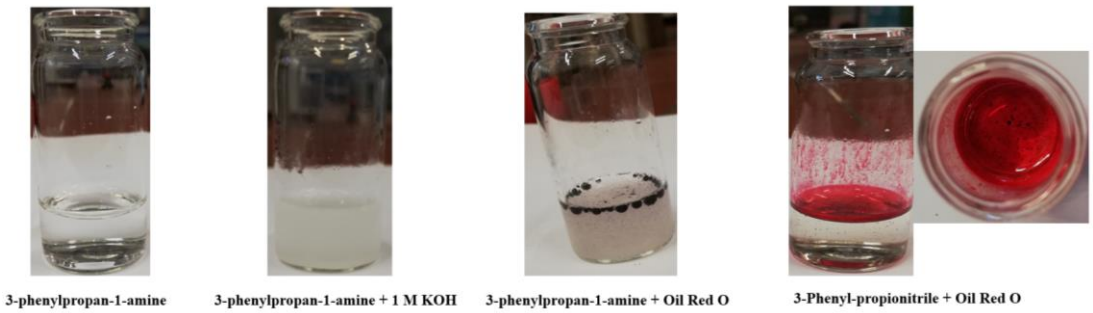

Figure S85. Digital figures of NiFe-1 catalyzed 3-phenylpropan-1-amine electro-oxidation and the color change upon the addition of Oil Red O.

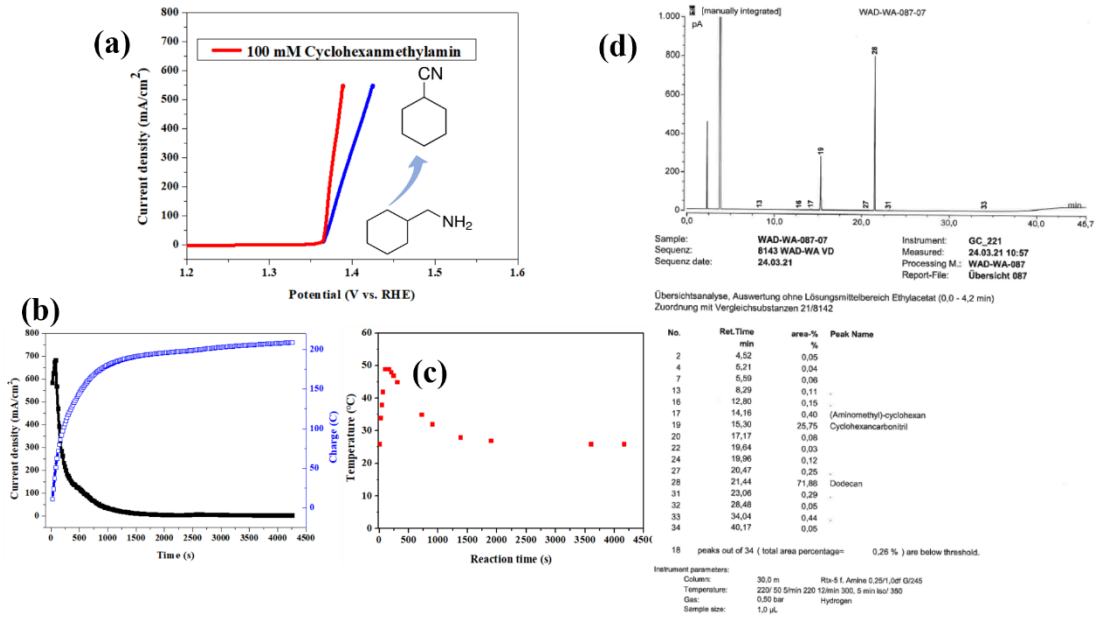

Figure S86. a) LSV curve of NiFe-1 catalyzed cyclohexanemethylamine electro-oxidation in a H-cell (blue line is without compensation, while red line is with 85% iR compensation), b) Current densities, charges *v.s.* time curves, c) Temperature changes *v.s.* time in the cathode chamber measured by an external thermometer, and d) GC chromatogram of the final sample (electrolyte solution was extracted with ethyl acetate, and using dodecane as internal standard). Reaction condition: 1 M KOH and 100 mM cyclohexanemethylamine.

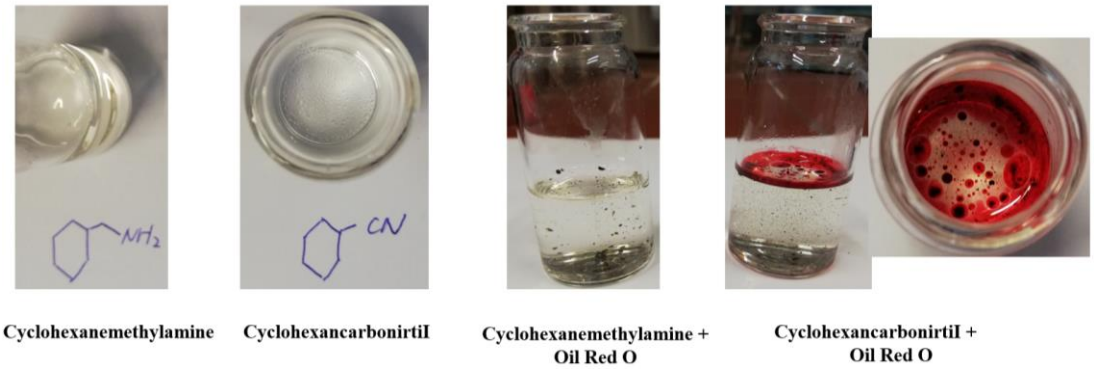

Figure S87. Digital figures of NiFe-1 catalyzed cyclohexanemethylamine electro-oxidation and the color change upon the addition of Oil Red O.

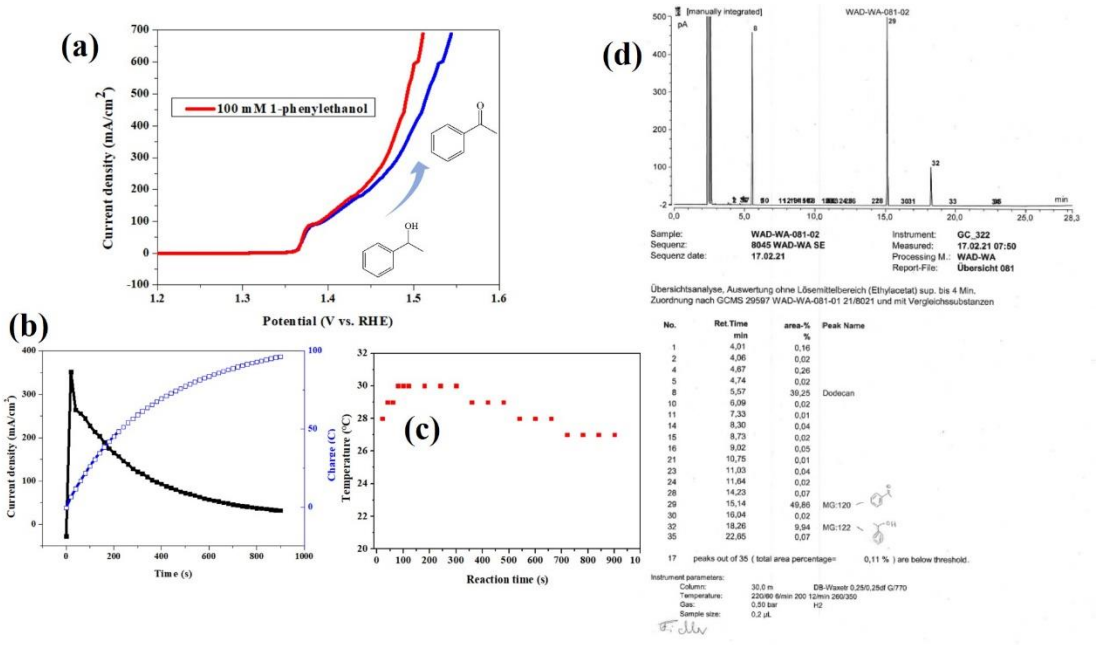

Figure S88. a) LSV curve of NiFe-1 catalyzed 1-phenylethanol electro-oxidation in a H-cell (blue line is without compensation, while red line is with 85% iR compensation), b) Current densities, charges *v.s.* time curves, c) Temperature changes *v.s.* time in the cathode chamber measured by an external thermometer, and d) GC chromatogram of the final sample (electrolyte solution was extracted with ethyl acetate, and using dodecane as internal standard). Reaction condition: 1 M KOH and 100 mM 1-phenylethanol.

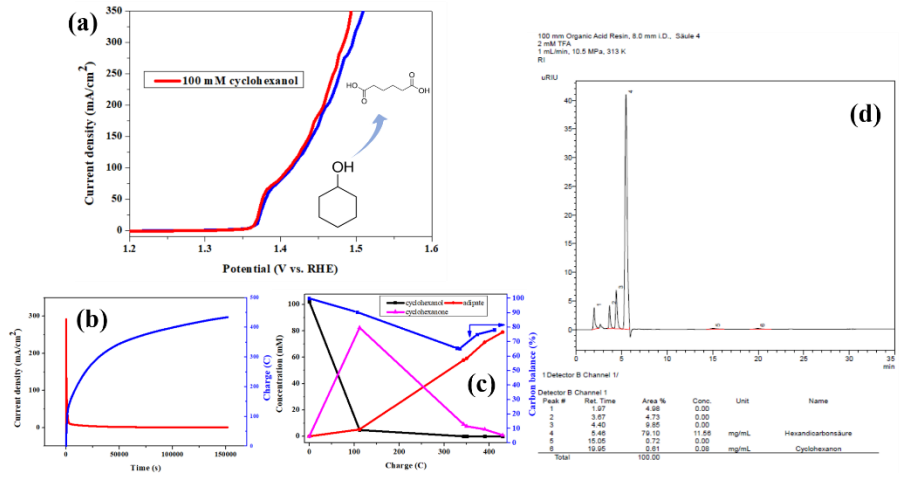

Figure S89. a) LSV curve of NiFe-1 catalyzed cyclohexanol electro-oxidation in a H-cell (blue line is without compensation, while red line is with 85% iR compensation), b) Current densities, charges *v.s.* time curves, c) conversion and concentration changes of cyclohexanol and its oxidation products during the electrochemical oxidation of cyclohexanol, and d) HPLC chromatogram of the final sample. Reaction condition: 1 M KOH and 100 mM cyclohexanol.

KA oil (a mixture of cyclohexanol and cyclohexanone), which can be produced from lignin-derived phenols or aromatic ethers via reductive routes, are used as high-volume industrial feed- stock for the manufacture of adipic acid and as essential industrial precursors in the pesticide, pharmaceutical, and food industries. KA oil contains C(OH)-C and C(O)-C bonds, and can be upgraded to adipic acid by electrochemical oxidative transformations over NiFe-1. HPLC results showed that cyclohexanol was progressively converted to adipate via cyclohexanone as the intermediate with the 100% conversion of cyclohexanol, 77.4% yield of adipic acid and negligible traces of cyclohexanone after passing a charge of 430 C. This reaction involves the first electro-oxidation of cyclohexanol to cyclohexanone, which accumulates to the maximum concentration and thereafter is converted to adipic acid by electrochemical oxidative cleavage of either C(OH)-C or C(O)-C bonds.

In industry, the manufacture of adipic acid relies almost exclusively on the oxidation of cyclohexanol or the KA oil with nitric acid as the oxidant in the presence of copper and vanadium catalysts, producing greenhouse gas nitrous oxides, which raises the cost, requires additional safety precautions, and is associated with environmental problems. Under the conditions explored here, electrochemical transformations of lignin-derived cyclohexanol to adipic acid is conducted under mild and environmentally benign conditions. Thus, the strategy —electrochemical oxidative cleavage C(OH)-C and C(O)-C bonds over NiFe-1 electrode—offers a sustainable pathway for the large-scale, highly efficient and selective production of adipic acid, an industrial important intermediate to produce nylon 6,6 (polyester, plastic, etc.), which is also widely used in the food industry and in cosmetics, from renewable biomass substrates.

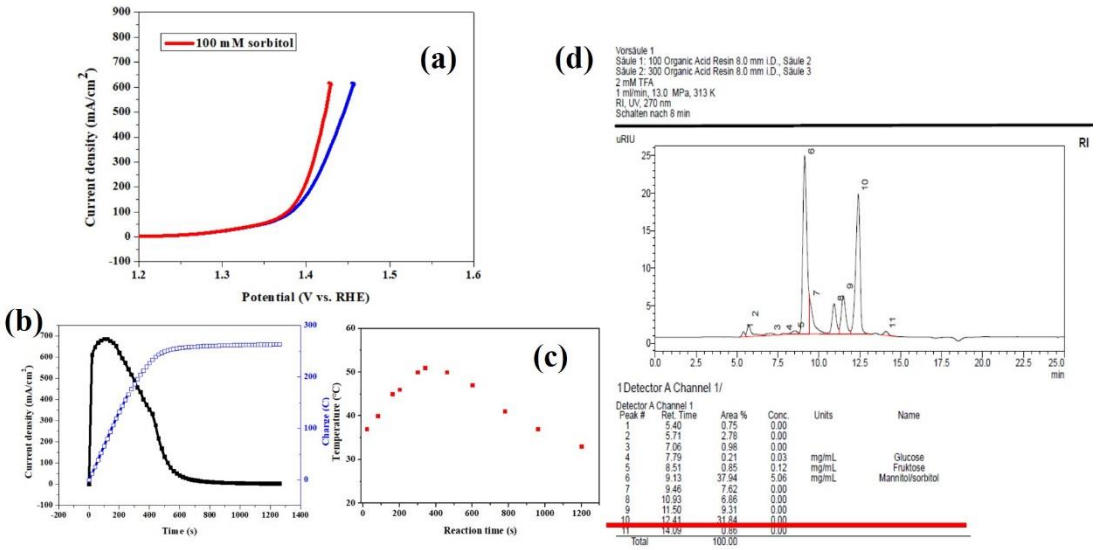

Figure S90. a) LSV curve of NiFe-1 catalyzed sorbitol electro-oxidation in a H-cell (blue line is without compensation, while red line is with 85% iR compensation), b) Current densities, charges *v.s.* time curves, c) Temperature changes *v.s.* time in the cathode chamber measured by an external thermometer, and d) HPLC chromatogram of the final sample. Reaction condition: 1 M KOH and 100 mM sorbitol.

High current density and potential shift was observed upon the addition of the sorbitol, compared to those of the OER. In addition, the solution color changed from colorless to light yellow and finally to dark yellow. However, the HPLC of the final sample (taken at the 263.5 C) showed a high amount of an unknown product at retention time of 12.41 min. This peak with other glucose and fructose products may suggest the production of either oxidation products or C-C cleavage products, which could not be identified at this point.

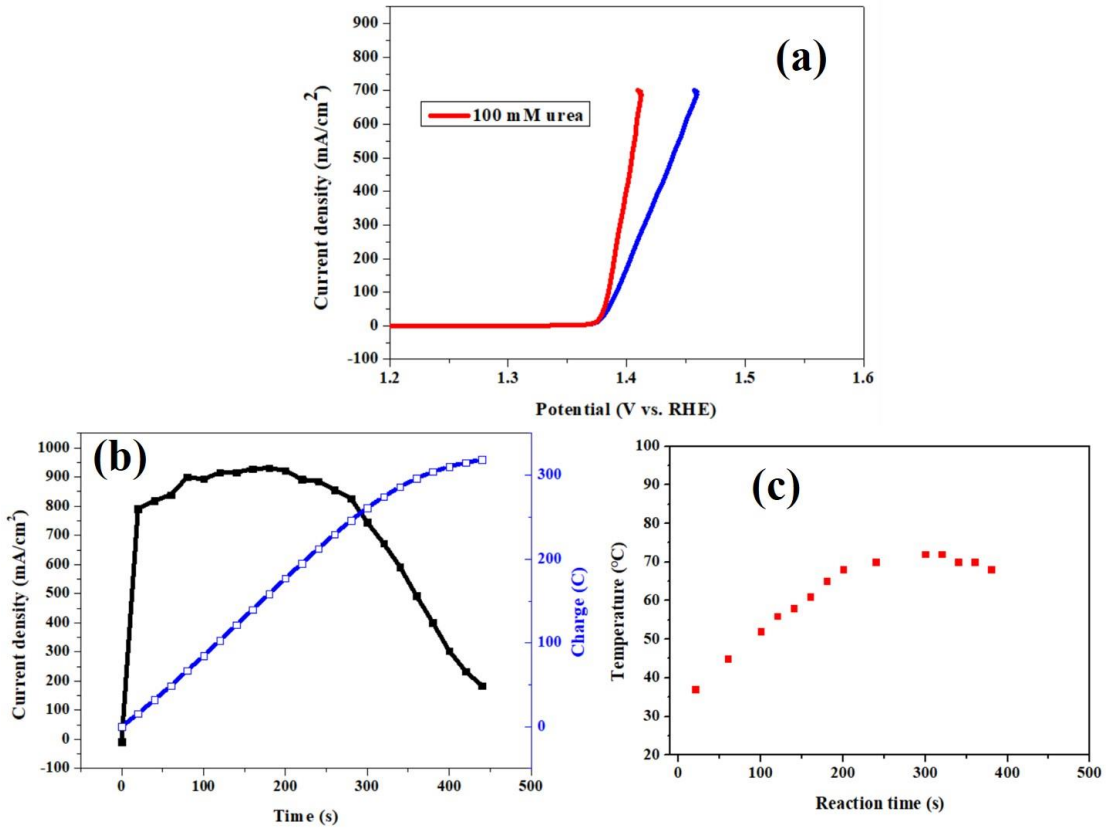

Figure S91. a) LSV curve of NiFe-1 catalyzed urea electro-oxidation in a H-cell (blue line is without compensation, while red line is with 85% iR compensation), b) Current densities, charges *v.s.* time curves, c) Temperature changes *v.s.* time in the cathode chamber measured by an external thermometer. Reaction condition: 1 M KOH and 100 mM urea.

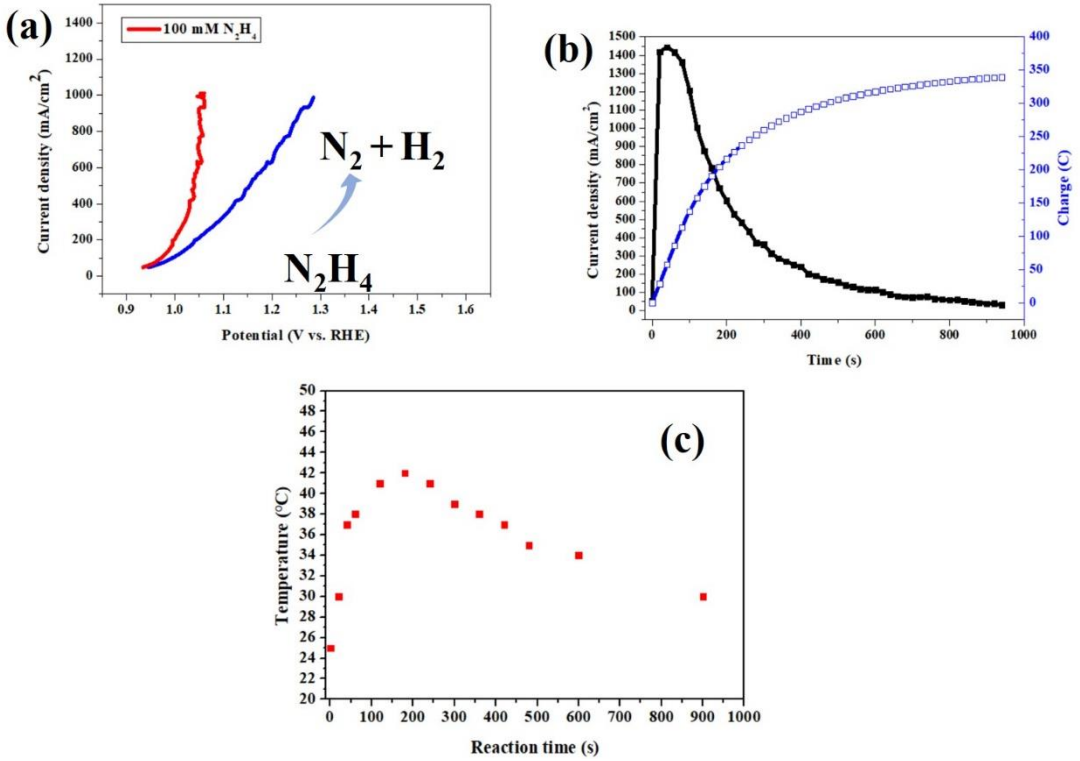

Figure S92. a) LSV curve of NiFe-1 catalyzed N_2H_4 electro-oxidation in a H-cell (blue line is without compensation, while red line is with 85% iR compensation), b) Current densities, charges *v.s.* time curves, c) Temperature changes *v.s.* time in the cathode chamber measured by an external thermometer. Reaction condition: 1 M KOH and 100 mM N_2H_4.

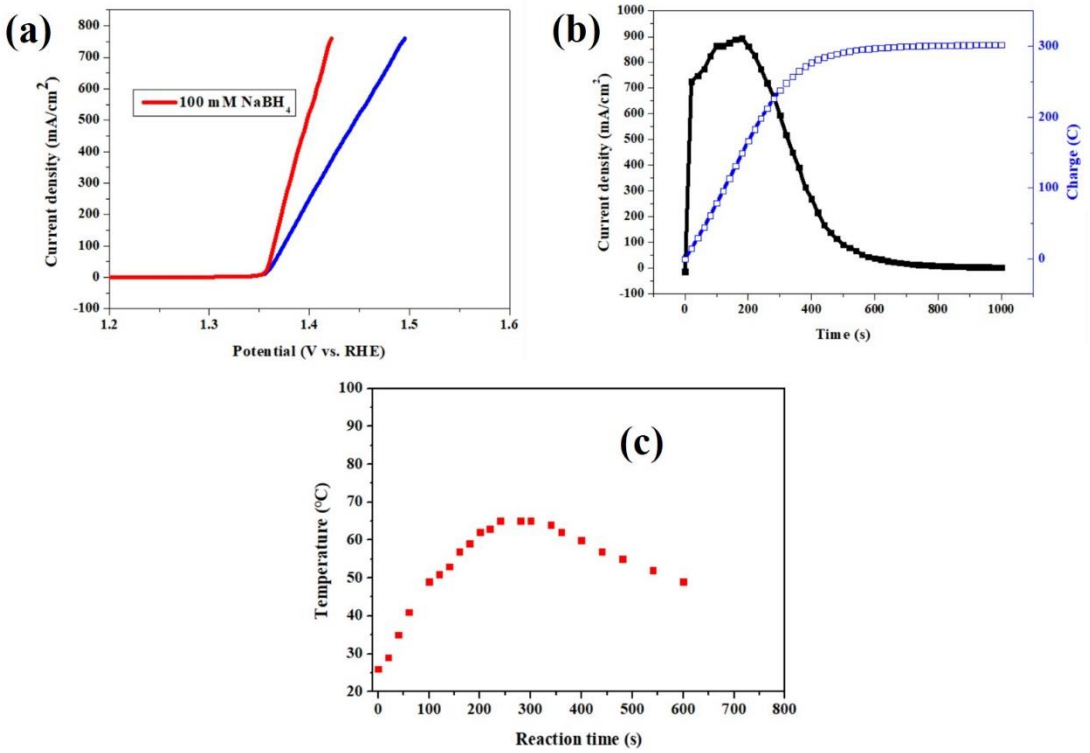

Figure S93. a) LSV curve of NiFe-1 catalyzed $NaBH_4$ electro-oxidation in a H-cell (blue line is without compensation, while red line is with 85% iR compensation), b) Current densities, charges *v.s.* time curves, c) Temperature changes *v.s.* time in the cathode chamber measured by an external thermometer. Reaction condition: 1 M KOH and 100 mM $NaBH_4$.

9. References

[1] W.-J. Liu, L. Dang, Z. Xu, H.-Q. Yu, S. Jin, G.W. Huber, *ACS Catal.* **2018**，*8*, 5533-5541.

[2] M. Zhang, Y. Liu, B. Liu, Z. Chen, H. Xu, K. Yan, *ACS Catal*. **2020**, *10*, 5179-5189.

[3] X. Deng, X. Kang, M. Li, K. Xiang, C. Wang, Z. Guo, J. Zhang, X.-Z. Fu, J.-L. Luo, *J. Mater. Chem. A* **2020**, *8*, 1138-1146.

[4] N. Jiang, B. You, R. Boonstra, I.M. Terrero Rodriguez, Y. Sun, *ACS Energy Lett.* **2016**, *1*, 386-390.

[5] B. You, X. Liu, N. Jiang, Y. Sun, *J. Am. Chem. Soc.* **2016**, 138, 13639-13646.

[6] B. You, N. Jiang, X. Liu, Y. Sun, *Angew. Chem. Int. Ed.* **2016**, 55, 9913-9917.

[7] X. Huang, J. Song, M. Hua, Z. Xie, S. Liu, T. Wu, G. Yang, B. Han, *Green Chem.* **2020**, 22, 843-849.

[8] L. Gao, Z. Liu, J. Ma, L. Zhong, Z. Song, J. Xu, S. Gan, D. Han, L. Niu, *Appl. Catal. B: Environ.* **2020**, 261, 118235.

[9] M. J. Kang, H. Park, J. Jegal, S. Y. Hwang, Y. S. Kang, H. G. Cha, *Appl. Catal. B: Environ.* **2019**, 242, 85-91.

[10] Z. Zhou, C. Chen, M. Gao, B. Xia, J. Zhang, *Green Chem.* **2019**, 21, 6699-6706.

[11] Y. Lu, C. L. Dong, Y. C. Huang, Y. Zou, Z. Liu, Y. Liu, Y. Li, N. He, J. Shi, S. Wang, *Angew. Chem. Int. Ed.* **2020**, 59, 19215-19221.

[12] S. Barwe, J. Weidner, S. Cychy, D.M. Morales, S. Dieckhöfer, D. Hiltrop, J. Masa, M. Muhler, W. Schuhmann, *Angew. Chem. Int. Ed.* **2018**, 57, 11460-11464.

[13] B. You, X. Liu, X. Liu, Y. Sun, *ACS Catal.* **2017**, 7, 4564-4570.

[14] Y. Song, Z. Li, K. Fan, Z. Ren, W. Xie, Y. Yang, M. Shao, M. Wei, *Appl. Catal. B: En.* **2021**, 299, 120669.

[15] G. Yang, Y. Jiao, H. Yan, Y. Xie, A. Wu, X. Dong, D. Guo, C. Tian, H. Fu, *Adv. Mater.* **2020**, 32, 2000455.

[16] Z. Zhou, C. Chen, M. Gao, B. Xia, J. Zhang, *Green Chem.* **2019**, 21, 6699-6706

[17] N. Zhang, Y. Zou, L. Tao, W. Chen, L. Zhou, Z. Liu, B. Zhou, G. Huang, H. Lin, S. Wang, *Angew. Chem. Int. Ed.* **2019**, 58, 15895-15903.

[18] X. Huang, J. Song, M. Hua, Z. Xie, S. Liu, T. Wu, G. Yang, B. Han, *Green Chem.*, **2020**, 22, 843-849.

[19] S. Li, X. Sun, Z. Yao, X. Zhong, Y. Cao, Y. Liang, Z. Wei, S. Deng, G. Zhuang, X. Li, J. Wang, *Adv. Funct. Mater.* **2019**, 29, 1904780.

[20] K. Gu, D. Wang, C. Xie, T. Wang, G. Huang, Y. Liu, Y. Zou, L. Tao, S. Wang, *Angew. Chem. Int. Ed.* **2020**, 60, 20253 –20258.

[21] B. Zhou, Y. Li, Y. Zou, W. Chen, W. Zhou, M. Song, Y. Wu, Y. Lu, J. Liu, Y. Wang, S. Wang, *Angew. Chem. Int. Ed.* **2021**, 60, 22908-22914.

[22] Y. Xie, Z. Zhou, N. Yang, G. Zhao, *Adv. Funct. Mater.* **2021**, 31, 2102886.

[23] W. H. Lie, C. Deng, Y. Yang, C. Tsounis, K. -H. Wu, M. V. C. Hioe, N. M. Bedford, D. -W. Wang, *Green Chem.*, **2021**, 23, 4333-4337.

[24] J. N. Hausmann, R. Beltrán-Suito, S. Mebs, V. Hlukhyy, T. F. Fasler, H. Dau, M. Driess, P. W. Menezes, *Adv. Mater.* **2021**, 33, 2008823.